Diploma Thesis

Semicrystalline thermoplastics for light-based 3D printing

carried out at the

Institute of Applied Synthetic Chemistry

at **Technische Universität Wien**

under supervision of

Univ.Prof. Dipl.-Ing. Dr.techn. Robert Liska

Dr.techn. Katharina Ehrmann

Alexander Ricke, MSc

by

Michael Göschl, B.Sc.

01425491

———————————————
Michael Göschl, B.Sc.

Danksagung

Als Erstes möchte ich Professor Robert Liska danken, der einerseits eine einzigartige Arbeitsatmosphäre in der Forschungsgruppe pflegt, und andererseits viel wertvollen wissenschaftlichen Input für diese Arbeit gegeben hat. Auch meinen Betreuern Kathi und Alex gilt mein Dank. Danke Kathi für die aufmerksame Literaturbetreuung und die detailreichen Korrekturen, aus denen ich viel gelernt habe. Und Alex, dir kann ich gar nicht genug danken für die Unterstützung bei Fragen und Problemen innerhalb des Labors und auch außerhalb. TOP!

Meinen besonderen Dank muss ich den Otex Bois Flo, Pontus und Fitzi aussprechen, die den Arbeitsalltag zu einer Freude gemacht haben! Flo für deine Motivation, andere zu motivieren und deine Herzlichkeit, Pontus, weil du mühelos einen ganzen Raum mit Lachen füllen kannst, und Fitzi für deine ewige Hilfsbereitschaft und deinen trockenen Humor.

Allen anderen MCs gilt ebenso mein Dank für einen reibungslosen und konstruktiven Laboralltag. Besonders hervorzuheben sind noch Lisa, Babsi und Dani, und die weiteren H21-Laborkollegen Stefan, Oxi, Jakob und Anna. Aber auch Viola, Davide, Sarah, Betti, David, Jan, Ralle, Stephan, Anna Maria, Philip, Flo, Larissa, Carola, Klausi, Toni, Roli, Nikol, Lorenzo und Tina haben mitgeholfen, die Stunden bei der Arbeit und auch viele gemeinsame Stunden außerhalb der Arbeitszeit mit Freude zu füllen! Eine besondere Erwähnung gilt auch Hansi, der mir mit einem interessanten Wahlpraktikum überhaupt erst den Zugang zu dieser Gruppe gezeigt hat, und mir auch während der Diplomarbeit noch mit wichtigen Tipps zur Seite gestanden ist.

Mein Dank gebührt ebenfalls den „Männern von Flake", die im Studium und außerhalb seit langer Zeit wichtige Begleiter für mich sind. Ebenso muss der „Fightzustand" erwähnt werden, eine bunt gemischte Gruppe von großartigen Menschen, mit denen ich in vielen Jahren viel Schönes erlebt habe!

Meiner Mutter Verena danke ich für ihre immerwährende Unterstützung jeglicher Art. Danke, dass du mir beigebracht hast, alles mit einer positiven Einstellung anzugehen!

Meiner Freundin Shilpa danke ich für guten Humor, Wärme, Unterstützung und Vertrauen. Ich freue mich darauf, die nächsten Jahre die Welt gemeinsam zu erkunden!

I

Table of contents

Abstract

Photopolymerization offers a simple and versatile method to produce polymeric materials. Stereolithography, a 3D-printing technique where a light source sequentially polymerizes a monomer formulation layer by layer in a vat, has recently been modified into a technology called Hot Lithography, where the vat and printing head are heated during printing to reduce monomer viscosity and to enable the printing of materials with high melting points. As of late, new challenges have emerged for photopolymers intended for the use in light-based 3D printing, especially concerning the fact that photopolymers are traditionally covalently crosslinked thermosets.[1] This leads to decreased recyclability and low fracture toughness due to high network density and network inhomogeneities. The goal of this work is to produce new non-crosslinked photopolymers that can be reprocessed by thermal methods, greatly improving recyclability. Efforts are made to improve the mechanical properties by introducing crystalline phases. To achieve this, the material is polymerized from a liquid crystalline molten phase, where the degree of order in the liquid phase translates into the solid phase, yielding a semicrystalline polymer.

A library of liquid crystalline difunctional monomers was synthesized for polymerization with other difunctional monomers. The monomers contain a mesogenic core group, which is responsible for the liquid crystalline properties of the material. The mesogenic groups can align in the liquid phase and exhibit a long-range order usually only observed in solid materials. Aliphatic spacer chains were attached to reduce the melting point of the monomer. The end groups consist of terminal alkenes or thiols for radical thiol-ene step growth polymerization.

A screening experiment was performed to test the most promising ene-monomer for its polymerization properties with a variety of available difunctional thiols. Further studies were performed with the monomer combination that showed the best results regarding their polymerization properties. To improve the fracture toughness of the material, the liquid crystalline monomer was substituted partially with other, more elastic difunctional

ene-monomers in varying concentrations. One of the chosen materials was obtained commercially, while the other one was synthesized. The monomer mixtures were investigated for their viscosity and their stability at the temperature where the polymerization was performed. Using real time monitoring, the polymerization process of the monomer mixtures was investigated. The resulting polymers were characterized to gain information about their molecular weight and their thermomechanical properties. Additionally, the phases and phase transition behavior of the polymers was investigated.

Kurzfassung

Photopolymerisation ist eine einfache und vielseitige Methode zur Herstellung von polymeren Werkstoffen. Stereolithographie, eine 3D-Drucktechnik, mithilfe derer eine Lichtquelle eine Monomerformulierung Schicht für Schicht in einer Wanne aushärtet, wurde vor kurzem in eine Technik namens Hot Lithography verfeinert. Hierbei werden die Wanne und der Druckkopf während des Druckprozesses erhitzt, um die Viskosität von Monomeren zu senken, und um hochschmelzende Monomere als Ausgangsmaterialien für den Druck zu erschließen. Die Anforderungen für Photopolymere im 3D-Druck erhöhen sich stetig, und die Nachfrage nach Alternativen zu traditionellen quervernetzten Duromeren ist in den letzten Jahren stark gewachsen. Klassische Duromere sind nicht recyclierbar und weisen zudem häufig eine niedrige Bruchzähigkeit durch hohe Netzwerkdichten und Unregelmäßigkeiten im Netzwerk auf. Das Ziel dieser Arbeit ist die Herstellung von neuen nicht quervernetzten Photopolymeren, die mithilfe von thermischen Verfahren wiederverarbeitet werden können, was die Recyclierbarkeit der Materialien stark erhöht. Mittels der Einbringung kristalliner Phasen in die Polymere soll eine Verbesserung der mechanischen Eigenschaften der Polymere erreicht werden. Dies soll mithilfe der Einbringung kristalliner Phasen in die Polymere erreicht werden. Dafür wird das Material aus einer flüssigkristallinen Schmelzphase polymerisiert, wobei die Ordnung, die in der Flüssigphase präsent ist, in die Festphase übertragen wird, wodurch ein semikristallines Polymer erzeugt wird.

Eine Sammlung flüssigkristalliner difunktioneller En-Monomere wurde für die Copolymerisation mit difunktionellen Thiolen synthetisiert. Diese Monomere enthalten eine mesogene zentrale Gruppe, welche für die Flüssigkristallinität verantwortlich ist. Die mesogenen Gruppen können in der Flüssigphase eine Fernordnung bilden, die üblicherweise nur bei festen Stoffen beobachtet wird. Aliphatische Spacer-Ketten wurden angefügt, um den Schmelzpunkt des Monomers zu senken. Die Endgruppe besteht aus

endständigen Alkenen bzw. Thiolen, die eine radikalische Thiol-En-Stufenwachstumspolymerisation eingehen können.

Ein Überblicksversuch wurde durchgeführt, um die Polymerisationsfähigkeit des vielversprechendsten En-Monomers in Kombination mit mehreren unterschiedlichen difunktionellen Thiolen zu testen. Mit der Monomerkombination durchgeführt, mit der die besten Ergebnisse erreicht wurden, wurden weitere Tests durchgeführt. Um die Bruchzähigkeit des erhaltenen Polymers zu verbessern, wurde das flüssigkristalline Monomer zum Teil durch andere, elastischere En-Monomere in unterschiedlichen Konzentrationen ersetzt. Eines dieser Monomere wurde kommerziell bezogen, ein weiteres wurde synthetisiert. Die Viskosität und thermische Stabilität der Monomermischungen an der Polymerisationstemperatur wurde untersucht. Mithilfe von Echtzeituntersuchungen wurde das Polymerisationsverhalten der Monomermischungen getestet. Die Molekulargewichte und die thermomechanischen Eigenschaften der erhaltenen Polymere wurden ermittelt. Zuletzt wurden die Phasen und Phasenübergänge der Polymere untersucht.

Introduction

1   Additive manufacturing technologies

Additive manufacturing technologies (AMT), commonly called 3D printing, is the generic term for all manufacturing technologies that automatically produce parts by physically making and joining volume elements. In practice, additive manufacturing processes use a 3D computer aided design (CAD) model, which is split into layers. The 3D model is either built using a CAD software or imported as a 3D scan (Figure 1).[2]

| CAD model | computer processed slicing | conversion of slices into physical layers & merging physical layers | physical rapid prototyping model |
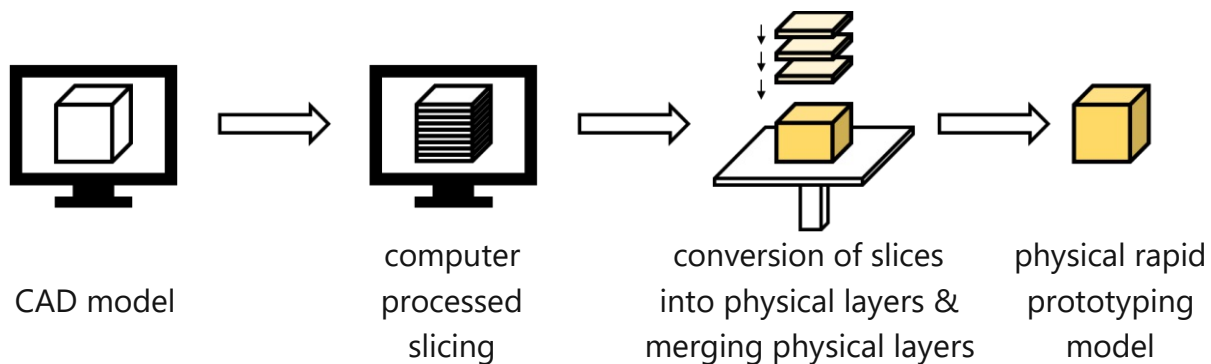
Figure 1: Typical AMT process.

AMT are divided into two main application levels: *rapid prototyping* serves to make models and mock-ups that can be tested quickly before the final part is manufactured. *Rapid manufacturing* produces finished parts or products.

Perhaps the biggest advantage of AMT is the capability of production independent of the number of pieces, as there is no need for an expensive mold or a new manufacturing method for each new part. This permits vastly increased customization of parts. Additionally, additive manufacturing allows for production of geometric details that cannot be made using subtractive or formative technologies, for example complex features on the inside of a part.

Various methods for generating layers for additive manufacturing have been developed:[2]

- Photopolymerization of liquid formulations to solid materials (Stereolithography, SLA)

- Shape-generation from the solid phase by sintering or melting processes from powders, powder mixtures, or granules (Powder Bed Fusion, e.g., Selective Laser Sintering, SLS)

- Layering process from cutting of foils and ribbons or milling of slabs (Layered Manufacturing, LM)

- Extrusion process from molten solid materials (Fused Deposition Modelling, FDM)

- "3D printing process" by conglutination of granules or powders by additional binders

- Precipitation from the gaseous phase by chemical or physical vapor deposition (CVD, PVD)

All AMT processes, which utilize the solidification of liquids are based on (photo-)polymerization and are summarized under the umbrella term stereolithography. Herein, a monomer formulation with no crosslinks is polymerized locally by exposure to (UV) light.

The oldest and still most accurate process is the laser scanning process (laser-SLA). With this method, a fine laser beam traces the desired cross section on the surface of a resin bath and locally generates the critical energy density necessary for polymerization. In microtechnology, the two-photon excitation process is applied for better accuracy.[3, 4]

When using stereolithography, it is important to limit the area of polymerization to achieve a good resolution. The polymerization must therefore only be able to be initiated by direct photon irradiation. The minimal depictable width in the x-y plane is a function of the laser diameter. The minimal height per layer in the z dimension is limited by the wettability of the solid layer by the liquid monomer. Insufficient layer thickness can cause

the layer to rip. However, in most practical cases, the layer thickness is a time and cost-related decision.[2]

Other processes include the lamp-mask process, in which the cross section of a layer is imaged onto a transparent mask and a UV lamp initiates the polymerization in the desired area through the transparent sections. In the nozzle-lamp process, a nozzle deposits the monomer layer, and a UV lamp is used to polymerize it. In the projections process, a powerful projector serves the function of both the mask and the light source.

In Digital Light Processing (DLP), a recent development in AMT, the light source and the imaging device are separated compared to the projections process, and instead of a physical mask, a digital micro mirror device chip is used (Figure 2).
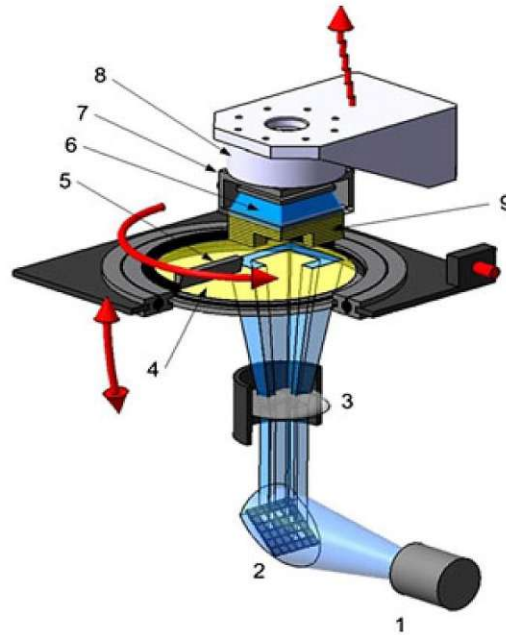
Figure 2: DLP setup: 1) Light source, 2) DMD-chip (dynamic mask), 3) optic, 4) vat with monomer mixture, 5) coating blade, 6) back light, 7) building platform, 8) load cell, 9) manufactured part.[5]

DLP has been described as a dynamic lamp-mask process. Using this technique, a full layer can be created with a single instance of light exposure through an LED light source. This enables faster processing speeds than the laser scanning process with optical accuracies of 25-60 µm. Another benefit of DLP lies in the facilitation of curing of oxygen sensitive

formulations, as the building platform is always located inside the liquid resin. The part is printed upside down with light exposure taking place through a transparent material vat.[5]

The digital light processing technique can be combined with a heated monomer vat and building platform in a process called Hot Lithography. This bears multiple benefits like higher conversions for many types of monomers, lower critical energies needed for curing, higher curing depths and higher printing speed due to lower viscosity of the resin. Additionally, it enables the use of monomers previously unavailable for printing, either due to high viscosities or high melting points of the monomers.[6]
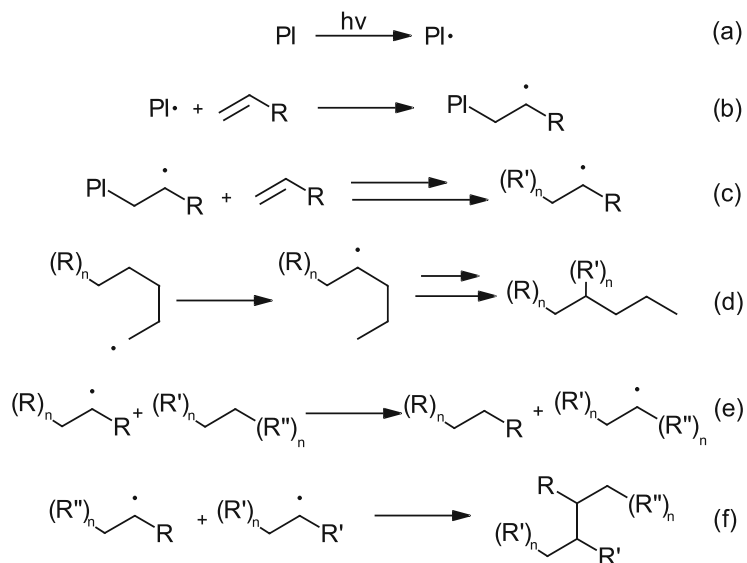
2 Free radical photopolymerization

Photopolymerization is a form of polymerization in which light is used to initiate polymerization. Advantages of photopolymerization include solventless bulk polymerization, fast reaction times, and the possibility for mild conditions around room temperature, which results in fewer side reactions.[7] Here, free radical photopolymerization will be discussed, which utilizes photoinitiators, which produce radicals upon irradiation.

Free radical photopolymerization happens in four main steps, which are excitation, initiation, propagation, and termination. In the excitation step, a photoinitiator (PI) is excited *via* irradiation with a (UV) light source, forming free radicals (Scheme 1 a). These radicals then attack the double bonds of polymerizable monomers in the initiation step (Scheme 1 b). In the propagation step, the radical site undergoes an addition reaction with another monomer (Scheme 1 c). Through repetition of this step, polymer chains are formed. During the polymerization, intra- and intermolecular chain transfer reactions that result in branching of the chains can take place. In intramolecular chain transfer, the radical site is moved to another location within the same polymer chain, causing short-chain branching (Scheme 1 d). In intermolecular chain transfer, the radical site is transferred from one polymer chain to another, causing long-chain branching (Scheme 1

e).[8] Chain transfer reactions can be advantageous because they lead to the formation of more homogenous networks with lower brittleness. Therefore, chain transfer agents like thiols or β-allyl sulfones are used to enhance the toughness of polymers.[9] Upon collision of two radical species, the chain reaction is terminated, which can take place through recombination of the radicals (Scheme 1 f) or disproportionation *via* hydrogen abstraction.[10]

Scheme 1: The steps of radical photopolymerization: a) excitation step, b) initiation step, c) propagation step, d) intramolecular chain transfer with short chain branching, e) intermolecular chain transfer leading to long chain branching, f) termination step.

In most cases, the polymerization happens rapidly, and the final molecular weight is reached quickly. However, in many monomer systems, the presence of oxygen can lead to inhibition *via* peroxyl radical formation, resulting in a much lower reactivity (Scheme 2). The biggest area of concern for oxygen inhibition is the preparation of films.
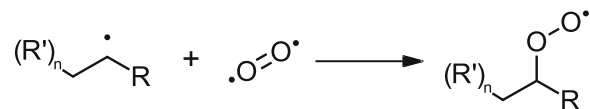
Scheme 2: Inhibition via formation of peroxyl radicals.

Possible solutions for this problem include the optimization of the photoinitiator, the use of inert atmospheres, higher light intensities, or the introduction of additives such as co-initiators or oxygen barriers.[11]

The photoinitiator (PI) is responsible for converting the energy provided by a light source into a reactive species that initiates the polymerization. Excitation takes place upon absorption of light from the ground state (S_0), which causes the photoinitiator to enter an excited singlet state (S_1 or S_2). Intersystem crossing can then take place to enter an excited triplet state (T_1) from which radical generation can occur among various other photochemical processes (Figure 3).[12]
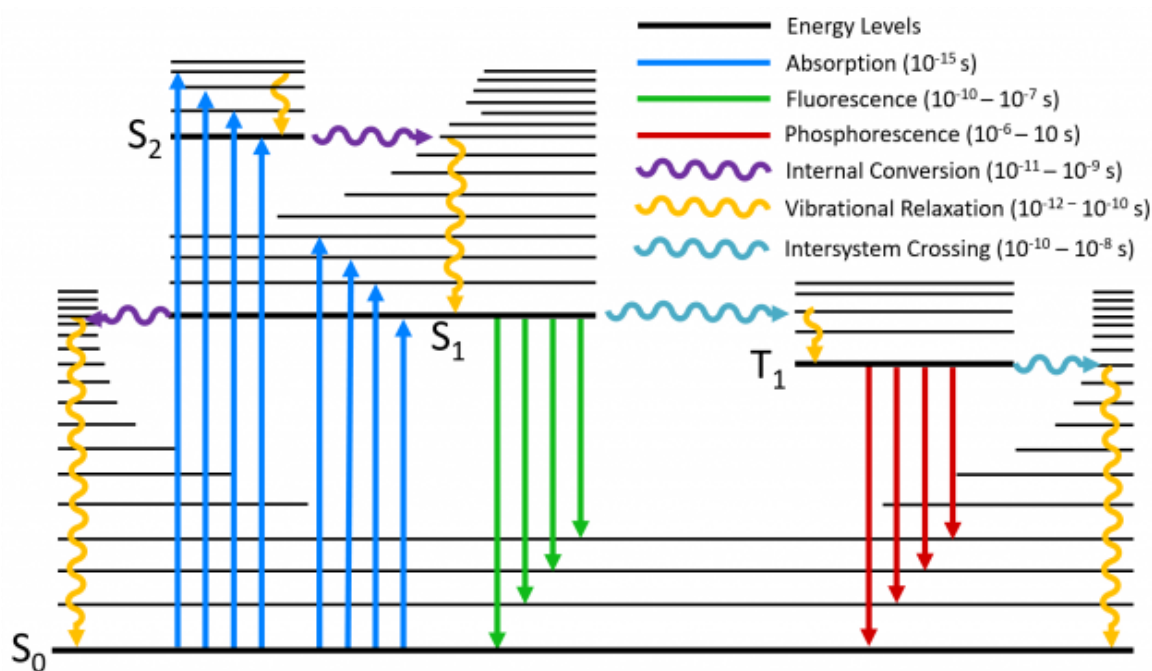
Figure 3: Jablonski diagram for different type of excitations and relaxations.[13]

Photoinitiators are divided into two main categories: Norrish type I and Norrish type II. Norrish type I photoinitiators (Figure 4) undergo a photolytic reaction that results in the homolytic cleavage of a C-C bond upon irradiation (Scheme 3). The cleavable bond is usually located in α position to a carbonyl group. A benzoyl group serves as the chromophore, which is responsible for the absorption of light. Germanium initiators like

Ivocerin (Figure 4 c) or camphorquinone (Figure 4 d) have an excitation wavelength in the visible light spectrum, which enables their use in medical applications and other applications where mild conditions may be necessary.[7, 14]
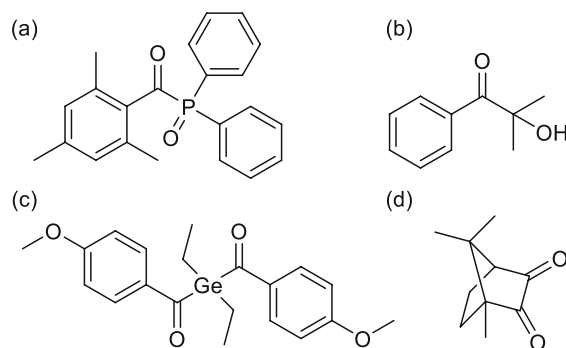
Figure 4: Commonly used type I photoinitiators for photopolymerization: a) diphenyl(2,4,6-trimethylbenzoyl)phosphine oxide (Lucirin TPO), b) 2-hydroxy-2-methyl-1-phenyl-propan-1-one (Irgacure 1173), c) Bis-(4-methoxybenzoyl)diethylgermanium (Ivocerin), d) camphorquinone. [10, 14]
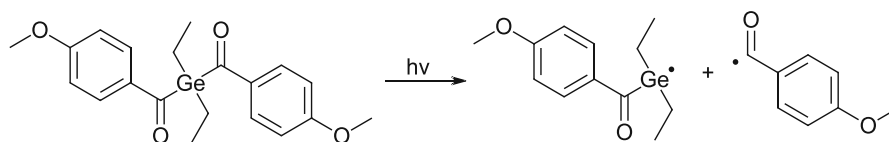
Scheme 3: Homolytic cleavage of Ivocerin upon irradiation.

Type II initiators (Figure 5 a, b) do not cleave by themselves when exposed to light. Instead, a co-initiator, usually a tertiary amine (Figure 5 c), acts as a hydrogen donor upon exposure to light (Scheme 4).
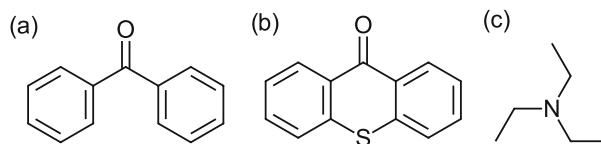
Figure 5: Commonly used type II initiators: a) benzophenone, b) thioxanthone, c) co-initiator triethylamine.
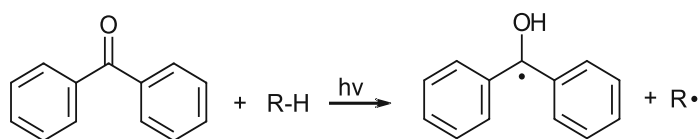
Scheme 4: Initiation mechanism of benzophenone as a type II photoinitiator.

Curing rates using type II photoinitiators are generally slower as the reaction follows a bimolecular mechanism. They are also more sensitive to quenching of excited triplet states.[7]

For some formulations, undesired polymerization initiation of the PI or the monomers may happen before irradiation. Therefore, especially when polymerizing materials at higher temperatures, a thermal stabilizer, or radical scavenger, may be necessary to prevent premature polymerization and to increase shelf life. Butylhydroxytoluene, 4-methoxyphenol (MEHQ), and hydroquinone have been used for stabilization of monomer systems.[15] Pyrogallol (PYR) has been proven to be an effective stabilizer for thiol-ene monomer mixtures.[16]
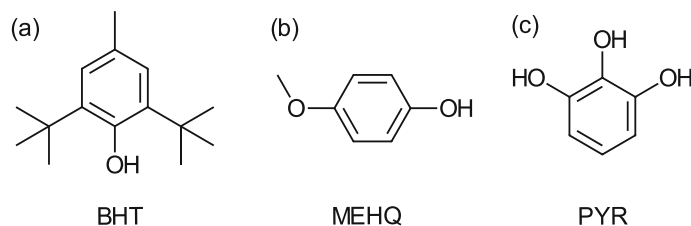
Figure 6: Thermal stabilizers for radical polymerization: a) butylhydroxytoluene, b) 4-methoxyphenol (MEHQ), c) pyrogallol (PYR).

3 Radical thiol-ene click reaction

The radical addition of thiols to alkenes is a powerful tool to create carbon-sulfur bonds under mild conditions with high yields in short reaction times. Additional benefits of this reaction mechanism are its orthogonality with many other reactions and 100% atom economy. The reaction is frequently started by the activation of a photoinitiator, which abstracts a hydrogen radical from a thiol, forming the thiyl radical (Scheme 5 a). This radical then undergoes an addition reaction with a carbon-carbon double bond to form a carbon-sulfur bond and a carbon-centered radical (Scheme 5 b). The carbon-centered radical can then abstract a hydrogen radical from another thiol, forming another thiyl radical (Scheme 5 c). Alternatively, the initiator may abstract a hydrogen radical from a carbon-carbon double bond, which then abstracts a hydrogen radical from a thiol.[17]

With this mechanism, terminal difunctional thiol monomers can be polymerized in bulk with difunctional ene-monomers in a step-growth mechanism to form linear polymers. To ensure high molecular weights, ene-monomers that exhibit low or no homopolymerization (Scheme 5 d) must be chosen.[18]
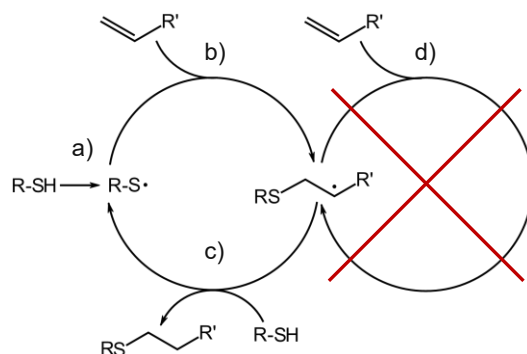
Scheme 5: Schematic of the radical thiol-ene step growth polymerization: a) initiation, b) propagation, c) chain transfer, d) homopolymerization of the ene-monomer.[18]

The reaction rates depend on the type of thiol and alkene monomers used. Mercaptopropionates are more reactive than mercaptoacetates, which, in turn, are more reactive than aliphatic thiols.
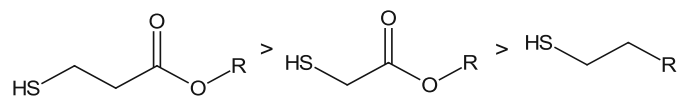
Figure 7: Thiol reactive groups in order of their rate of reactivity in the thiol-ene click reaction.

The influence of alkenes on the reaction rate is well documented, with norbornene groups showing the highest reactivities (Figure 8). Generally, ring strain and higher electron density of the double bond are beneficial to the reaction rate.[19]
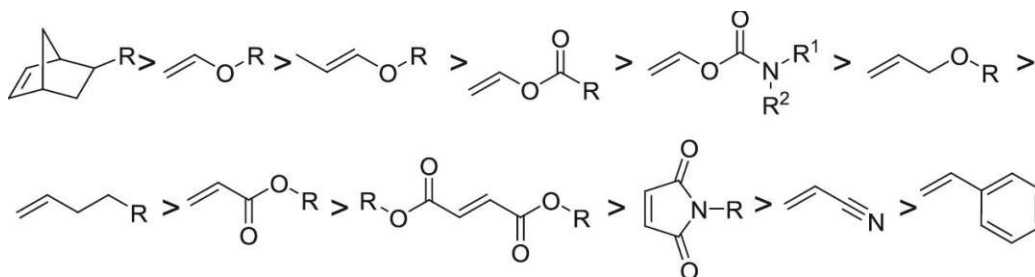
Figure 8: Various alkene groups in order of rate of reactivity in the thiol-ene click reaction.[19]

4   Semicrystalline polymers

Most polymers are either completely amorphous or partially crystalline. Amorphous polymers do not have a clearly defined melting point, they only have a glass transition temperature T_g, which separates glassy behavior from rubbery behavior and can change based on several parameters, e.g., the cooling rate and the presence of fillers in the polymer. Semicrystalline polymers also have a glass transition temperature along with a defined melting point.[20, 21]

The glass transition only occurs in amorphous regions and it is a kinetic transition unlike melting, which is a thermodynamic process. A fully crystalline polymer would have a defined melting point and no T_g. However, fully crystalline polymers are impossible to obtain using common processing conditions. The phase transitions in polymers may be measured using many different methods, for example dilatometry, differential scanning calorimetry (DSC), and dynamic mechanical analysis (DMA).[20, 21]

Semicrystalline polymers consist of alternating crystalline and amorphous phases, often forming a lamellar morphology (Figure 9 a). These lamellar structures can have random (isotropic) or ordered orientations (anisotropic). Anisotropic structures occur in films and fibers. The lamellar structures form sphere-shaped superstructures are called spherulites (Figure 9 b). The overall form of the spherulites is determined by the first forming (dominant) lamellae.[22] To analyze crystalline structures, small angle X-ray scattering (SAXS) and polarized optical microscopy may be be used.[23]

Microscopic analysis using polarized light is a widely used method for semicrystalline polymers. Spherulites are identified under a polarized optical microscope by their characteristic morphology in the form of a circular area with a maltese cross extinction pattern. The arms of this cross are aligned with the vibration directions of the polarizer and analyzer of the microscope.[24]
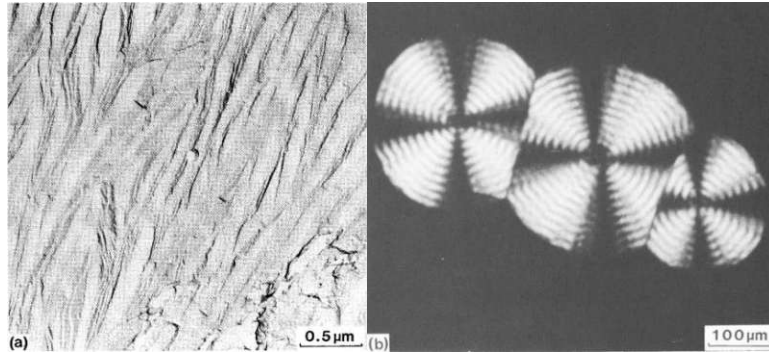
Figure 9: a) Lamellar and b) spherulitic morphology in semicrystalline polymers.[22]

The Avrami equation (1) describes isothermal crystallization kinetics for polymers. θ is the fraction of uncrystallized material remaining after a certain time. t is the time in which the material can crystallize, k is the growth rate parameter, and n is the nucleation parameter.

$$\theta = \exp(-kt^n) \tag{1}$$

The nucleation parameter describes the crystallite shape. A linear rod has a nucleation parameter of 1, a sphere growing in all directions simultaneously is described by a nucleation parameter of 4.[25]

The crystallization of polymers depends on many factors. Polyethylene, for example, has weak interchain bonding, but due to the linearity and flexibility of its chains, it is almost impossible to obtain as an amorphous material.[26] For crystallization to happen in a polymer, the molecules must be able to form an ordered configuration. Therefore, molecules in the melt must themselves be ordered, and capable of relative motion. The higher the degree of regularity, the more likely crystallization occurs in the molecule. The degree of regularity can be divided into three subcategories. Chemical regularity describes the chemical groups and the occurrence of branching on the polymer chain. Geometrical regularity describes the occurrence of head-to-head defects. Spatial regularity describes the orientation of side groups, which are connected to the polymer backbone *via* an asymmetric carbon atom. An example for the large influence of spatial regularity is polypropylene, where the tacticity is largely responsible for the degree of crystallinity.[22]

5   Liquid crystals

A liquid crystalline phase, also called mesomorphic phase or mesophase, is a state of matter between the long-range order typically found in crystalline solids and the long-range disorder found in liquids and gases. Liquid crystals are generally made of molecules that have anisotropic shapes, which are called mesogens, and are best known for their use in flat panel displays.[27] Other uses include optical devices like liquid crystal tunable filters[28] or use of liquid crystalline polymers as blends with thermoplastics for improved mechanical properties.[29, 30] To obtain a molecule capable of forming a mesomorphic phase, mesogenic groups are necessary. There are two classical types of mesogenic groups: discotic (disc-shaped) and calamitic (rigid linear) mesogens. In most cases, they consist of closely connected aromatic groups. Flexible spacers, usually alkyl chains, are attached to the mesogenic groups to prevent complete crystallization.[31]

Substances are considered thermotropic if they become liquid crystalline at a certain temperature, or lyotropic if they form liquid crystalline structures when they are dissolved in certain solvents. If both conditions induce the formation of a mesophase in a substance, it is described as amphotropic. The nematic phase (N) is the least ordered liquid crystalline phase (Figure 10 b). It leads to long-range orientational order and short-range positional order. Characteristic for the nematic phase is a parallel orientation of the molecules with an axis that corresponds to the long axis of the mesogen. Smectic phases (Sm, Figure 10 c and d), and columnar (Col, Figure 10 e) phases are more ordered than nematic phases and induce long-range positional order. There are various smectic phases, for example smectic A (Sm_A), which forms an untilted layer, and smectic C (Sm_C), which forms a tilted layer.[32]
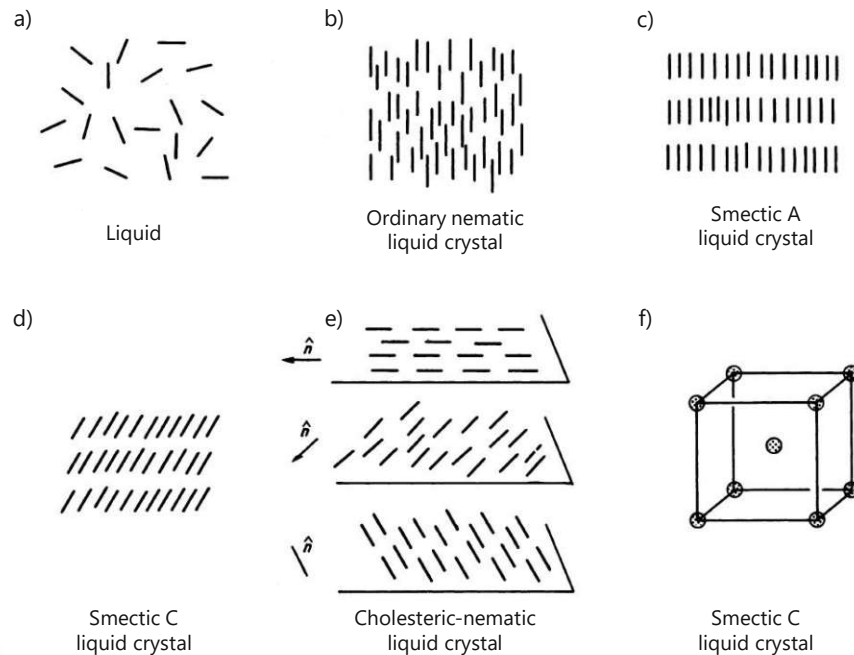
Figure 10: Phases with varying degrees of order, including a) liquid, b-e) liquid crystalline and f) crystalline phases.[32]

Another significant influence on liquid crystalline phase formation behavior of a mesogen is the length of the spacers. Research indicates that the balance of the spacer and the mesogenic group is an important factor on which mesophases are formed. There is no definitive trend in chain length that leads to highly ordered liquid crystalline phases, as demonstrated by Ujiie *et al.* With the tested liquid crystalline polymer, a smectic phase was formed with very short methylene spacer lengths of 2-4 units, followed by a less ordered nematic phase at 5-9 units. Polymers with spacer lengths of 10 and more led to the formation of more ordered smectic phases.[33]

Like semicrystalline materials, liquid crystals are also regularly analyzed by polarized optical microscopy (Figure 11). Light that passes through a liquid crystalline sample is subject to modifications in its polarization plane. The typical textures of different liquid crystalline phases can be seen under crossed polars. To observe phase transitions in thermotropic liquid crystals, a heated sample stage is utilized.[34]

Polarized optical microscopes make use of two polarizers, which allows for the analysis of minerals and other birefringent materials. The unpolarized light from the light source passes through a polarizer, which causes the light to vibrate within a single plane. In most standard settings, this filter is directed along the east-west direction, parallel to the horizontal line of the crosshair in the ocular. The polarizer may be able to be rotated by up to 90°. The analyzer, which is the second polarizing filter, is inserted above the sample stage in the north-south direction, parallel to the vertical line of the crosshair in the ocular. With both filters in perpendicular orientations, the sample is said to be viewed under crossed polars. This allows for light to pass through to the ocular only if the sample has birefringent or refractive characteristics.[35]
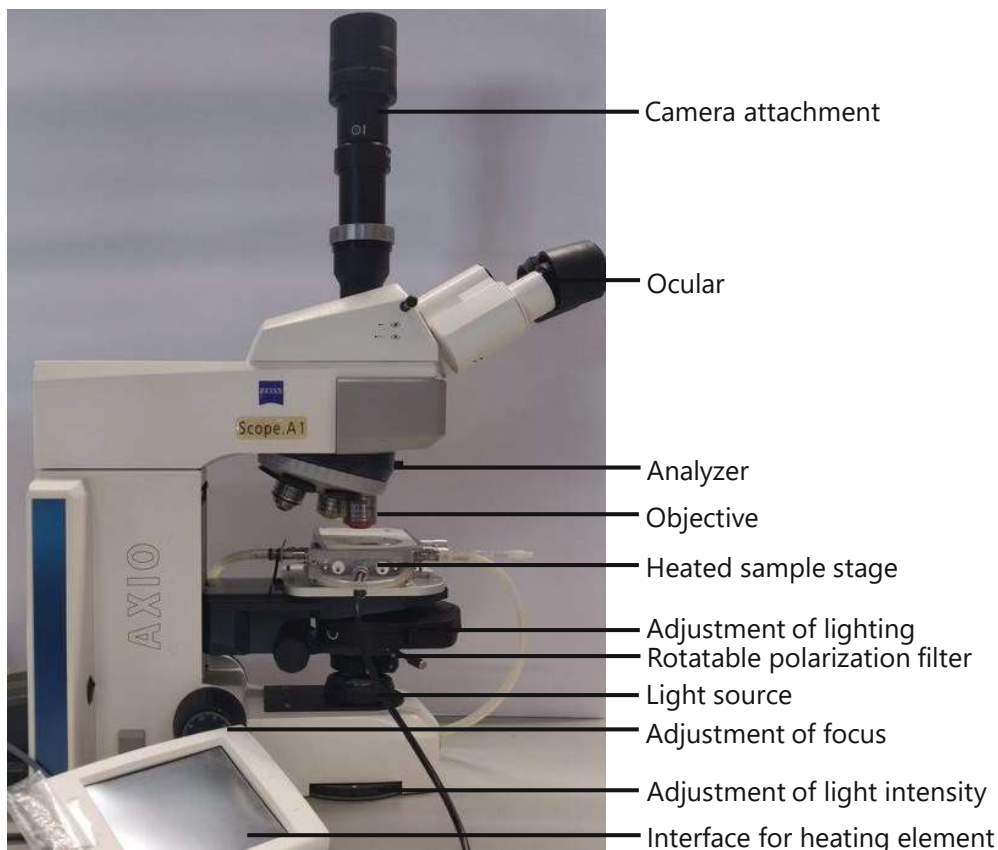
Figure 11: Components of heated stage polarized optical microscope Zeiss Axio Scope.A1

Objective

As of late, new challenges have emerged for photopolymers intended for use in 3D printing concerning the recyclability and reprocessability of the polymerized products. Photopolymers are traditionally covalently crosslinked thermosets[1] and therefore not recyclable. Moreover, they are often brittle due to high crosslinking density and inhomogeneities in the network. The aim of this work is to produce new non-crosslinked photopolymers that can be reprocessed by thermal methods, greatly improving recyclability.

Efforts are made to improve the mechanical properties of such materials consisting of linear polymer chains by increasing the glass transition temperature, which is normally below room temperature in thermoplastics, by introducing crystalline phases. To achieve this, a library of liquid crystalline monomers should be designed, synthesized, and used with the goal of polymerizing the material from a liquid crystalline molten phase. The degree of order in the liquid phase can then translate into the solid phase, yielding a semicrystalline polymer with improved mechanical properties.

The materials should make use of the radical thiol-ene click reaction for polymerization, since it is an efficient way to prepare linear polymers with a wide range of material properties. Therefore, liquid crystalline monomers with either two thiol or two terminal alkene moieties should be synthesized. The mesogenic groups and spacer chains should be chosen according to the requirements for hot lithography additive manufacturing.

Analysis of the polymers should be performed through a variety of methods. The polymerization kinetics should be evaluated *via* photo-DSC and real time photorheology measurements. The polymers should be analyzed for their molecular weight *via* gel permeation chromatography and their reactive group conversion *via* infrared and NMR spectroscopy. To be eligible for 3D printing, the monomer mixtures require a certain thermal stability and a low viscosity, which should be examined. The polymers should be analyzed for their phase transitions like glass transition temperature, melting point, and liquid crystalline phase changes. To achieve this, methods like differential scanning calorimetry, dynamic mechanical analysis or polarized optical microscopy can be used. Finally, mechanical tests of the polymers should be performed.

State of the art

Due to its versatility, thiol-ene chemistry is a broad research area that has witnessed the publication of many articles and reviews in scientific literature over the past 30 years. In this literature overview, the focus of attention will be set on recent developments in semicrystalline polymers that are prepared using thiol-ene chemistry, and the use of liquid crystalline monomers with a focus on thiol-ene chemistry. For readers who are interested in the broader subject of thiol-ene chemistry, reviews by Charles Hoyle and Christopher N. Bowman, and Andrew B. Lowe can serve as an excellent entry point to the subject.[18, 36]

1   Semicrystalline thiol-ene polymers

Bowman *et al*. used an equimolar formulation of 1,6-hexanedithiol and diallyl terephthalate (Figure 12) with diphenyl(2,4,6-trimethylbenzoyl)phosphine oxide (TPO) as a photoinitiator to form a tough, linear semicrystalline thermoplastic polymer usable for 3D printing. A storage modulus in tension of 100 MPa and elongations at break of up to 800% have been reported. Gel permeation chromatography results gave a number average molecular weight of about 6000 Da. Semicrystallinity was confirmed by polarized light microscopy. The material was successfully melted after 3D printing.[37]
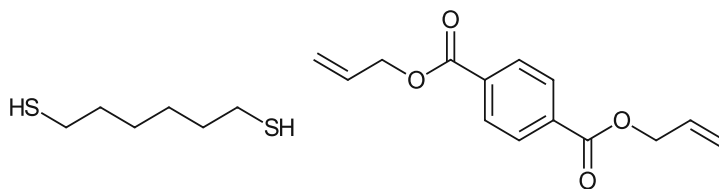
Figure 12: 1,6-hexanedithiol and diallyl terephthalate monomer combination, used by Bowman et al.[37]

A link between crystallinity of linear thiol-ene polymers and the aliphatic chain length of the thiol has been established, thus proving that minor structural changes in the monomers can cause significant changes in the resulting polymers. Crystallization was observed in all samples with an even number of alkyl groups in the aliphatic chain, while no crystallization was observed in any of the samples with an odd number of alkyl groups.[1]

Sycks *et al.* used 1,6-hexanedithiol in combination with 3,9-divinyl-2,4,8,10-tetraoxaspiro[5.5]undecan and a trifunctional thiol trimethylolpropane tris(3-mercaptopropionate) (TMPMP) as crosslinker in various concentrations (Figure 13). Without the crosslinker, a linear polymer was formed. Semicrystallinity was again confirmed by polarized light microscopy through the presence of spherulites. The crosslinker was used to enhance mechanical properties. With increasing crosslinking density, crystallinity decreased, and the glass transition temperature increased. At 0-20% crosslinking density, the T_g was around 0 °C. The T_g increased to 10 °C at 50% and 20 °C at 100% crosslinking density.[38] A crosslinking density of 7.5% was determined as ideal for mechanical properties, and the material was 3D printed with this composition.[39]
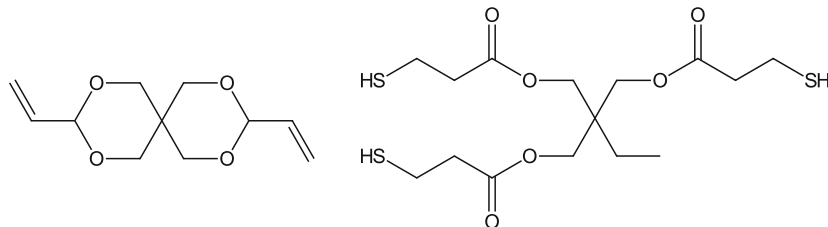
Figure 13: 3,9-divinyl-2,4,8,10-tetraoxaspiro[5.5]undecan and trimethylolpropane tris(3-mercaptopropionate), used by Sycks et al.[39]

2 Liquid crystalline monomers

Liquid crystalline acrylate and methacrylate monomers have been considered for composite dental fillings due to their low polymerization shrinkage, low viscosity, high monomer conversion and good mechanical properties.[40, 41] Photopolymerizable mesogens for use in LCD and OLED elements and other tailor-made optical applications are commercially available.[42]

Various routes for the synthesis of thermotropic liquid crystal monomers with reactive vinyl ether, epoxide and acrylate groups have been outlined in a review by Hikmet and Lub (Figure 14).[43]
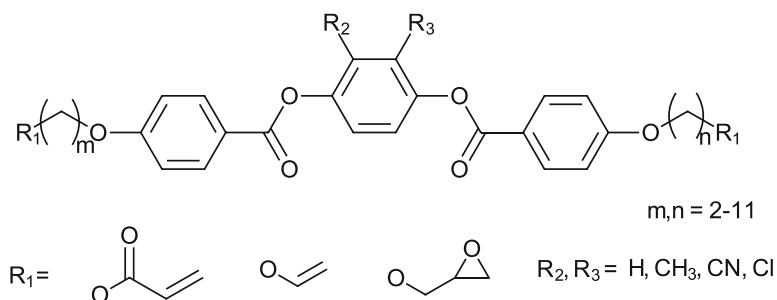
Figure 14: Monomers synthesized by Hikmet and Lub.

Strohriegl et al. have worked on liquid crystalline monomers, which polymerized into polymers that kept a liquid crystalline phase over a large temperature range. After cooling, some of the materials did not crystallize, but instead entered a glassy phase that kept the degree of order from the liquid crystalline phase.[44]

Various main-chain liquid crystalline elastomers have been prepared from acrylate-functionalized monomers, summarized in a review by Liu and Broer. Therein, the mesogenic group is part of the polymer backbone, as opposed to side chain liquid crystalline polymers in which the mesogenic group is attached to the polymer as a side chain. These materials demonstrated photomechanical responses upon exposure to UV light.[45]

Phenyl benzoate-based and biphenyl-based liquid crystalline thiol-ene monomers have been developed. Different types of mesophases were obtained by varying the length of the bridging unit and the spacer. Monomers containing one thiol group and one ene-group were synthesized and polymerized into novel main-chain liquid crystalline polymers. Highly defined mechanical, optical and electrical properties were expected from these polymers.[46]

Main-chain liquid crystalline thiol-ene polymers with focus on birefringent optical properties have been developed using benzoate-based liquid crystalline thiol-ene monomers with the thiol and ene-groups on a single molecule. 90 °C was reported as the ideal polymerization temperature. However, a large part of the alignment of the liquid crystal phase was lost during the polymerization process, rendering the material opaque.

Therefore, a crosslinkable thiol-ene monomer with two thiol and two ene-groups was developed, which resulted in optical transparency.[47] With continued focus on optical properties, polymer-dispersed liquid crystals inside a photopolymerized thiol-ene matrix have been prepared.[48]

Liquid crystalline thiol-ene elastomers have been prepared using a two-step process. In the first step, a thiol-Michael reaction addition of a bifunctional acrylate with a bifunctional thiol was performed. The resulting material was later partially photo-crosslinked by using a tetrafunctional thiol, creating a multidomain material.[49]

Focusing on mechanical properties, Lu *et al.* synthesized an interpenetrating liquid crystal elastomer network consisting of a polyurethane liquid crystal elastomer simultaneously polymerized with an acrylate thermoset. Their goal was to create a material for use in soft actuators like artificial muscles.[50] Photoinduced motion in liquid crystalline elastomer networks has been achieved through the preparation of an interpenetrating network incorporating azobenzene moieties.[51]

Yang *et al.* synthesized a variety of chiral liquid crystalline materials including mixed thiol and ene-functionalized molecule (Figure 15) that was photopolymerized into a liquid crystalline elastomer. Their goal was to synthesize liquid crystalline molecules for electro-mechanical applications. They prepared liquid crystalline elastomer microparticles that could reversibly contract by up to 400% at the nematic to isotropic phase transition.[52, 53]
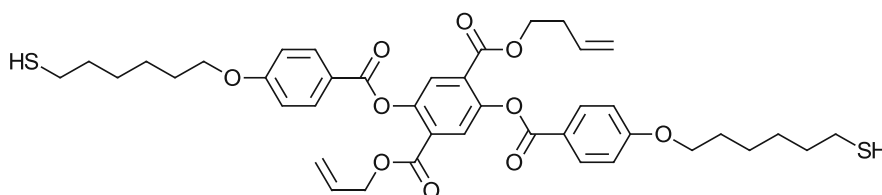
Figure 15: Thiol and allyl ether functionalized monomer synthesized by Yang et al. [52, 53]

The melting points of terminal alkene functionalized liquid crystalline molecules have been correlated with their spacer chain length (Figure 16).[54]
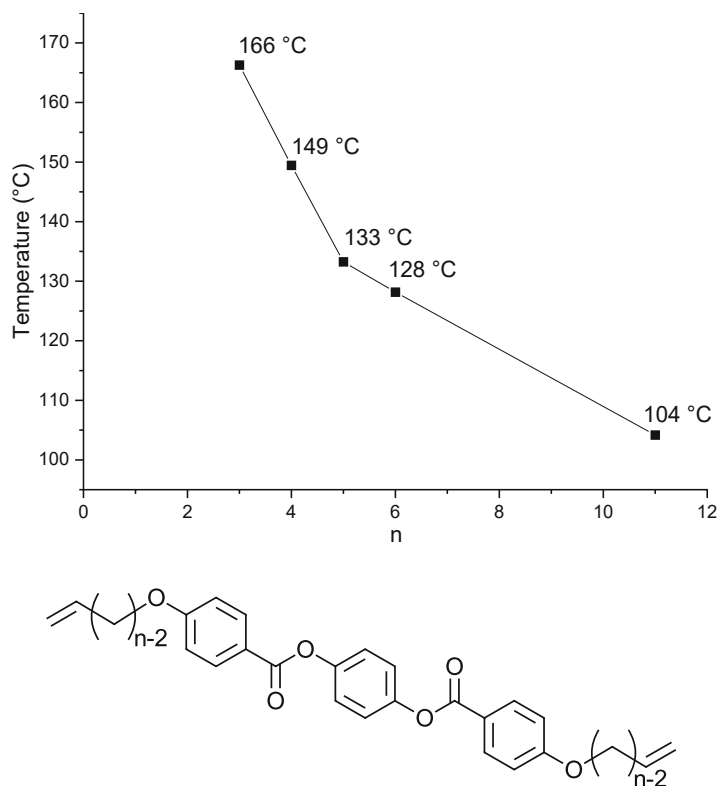
Figure 16: Melting points of liquid crystalline terminal alkenes with varying spacer lengths.[54]

Utilizing a thiol-Michael dispersion polymerization, Martinez *et al.* synthesized reversibly shape-programmable particles. The particle shapes were programmed *via* a photoinititated addition-fragmentation chain-transfer reaction, causing the particles to change shape between a spherical and a prolate shape when heated and cooled.[55] Additionally, they synthesized a reversibly mechanochromic liquid crystalline elastomer which demonstrated a blue shift in the visible spectrum when strained. The material returned to its original color when heated.[56]

Hoekstra *et al.* reported on the wavelength-selective photopolymerization of acrylate-oxetane cholesteric liquid crystal monomer mixtures (Figure 17). They were able to tune the reflective color of the resulting polymer network depending on the irradiation parameters during the polymerization.[57]
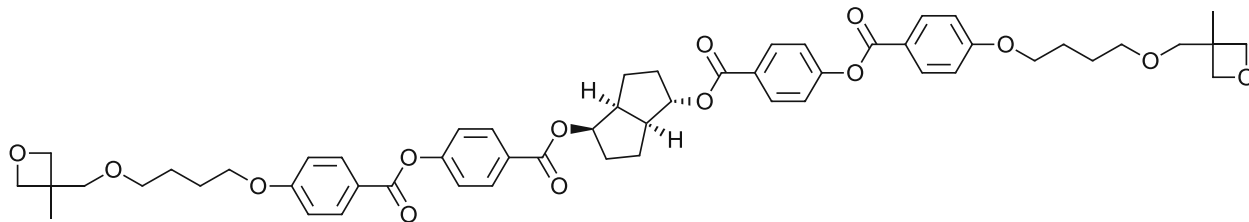
Figure 17: Liquid crystalline oxetane-functionalized monomer synthesized by Hoekstra et al.

3D printing of liquid crystalline actuators, often called 4D printing, has been realized with realized with various monomers. The fourth dimension describes the reversible change of shape through a certain stimulus like light or electrical impulses. The highly customizable nature of 3D printing in combination with motors that do not need to be connected to a power source could enable promising applications in soft robotics or medical uses.[58-60]

Results and discussion

1 Synthesis and characterization of monomers

A library of difunctional monomers was synthesized to contribute to the growing field of photopolymerizable thermoplastics. These monomers were prepared for characterization using different methods of analysis regarding their photopolymerization behavior, and the thermomechanical properties of the resulting polymers.

1.1 Liquid crystalline terminal alkene monomers

To create new semicrystalline polymers for 3D printing, several terminal dialkene monomers were considered for synthesis. The necessary functional groups for these molecules include a rigid mesogenic group for liquid crystalline properties, and non-homopolymerizable reactive end groups, like allyls or aliphatic terminal alkenes for polymerization with a difunctional thiol monomer. Aliphatic spacers may be necessary to reduce the melting point, which should not exceed 120 °C to remain in the operating range for Hot Lithography applications. With these requirements in mind, three liquid crystalline terminal alkene compounds were synthesized, each in a two-step reaction. The melting point was adjusted to fit the requirements by modification of the mesogenic core moiety and by variation of the aliphatic spacer length.

1.1.1 LCEM1

For the first monomer, a short spacer chain was chosen with the goal of achieving a high degree of crystallinity in the final polymer. A monomer melting point higher than the limitations of the Hot Lithography technique was therefore expected. In practice, the ene-monomer will be used in a formulation in conjunction with an equimolar amount of a dithiol monomer. The temperature at which this formulation is fully liquefied is likely to be lower than the melting point of the pure monomer. The liquid crystalline terminal

alkene compound p-[p-(allyloxy)benzoyloxy]phenyl p-(allyloxy)benzoate (LCEM1, Figure 18), was synthesized in a two-step process.

Figure 18: Liquid crystalline terminal alkene LCEM1.

For the first synthesis step, *p*-hydroxybenzoic acid was reacted with allyl bromide to form *p*-allyloxybenzoic acid (Scheme 6) in accordance with a procedure outlined by Shen *et al.*[61]. The product was obtained as a white powder with a yield of 65%.
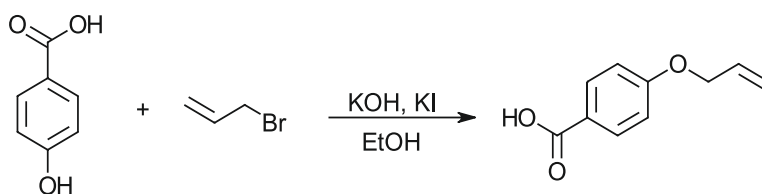
Scheme 6: Synthesis of p-allyloxybenzoic acid from p-hydroxybenzoic acid and allyl bromide.

In the second step, *p*-allyloxybenzoic acid was used in a Steglich esterification along with hydroquinone to synthesize the liquid crystalline monomer (Scheme 7) according to a procedure outlined by Zhang *et al.*[62]
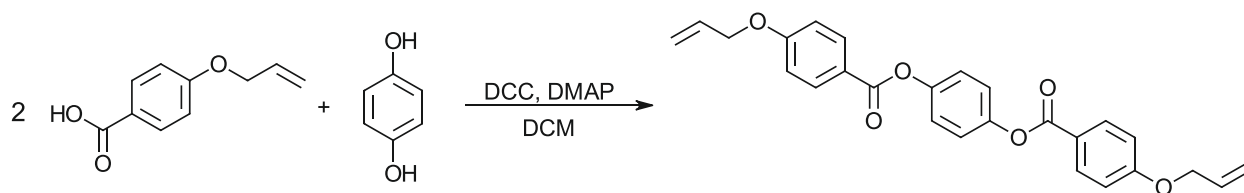
Scheme 7: Synthesis of LCEM1 from p-allyloxybenzoic acid and hydroquinone. Dicyclohexylcarbodiimide (DCC) was used as a coupling agent and 4-dimethylaminopyridine (DMAP) was employed as a catalyst. The reaction was performed in dichloromethane (DCM).

The solvent was removed, and purity was determined *via* NMR-spectroscopy, where several unexpected signals were found in the region of δ = 2-1 ppm. When melting the

25

polymer on a heated stage microscope, traces of a crystalline material were found, which were linked to the unexpected signals that appeared in the NMR-spectrum. They were identified as dicyclohexylurea (Figure 19), which is a byproduct of Steglich esterifications that employ DCC as a coupling agent.
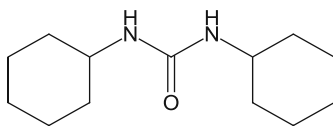
Figure 19: Dicyclohexylurea, byproduct of the LCEM1 synthesis.

Further purification was performed by dissolving the product in DCM and filtrating the solution, then crystallizing the product. The pure product was obtained as a white powder with a yield of 67%. The melting point of the material was determined at 166 °C, upon which a liquid crystalline phase formed, which appeared as a smectic phase. At 190 °C, a transition from a smectic to a nematic phase was observed, which persisted up to a temperature of 230 °C, at which point an isotropic molten phase formed.

1.1.2   LCEM2

Another liquid crystalline dialkene monomer synthesis was laid out with the goal of keeping a high degree of crystallinity while still reaching a workable melting point. Therefore, the molecule was designed to have short spacer chains, while a modification of the central mesogenic group was performed with the goal of reducing the melting point of the monomer. Thus, the synthesis of 4-[*p*-(allyloxy)benzoyloxy]tolyl *p*-(allyloxy)benzoate (LCEM2, Figure 20) was planned analogous to LCEM1.
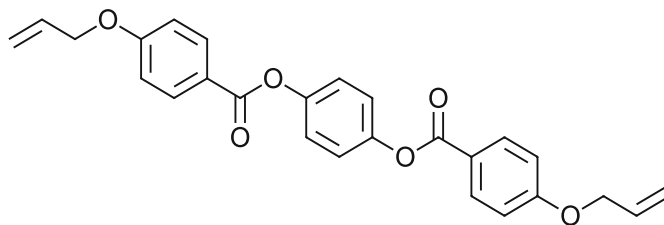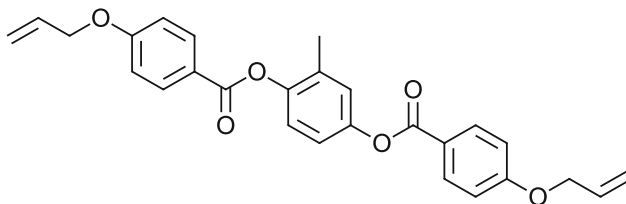

Figure 20: Liquid crystalline ene-monomer LCEM2.

For the first synthesis step, *p*-hydroxybenzoic acid was reacted with allyl bromide to form *p*-allyloxybenzoic acid (Scheme 8) in accordance with a procedure outlined by Shen *et al.*[61] The product was obtained as a white powder with a yield of 65%.
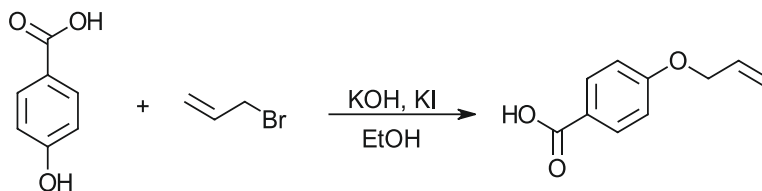
Scheme 8: Synthesis of p-allyloxybenzoic acid from p-hydroxybenzoic acid and allyl bromide.

The second liquid crystalline ene-monomer (LCEM2) was synthesized in another Steglich esterification using methylhydroquinone and *p*-hydroxybenzoic acid according to a procedure outlined by Zhang *et al.*[62] (Scheme 9). 1-ethyl-3-(3-dimethylaminopropyl) carbodiimide hydrochloride (EDC) was used as a coupling agent instead of DCC due to a more facile separation of the byproduct.
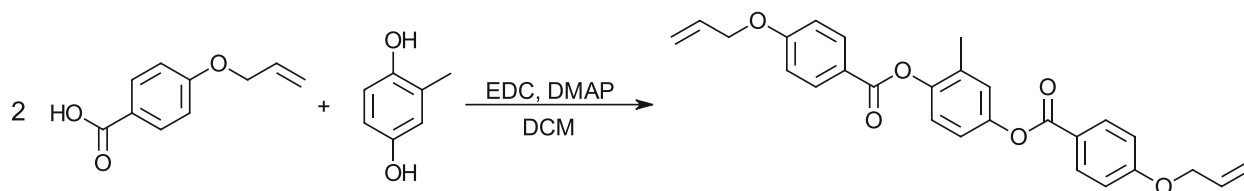
Scheme 9: Second step of the synthesis of liquid crystalline ene-monomer LCEM2. 1-ethyl-3-(3-dimethylaminopropyl)carbodiimide hydrochloride (EDC) was used as a coupling agent, and dimethylaminopyridine (DMAP) was used as a catalyst. Dichloromethane (DCM) was employed as solvent.

The product was obtained as a white powder after purification by two recrystallization steps with a final yield of 48%. The melting point of the material was determined at 142 °C, where a liquid crystalline phase formed. This phase persisted until the temperature of 217 °C, where a transition into an isotropic molten phase took place.

1.1.3   LCEM3

A plan for synthesis of a liquid crystalline ene-monomer with a melting point below 120 °C was laid out. According to a study by Koßmehl *et al.*, the melting point of a liquid

crystalline monomer using 11-bromo-1-undecene as a spacer is slightly above 100 °C, which would be suitable for the use in Hot Lithography (Figure 16).[54] Therefore, a plan was made to synthesize the monomer *p*-[*p*-(10-undecenyloxy)benzoyloxy]phenyl *p*-(10-undecenyloxy)benzoate (LCEM3, Figure 21).
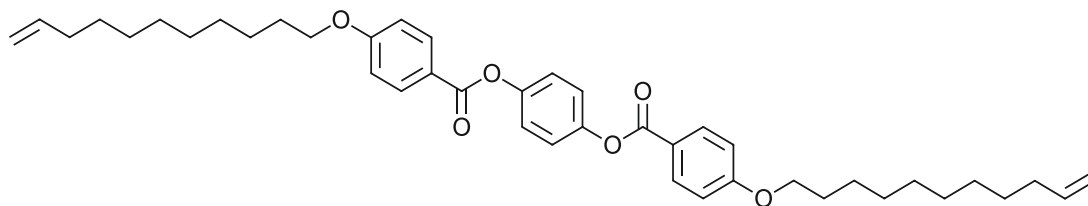
Figure 21: Liquid crystalline ene-monomer LCEM3.

In the first step of the synthesis of LCEM3, 11-bromo-1-undecene was reacted with *p*-hydroxybenzoic acid to form *p*-(undecenyloxy)benzoic acid (Scheme 10) in accordance with a procedure outlined by Shen *et al.*[61] The formation of a significant amount of esterified byproduct (Figure 22) was observed in addition to the product.
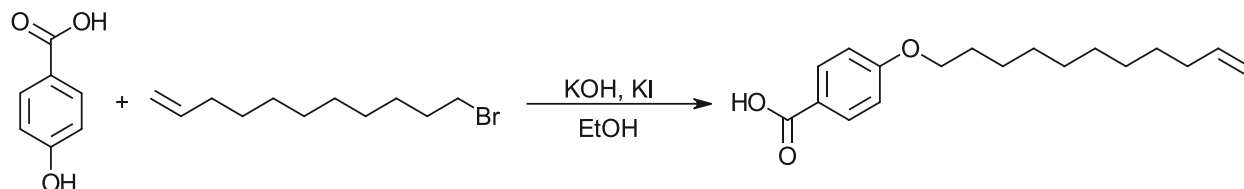
Scheme 10: Synthesis of p-(10-undecenyl-1-oxy)benzoic acid, the precursor of LCEM3.
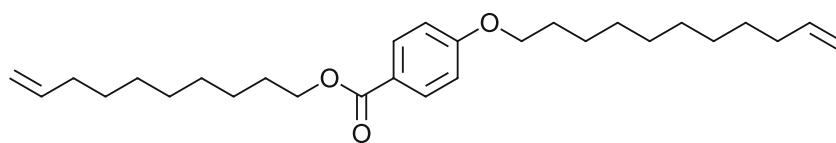
Figure 22: The esterified byproduct that formed during the synthesis of the precursor of LCEM3.

After removal of the esterified byproduct by washing with Et_2O, the product was obtained as a white powder with a yield of 68%.

To obtain LCEM3, the obtained intermediate was reacted with hydroquinone in a Steglich esterification according to a procedure outlined by Zhang *et al.* to obtain LCEM3 (Scheme 11).[62]
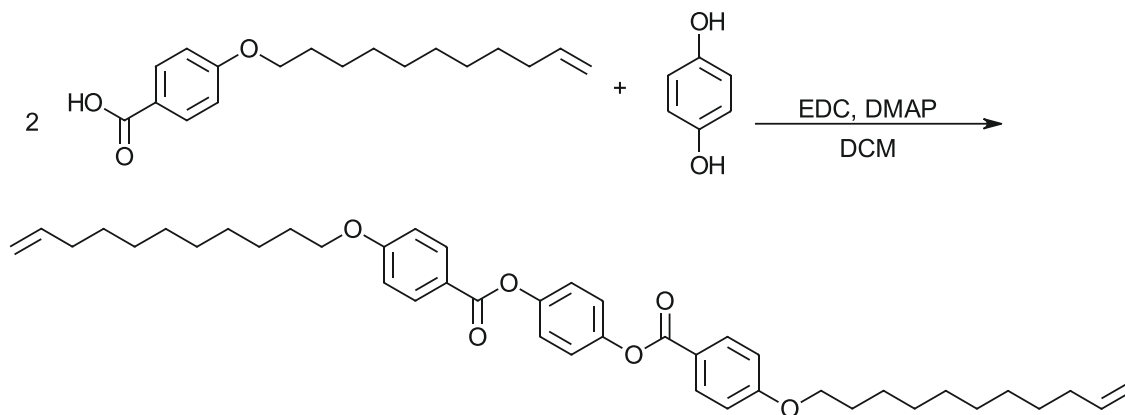
Scheme 11: Synthesis of the liquid crystalline difunctional ene-monomer LCEM3. 1-ethyl-3-(3-dimethylaminopropyl)carbodiimide hydrochloride (EDC) was used as a coupling agent, and dimethylaminopyridine (DMAP) was used as a catalyst. Dichloromethane (DCM) was employed as solvent.

Column chromatography was performed to purify the product. Purity was determined by reverse phase HPLC analysis, where some impurities of the esterified byproduct of the previous synthesis (Figure 22) were found. A high purity is crucial for a step-growth polymerization, as a deficit of one of the monomers causes a premature termination of the polymerization. Therefore, a recrystallization step was performed to purify the product successfully (Figure 23).
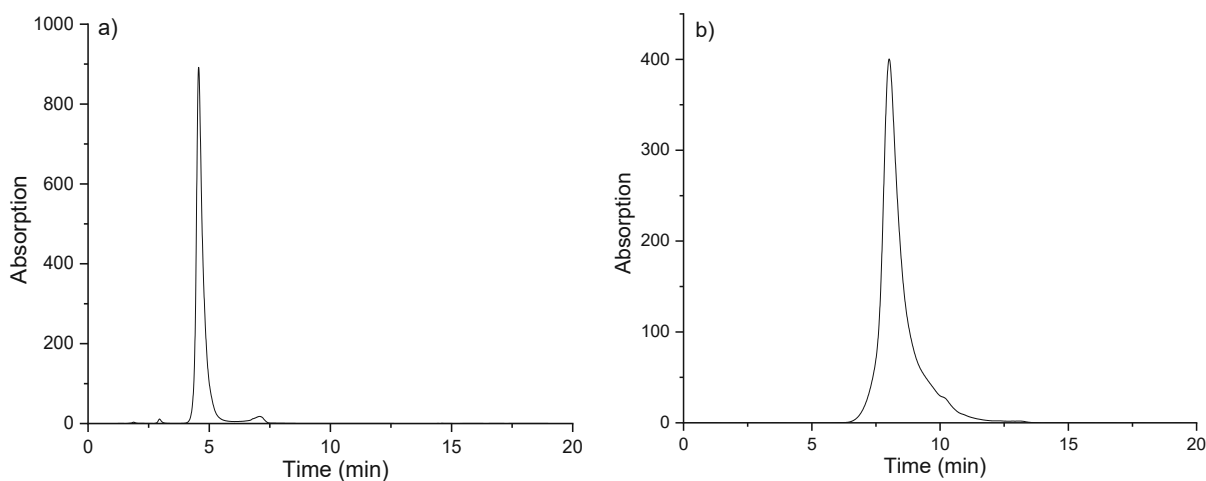
Figure 23: Reverse phase HPLC results for LCEM3: a) before and b) after the final recrystallization step.

No impurities were detected after recrystallization, after which the product was obtained as a white powder with a yield of 70%. The melting point of the material was determined at 111 °C, where it melted into a liquid crystalline phase. This phase had the appearance of a typical smectic C phase. At 140 °C, a nematic phase with colorful strand patterns formed, which persisted until 177 °C, where an isotropic molten phase was observed.

1.2   Liquid crystalline dithiol monomer

A synthesis plan for a liquid crystalline dithiol monomer with a mesogenic group used in the previously synthesized liquid crystalline monomers LCEM1-3 was laid out. A liquid crystalline dithiol monomer would offer much more flexibility regarding monomer choice compared to just having liquid crystalline ene-monomers available, as any difunctional alkene could be used as a co-monomer. This enables the possibility to tune the degree of crystallinity in the monomer accurately.

A commonly used method for thiol functionalization of molecules is the reaction of thiourea with alkyl halides and subsequent hydrolysis.[63] Due to the ester bonds in the mesogenic group used in the LCEM monomers, this was not an option, as the acidic or basic hydrolysis conditions would split the ester. Therefore, a synthesis taking advantage of the radical thiol-ene click reaction was prepared to synthesize a liquid crystalline difunctional thiol monomer *p*-[*p*-[3-(6-mercaptohexylthio)propoxy]benzoyloxy]phenyl *p*-[3-(6-mercaptohexylthio)propoxy]-benzoate (LCDT, Figure 24).
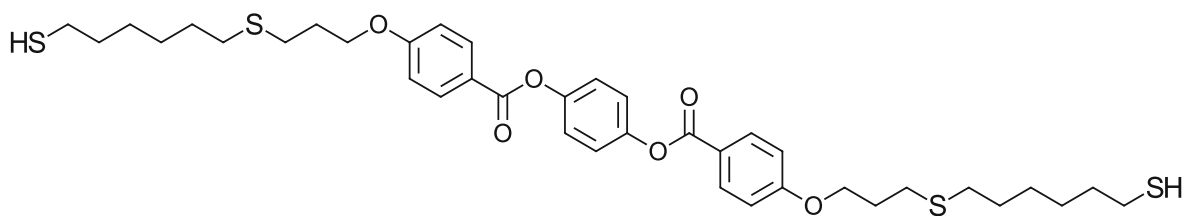
Figure 24: The liquid crystalline difunctional thiol monomer LCDT.

The synthesis was performed using LCEM1 (Chapter 1.1.1, Figure 18) as a starting material with an eight-equivalent excess of 1,6-hexanedithiol and azobisisobutyronitrile (AIBN) as a thermal radical initiator (Scheme 12).
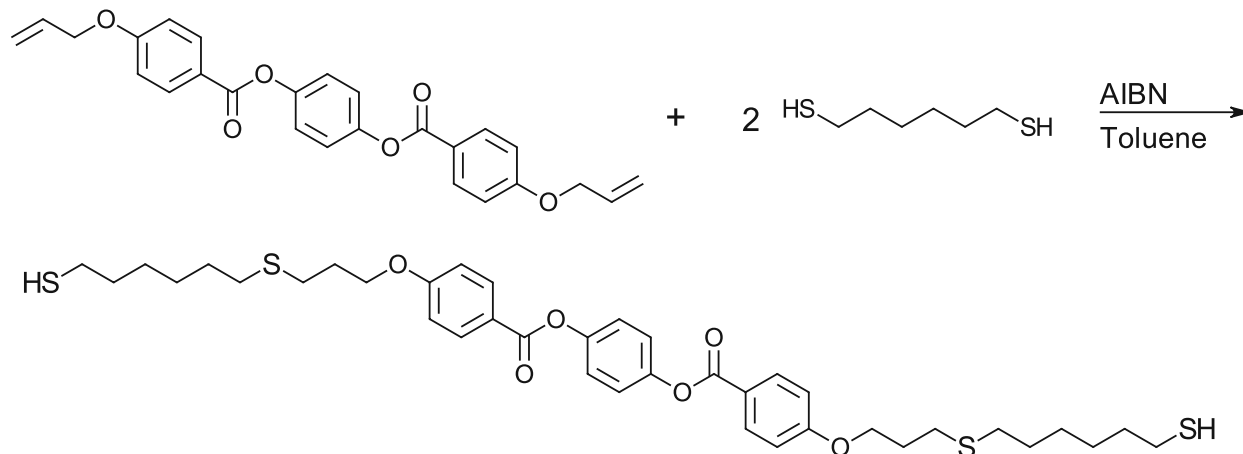
Scheme 12: Synthesis of liquid crystalline difunctional thiol monomer LCDT.

The product was obtained as a white powder after purification by column chromatography with a yield of 60%. The melting point of the material was measured to be 80 °C, where a liquid crystalline phase was observed that persisted until 133 °C. At this temperature an isotropic molten phase was formed.

1.3   Allyl-functionalized pTHF

To tune the mechanical properties of resulting polymers, a plan was laid out to partially substitute the liquid crystalline ene-monomers responsible for a high crystallinity and replace them with a more flexible monomer. Practically, this would lead to a larger portion of aliphatic spacers in the formulation. Thus, poly(tetrahydrofurane) (pTHF) was functionalized with allyl groups for use in thiol-ene polymerization (Figure 25).
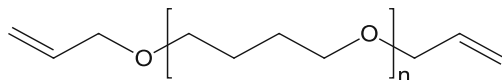
Figure 25: Allyl-functionalized pTHF (APF).

A Williamson ether synthesis using sodium hydride and allyl bromide was performed to convert the hydroxyl groups into allyl ether groups according to a procedure outlined by Jang et al.[64] (Scheme 13).
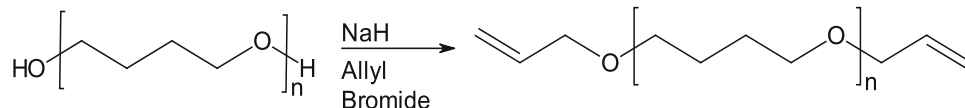
Scheme 13: Synthesis of allyl-functionalized pTHF (APF).

After purification by column chromatography, the product was obtained with a yield of 96% as a slightly yellow oil that solidified into a waxy substance after around three days at room temperature.

The reactant and the product were both analyzed using quantitative ^{31}P-NMR-spectroscopy, which served two purposes. Firstly, the hydroxyl number of pTHF and therefore its molecular weight was measured, which has been proven an accurate alternative to titration of the hydroxyl number.[65] The second purpose was to determine the conversion of the hydroxyl groups. This was performed by measuring the hydroxyl number of the product and calculating the OH number ratio between the product and the reactant.

By measurement of the integral of the hydroxyl groups compared to the internal standard in the NMR spectrum, a hydroxyl number of pTHF of 1.135 mmol g^{-1} was determined. This corresponds to a molecular weight of 1762 g mol^{-1}. For the allyl-functionalized pTHF a hydroxyl number of 0.026 mmol g^{-1} was calculated. The conversion of hydroxyl groups into allyl groups was therefore 97.4%.

2 Thiol monomer screening

LCEM3 (Chapter 1.1.3, Figure 26) was selected for polymerization experiments with a variety of dithiols due to its melting point at 111 °C, which is in the workable range for Hot Lithography applications.
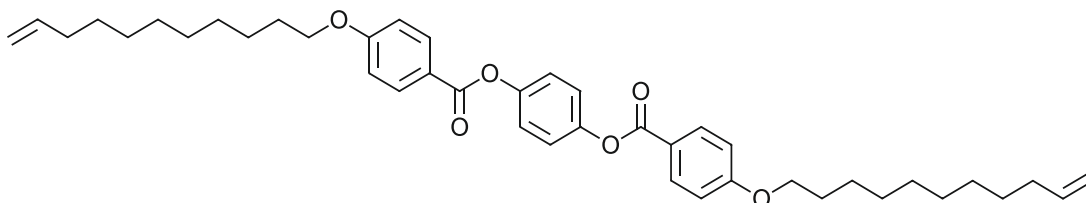
Figure 26: Difunctional terminal alkene monomer LCEM3.

LCEM2 (Chapter 1.1.2), which has a melting point of 142 °C, did not have a sufficiently low melting point for Hot Lithography experiments. An experiment, in which LCEM2 was combined in equimolar formulations with two different dithiol monomers (Figure 27 a,b) also did not result in a significant reduction of the melting point of the monomer. Therefore, it was not analyzed further in polymerization experiments.

To assess the polymerization properties of the liquid crystalline difunctional ene-monomer LCEM3, a variety of commercially available difunctional thiol monomers (Figure 27 a-f) were selected for a screening of their polymerization properties in combination with LCEM3. Additionally, the liquid crystalline dithiol LCDT (Figure 27 g) was selected.
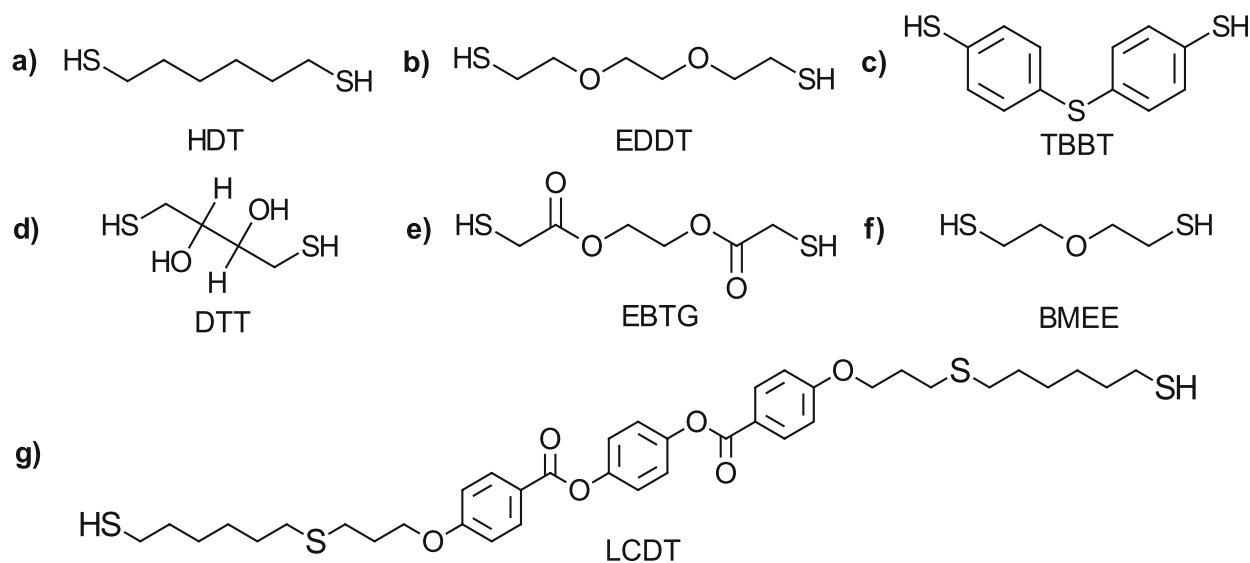
Figure 27: Difunctional thiols used for polymerization in combination with the difunctional ene-monomer LCEM3: a) 1,6-hexanedithiol (HDT); b) 2,2'-ethylenedioxy(diethanethiol) (EDDT); c) 4,4'-thiobisbenzenethiol (TBBT); d) dithiothreitol (DTT); e) ethylene bis(thioglycolate) (EBTG); f) bis(2-mercaptyethyl)ether (BMEE); g) liquid crystalline dithiol (LCDT).

The thiols depicted in Figure 27 were each mixed with an equimolar amount of LCEM3 monomer, 1 wt% Ivocerin as a photoinitiator, and 0.1 wt% pyrogallol as a thermal stabilizer. As a reference substance, a formulation of 1,6-hexanedithiol with an equimolar amount of the commercially available *p*-diallyl terephthalate (DAT, Figure 28) was used. This formulation had yielded a semicrystalline polymer with high tensile strength and elongation at break in experiments conducted by Bowman et al.[37]
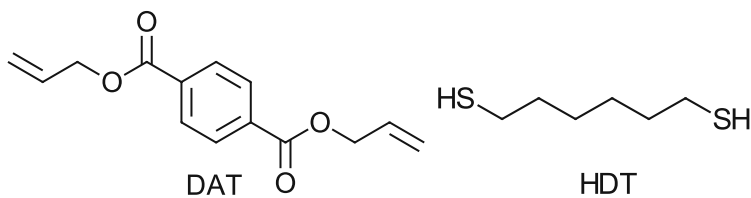
Figure 28: Diallyl terephthalate (DAT, left), which, in conjunction with 1,6-hexanedithiol (HDT, right), was used as a reference system.

The monomer mixture consisting of LCEM3 and LCDT exhibited problems regarding its thermal stability. After melting the formulation at ~120 °C, the mixture solidified again in less than one minute without cooling. An increase of the melting point to ~150 °C was confirmed afterwards *via* a melting point measurement. This confirmed the suspicion of initiation of spontaneous thermal oligomerization or polymerization, which prevented further characterization of the formulation and the resulting polymer.

Analysis of reactivity of the remaining formulations (LCEM3 in combination with Figure 27 a-f) was conducted *via* photo-DSC, and conversion was evaluated *via* NMR-spectroscopy.

2.1 Reactivity *via* photo-DSC

Photo-differential scanning calorimetry (photo-DSC) is a specialization of the DSC measurement method, where instead of a temperature change irradiation of a monomer mixture with light is measured compared to a reference sample. The measurement chamber is kept at a constant temperature and the energy required to hold the temperature during irradiation is measured. Typically, two irradiation periods are performed. After the second irradiation period, exothermic or endothermic signals from the second irradiation period are subtracted from signals measured during the first irradiation period. Therefore, it is important to choose an irradiation time that is long enough to guarantee that the photochemical reaction is finished.
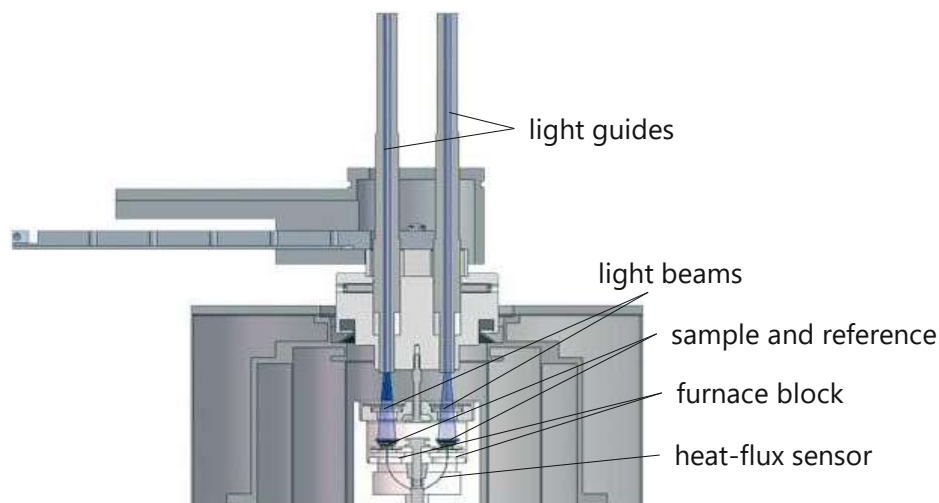
Figure 29: Schematic of a typical photo-DSC instrument with light guides, measurement cell containing sample and reference crucibles, heat-flux sensors for differential calorimetry, and furnace block for temperature control.

Thus, exothermal, and endothermal processes can be measured as heat flow as a function of time. The peak area of the curve resulting from plotting the DSC signal against irradiation time gives information about the exothermicity or endothermicity of chemical reactions in the sample during irradiation. The peak area is standardized to the sample mass and therefore, it is proportional to the number of reactive groups in the sample undergoing a chemical reaction. Thus, different samples can be compared even if there is a large discrepancy in the molar mass of the monomers, as long as the reactive groups are identical. The time at peak maximum (t_{max}) is the time when the largest exothermic or endothermic energy flow is measured during photopolymerization. It indicates when the most intense chemical reaction takes place after the start of the irradiation. The time at 95% conversion (t_{95}) describes when the chemical reaction is nearly finished. It is defined as the time when 95% of the curve area is reached.
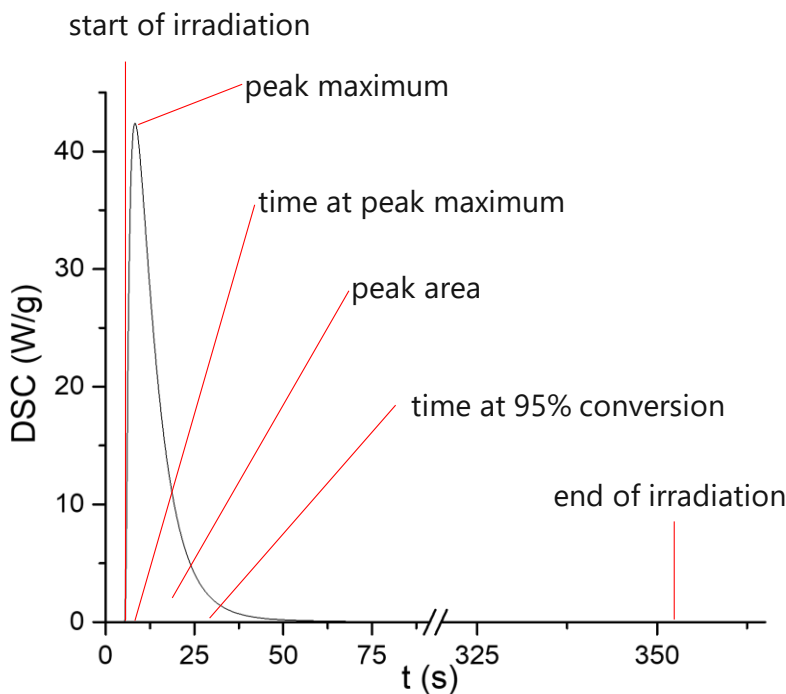
Figure 30: Photo-DSC measurement curve with notable points.

Due to the high melting points of the liquid crystalline monomer, the measurements were performed at 120 °C. An irradiation time of 360 s was chosen to ensure a complete reaction. The results are listed in Table 1.

Table 1: Photo-DSC measurement results of the LCEM3 monomer in combination with various difunctional thiol monomers. Molar amounts refer to the reactive groups and therefore are twice the amount of molar amounts of monomers.

Formulation	t_{max} (s)	t_{95} (s)	Peak area (kJ mol^{-1})
LCEM3 + HDT	8.2±0.1	67.4±2.6	82.9±1.3
LCEM3 + EDDT	8.3±0.2	34.7±2.8	72.7±3.8
LCEM3 + TBBT	15.1±0.5	163.7±13.9	23.5±2.5
LCEM3 + DTT	11.2±0.3	102.3±9.0	23.4±0.9
LCEM3 + EBTG	7.8±0.1	34.0±2.9	57.5±3.7
LCEM3 + BMEE	8.5±0.3	37.8±2.9	66.0±4.8
HDT + DAT (ref.)	8.0±0.2	27±1	82.2±3.6

The largest peak area was observed for the LCEM3-HDT formulation (83 kJ·mol^{-1}). It was within the margin of error for the performance of the HDT-DAT reference system. Formulations incorporating ether/ester-based monomers EDDT, EBTG, and BMEE were also found to have high peak areas ranging from 58 to 73 kJ·mol^{-1}. The reactivity was low for the aromatic TBBT and OH-containing DTT monomers, which are both solid at room temperature. The time at maximum peak height correlated well with the peak area except for the LCEM3-EBTG monomer combination, which had a slightly faster reaction speed than all other tested formulations while having a lower peak area than most other formulations. The time at 95% conversion was unexpectedly high for the LCEM3-HDT monomer combination. For the other formulations, a low t_{95} coincided with a high peak area, except for the LCEM3-EBTG formulation, which once again showed a faster reaction time than the other formulations.

Formulations containing HDT, EDDT and BMEE exhibited the highest peak areas, which leads to the possibility that simple, linear dithiols with no side groups are generally well suited for thiol-ene polymerization, and that more complex structures may have a negative influence on the conversion of functional groups in the formulation. With this hypothesis in mind, the ester side group of EBTG did not have a large negative impact.

Considering the much lower peak areas of the TBBT and DTT-containing formulations, it is possible that multiple effects contributed to the decreased reactivity. In TBBT, the thiol group is in α position to an aromatic ring, as opposed to an aliphatic CH_2 group present in all other thiols, which could be a reason for the lowered reactivity due to resonance effects of the aromatic structure. Another chemical difference is the thioether bond, which connects the aromatic rings. However, it is unlikely that the thioether, which is relatively inert to radical reactions, had a negative impact on the polymerization. The formulation containing DTT had a similarly low peak area. The only chemical differences between DTT and the best-performing HDT is the presence of hydroxyl groups and the main chain length. As demonstrated by Childress et al.,[1] a variation of the chain length only has a

small impact on the polymerization of thiol-ene systems. Therefore, it can be concluded that the hydroxyl groups are responsible for the decrease in reactivity.

2.2   Molecular weight *via* gel permeation chromatography

Gel permeation chromatography (GPC), or size exclusion chromatography, is a method to sort macromolecules by their size in solution, thus determining the molecular weight of polymers. The dissolved polymer samples are moved through a column that uses a porous gel as a stationary phase, which holds back smaller molecules while larger molecules can pass through more easily. The varying retention of the polymer chains in the gel enables the calculation of the average molecular weight. Number average (M_n) and mass average molar mass (M_w) can both be determined *via* GPC. The fraction of both values yields the dispersity ($Đ_M$), which gives information about the size heterogeneity of the macromolecules. Calibration of the measurements is either performed with a polystyrene standard for relative molecular weight comparisons, or through absolute methods like triple detection, where multiple detectors measure the retention volume of the same sample at different concentrations. A calibration is thus established, which enables the calculation of the true molecular weight of the sample.[66]

The photo-DSC samples were dissolved in THF for GPC evaluation. While the LCEM3-HDT sample could briefly be dissolved when heating, the polymer precipitated from the solution while cooling to room temperature. Therefore, it could not be measured. All remaining samples were soluble in THF and were evaluated using conventional calibration. The results are listed in Table 2.

Table 2: GPC results of LCEM3 in combination with various thiols. LCEM3-HDT could not be dissolved at room temperature. All results were evaluated via conventional calibration.

Formulation	M_n (kDa)	M_w (kDa)	$Đ_M$	Average molecular weight of monomer (g/mol)	Calculated no. of repeating units
LCEM3 + EDDT	10.2	25.1	2.5	418.6	24.4
LCEM3 + TBBT	4.0	5.0	1.2	452.5	8.8
LCEM3 + DTT	3.7	4.9	1.3	404.6	9.1
LCEM3 + EBTG	5.7	12.3	2.2	432.6	13.2
LCEM3 + BMEE	11.1	26.8	2.4	396.6	28.0

The lower solubility of the LCEM3-HDT sample may point to longer polymer chains. This correlates with the highest peak area measured by photo-DSC. However, the chain length could not be calculated as the polymer precipitated from the solution while cooling to room temperature.

The highest molecular weights were measured for the EDDT and BMEE-containing formulations, where number average molecular weights of over 10 kDa were observed. The rest of the monomers had much lower molecular weights, with TBBT and DTT at lower number average molecular weights than EBTG. The highest number of repeating units was calculated for the BMEE-containing polymer.

Additionally, the elugrams showed a multitude of peaks, which points to an incomplete polymerization for most samples (Figure 32). This effect was especially prominent for the lower molecular weight samples, while the EDDT and BMEE samples had a large initial peak followed by smaller oligomer peaks. The elugram of EBTG shows that some polymer chains were able to build up to a significant length, but that the refractive index signal was spread out widely across the elugram.
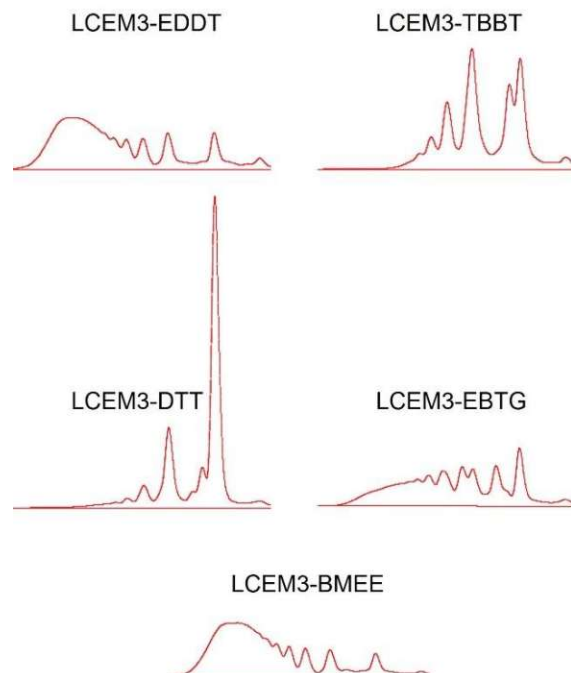
Figure 31: GPC elugrams of polymers resulting from combining LCEM3 with various dithiols.

2.3 Conversion *via* NMR-spectroscopy

The samples polymerized during the photo-DSC measurements were analyzed for their functional group conversion by NMR-spectroscopy.

The difference in double bond peak integral area in the NMR spectra before and after the polymerization gives information about the degree of conversion of alkene groups (2). C is the conversion of double bonds in the sample during the reaction. A_{before} and A_{after} describe the double bond peak integral before and after irradiation, respectively. Both integrals were set relative to the peak of the benzene ring in LCEM3.

$$C = 1 - \left(\frac{A_{after}}{A_{before}}\right) \tag{2}$$

Both peaks that correspond to the terminal alkene double bond were integrated and compared to the pure monomer, which was recorded separately (Table 3).

Table 3: Conversion during polymerization of LCEM3 formulations as determined by integration of their peak areas in ^{1}H-NMR-spectroscopy. Peak 1 corresponds to the two hydrogen atoms on each terminal carbon atom at a chemical shift of 4.99. Peak 2 corresponds to the hydrogen on each of the carbon atoms next to the terminal carbon atom at a chemical shift of 5.85. The integral of the benzene ring at a chemical shift of 8.23-8.10 was set to 4 across all samples.

Formulation	Peak 1 integral	Peak 2 integral	Conversion 1 (%)	Conversion 2 (%)
LCEM3	3.70	1.79	-	-
LCEM3 + HDT	0.34	0.13	91	93
LCEM3 + EDDT	0.66	0.27	82	85
LCEM3 + TBBT	1.58	0.71	57	60
LCEM3 + DTT	2.52	1.21	32	32
LCEM3 + EBTG	1.13	0.57	69	68
LCEM3 + BMEE	0.55	0.25	85	86

The results of the two signals correlated well among each other and with the peak area values of the photo-DSC measurements. Thus, it can be plausibly concluded that the measurements have yielded reliable results. Degrees of conversion over 80% were reached in three samples: LCEM3-HDT, LCEM3-EDDT and LCEM3-BMEE. Again, the best performance across measurements was achieved by formulations incorporating simple, linear thiol monomers. Therefore, it can be concluded that this type of monomer is the most suitable for the polymerization with the LCEM3 monomer, and that more complex monomers, which contain bulky aromatic groups or hydroxyl groups, may influence the polymerization negatively. The best result was obtained for the LCEM3-HDT monomer combination at 91% conversion by NMR-spectroscopy. HDT and EDDT, which were the two most promising dithiol monomers by photo-DSC and NMR-spectroscopy, were selected for further experiments in combination with the LCEM3 monomer.

3   Polymer curing and characterization

Bulk polymerization experiments were performed to test the material properties of LCEM3 in combination with the two most promising thiol monomers, HDT and EDDT, as determined by photo-DSC and NMR-spectroscopy. After casting the formulations into a mold and photopolymerization at 120 °C, the HDT-containing formulation resulted in a stiff, crystalline, brittle material. The EDDT-containing formulation was even more brittle and formed cracks while cooling to room temperature. The obtained material did not have the structural stability to be prepared for mechanical tests. Therefore, experiments with the EDDT-containing formulation were not continued, and focus was set onto the formulation combining LCEM3 with HDT (Figure 32 a, b).

A study was laid out to perform a full characterization of the LCEM3-HDT formulation, its polymerization process, and the properties of the resulting polymer. Additionally, due to the foreshadowed brittleness of resulting materials from bulk experiments, a plan was devised to improve the toughness of the polymer by partially substituting the LCEM3 monomer with a more flexible monomer. The result should be a semicrystalline polymer with hard blocks responsible for structural stability of the polymer and soft blocks responsible for fracture toughness. Factors in the selection of these co-monomers were that they contain non-homopolymerizable reactive groups, exhibit flexible structures, are commercially available, and exhibit a relatively high molecular weight and boiling point, as the polymerization should take place at 120 °C. For this purpose, two monomers were chosen after thorough literature review: diallyl adipate (DAA, Figure 32 c) and allyl-functionalized pTHF with a molecular weight of ~2000 (APF, Figure 32 d).

a)

LCEM3

b)   c)   d)

HDT   DAA   APF

MW ~2000
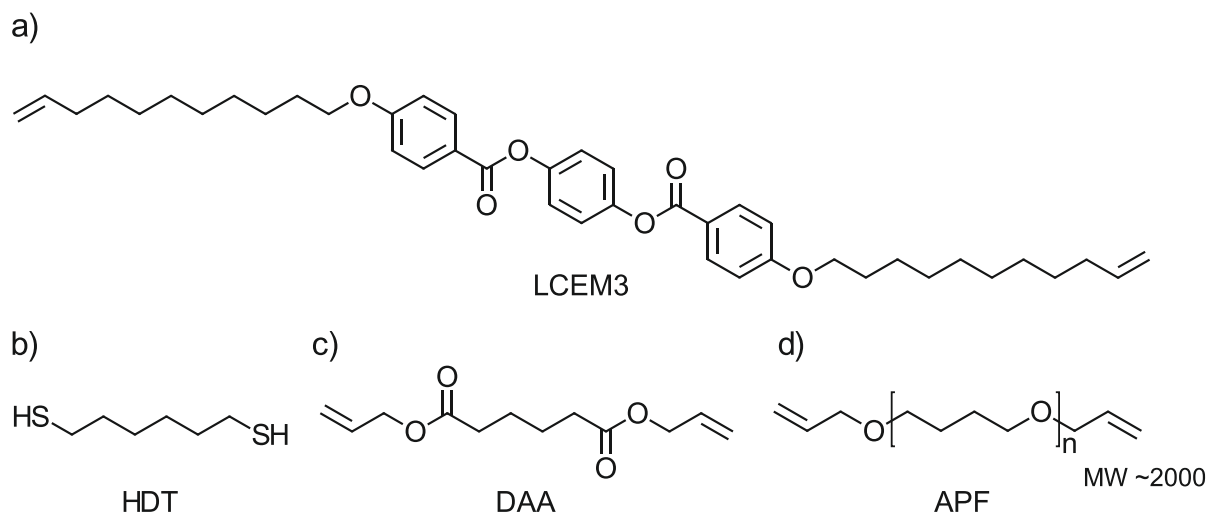
Figure 32: Monomers used for studies of polymerization behavior and polymer analysis in this work: a) liquid crystalline difunctional ene-monomer LCEM3, b) difunctional thiol monomer HDT, c) co-monomer diallyl adipate (DAA) used for partial substitution of LCEM3, d) co-monomer allyl-functionalized pTHF with a molecular weight of ~2000 (APF) used for partial substitution of LCEM3.

All formulations characterized in the study contained an equimolar amount of thiol and terminal alkene functional groups. LCEM3 was partially substituted by another difunctional terminal alkene monomer in varying concentrations (Table 4). The concentration of the additional monomer was decided upon review of the brittleness of the material obtained by initially substituting 50% of LCEM3. For APF, concentrations from 25 to 75 mol% were chosen. As the addition of 50 mol% diallyl adipate still yielded a brittle material, concentrations of diallyl adipate below 50% were not investigated. Instead, concentrations ranging from 50 to 90 mol% were analyzed. 1 wt% Ivocerin was added as a photoinitiator, and 0.1 wt% pyrogallol was added as a thermal stabilizer to all formulations.

Table 4: Monomer mixtures chosen for characterization. The base formulation LCEM3-HDT contains only LCEM3 and HDT in an equimolar amount. For all other formulations, LCEM3 was partially substituted by another difunctional alkene monomer (DAA or APF). The name and percentage of substitution of the additional monomer were used to form the name for these formulations. All formulations contained 1 wt% Ivocerin as a photoinitiator and 0.1 wt% pyrogallol as a thermal stabilizer.

Formulation	Terminal difunctional alkene monomer	Dithiol monomer	Additional monomer	Percentage of LCEM3 substituted by additional monomer (mol%)
LCEM3-HDT	LCEM3	HDT	-	0
50DAA	LCEM3	HDT	DAA	50
75DAA	LCEM3	HDT	DAA	75
90DAA	LCEM3	HDT	DAA	90
25APF	LCEM3	HDT	APF	25
50APF	LCEM3	HDT	APF	50
75APF	LCEM3	HDT	APF	75

The formulations were analyzed for their viscosity and thermal stability *via* rheology. Their photopolymerization behavior was investigated using photo-DSC and RT-NIR-photorheology. Gel permeation chromatography was used to analyze the molecular weight of the resulting polymers. The polymers were characterized further for their mechanical properties using tensile tests, and their phase transition behavior was investigated *via* DSC and *via* polarized optical microscopy. Finally, atomic force microscopy was performed to investigate a possible separation of phases in the polymers.

3.1   Viscosity and thermal stability of formulations

The viscosity of the formulations at polymerization temperature (120 °C) was measured by rheometry (Figure 33).

This was combined with a thermal stability study, as the formulations must be stable for multiple hours without spontaneously polymerizing in a typical hot lithography printing process. If thermal polymerization spontaneously sets in, an increase in viscosity is observed due to an increase in polymer chain length. The measurements were repeated two hours and five hours after the initial measurement for this purpose. Between measurements, the samples were stored at 120 °C.
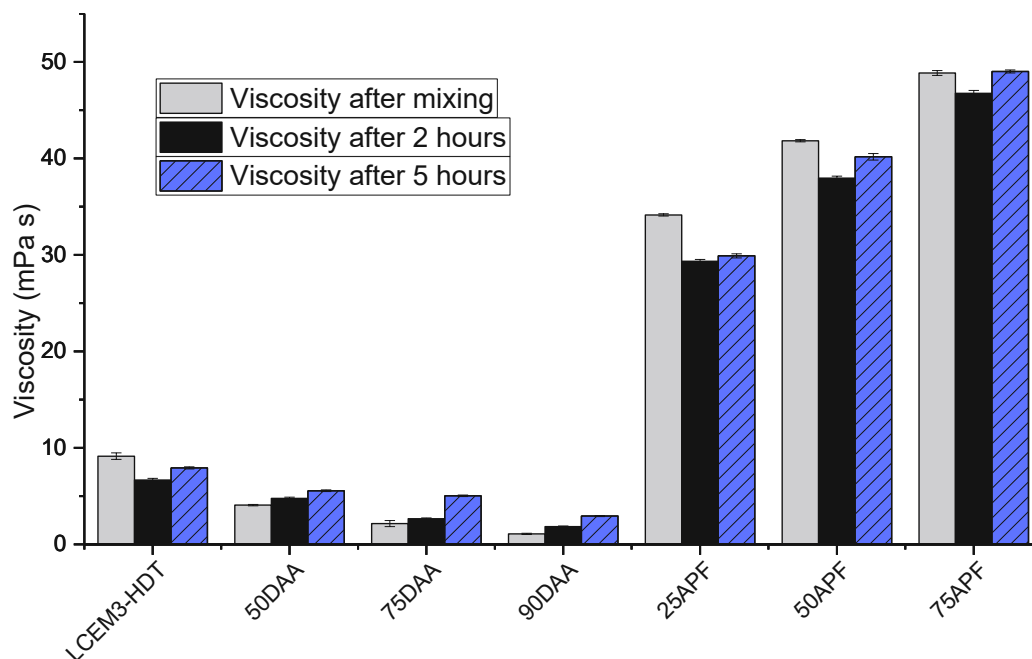
Figure 33: Viscosity at a measurement temperature of 120 °C of LCEM3-HDT formulations with varying amounts of substituted ene-monomers (50-90DAA, 25-75APF): after initially mixing the formulation (grey), two hours of storage at 120 °C (black), and after five hours of storage at 120 °C (textured blue).

All formulations exhibited a viscosity under 50 mPa s, which is well below the upper limit of viscosity for additive manufacturing using stereolithography (4.5 Pa s).[67] The pure LCEM3-HDT formulation exhibited a viscosity under 10 mPa s. Depending on the

monomer that was used to partially substitute LCEM3, a decrease in viscosity was found for increasing DAA-content formulations and a strong increase in viscosity was found for the formulations where LCEM3 was partly substituted by increasing amounts of APF. A larger amount of DAA in the formulation caused a further decrease in viscosity while a larger amount of APF in the formulation caused a further increase. This was expected due to the much higher molecular weight and chain length of APF compared to DAA.

Regarding the thermal stability, a decrease in viscosity during the measurement after two hours of storage at 120 °C was observed for all measurements of the pure LCEM3-HDT formulation while a small increase was observed after storing the same samples for another three hours. This could possibly be attributed to a temperature difference of the rheology stamp during the different measurements, as only the temperature of the sample surface could be determined accurately. An onset of thermal polymerization was not detected as the viscosity of later measurements remained below the viscosity of the initial measurement before storage.

For samples that contained DAA, an increase in viscosity was observed over time. Compared to the initial measurement, the increase was large especially in the 75DAA formulation. This could signify an initiation of thermal oligomerization in part of the sample. However, the overall viscosity remained lower than that of the LCEM3-HDT formulation, which suggests no threat for the viscosity requirement for Hot Lithography.

The same effect seen for the LCEM3-HDT formulation was also observed in APF-containing formulations. Compared to the initial measurement, a decrease of viscosity after two hours of storage was followed by a minor increase in viscosity in the measurement after an additional three hours of storage. Neither of the measurements after storage at 120 °C showed a higher viscosity than the initial measurement. It is likely that small differences in the measurement temperature were the reason for these deviations. Generally, it can be concluded that the thermal stabilities of all formulations are sufficient for the requirements of a hot lithography printing experiment.

3.2 Photoreactivity analysis

3.2.1 Photo-DSC

To test the reactivity and polymerization properties of the various formulations derived from LCEM3-HDT, a photo-DSC study was performed (Table 5, Figure 34). Analogous to chapter 2.1, the measured parameters are peak area per mole double bonds as a measure of reactivity, the time at maximum intensity (t_{max}), and the time at 95% conversion (t_{95}) as a measure of reaction speed. Normalization of the peak areas to mole reactive groups is especially important when monomers with large differences in molecular weight are used, as it is the case for diallyl adipate (226 g·mol⁻¹) and pTHF at (~2000 g·mol⁻¹). Measurements were again performed at 120 °C with an irradiation period of 360 s.

Table 5: Results of photo-DSC measurements of LCEM3-HDT formulations with varying amounts of substituted ene-monomers. Molar amounts refer to the reactive groups and therefore are twice the amount of molar amounts of monomers.

Formulation	t_{max} (s)	t_{95} (s)	Peak area (kJ·mol⁻¹)
LCEM3-HDT	8.2±0.1	67±3	83.0±1.3
50DAA	8.6±0.0	67±21	63.4±7.8
75DAA	7.6±0.3	24±1	49.5±5.7
90DAA	7.5±0.2	25±1	62.5±13.0
25APF	9.5±0.2	56±7	72.4±3.4
50APF	9.8±0.7	30±3	66.7±5.2
75APF	10.0±1	33±2	71.9±8.4
HDT-DAT (ref.)	8.0±0.2	27±1	82.2±3.6
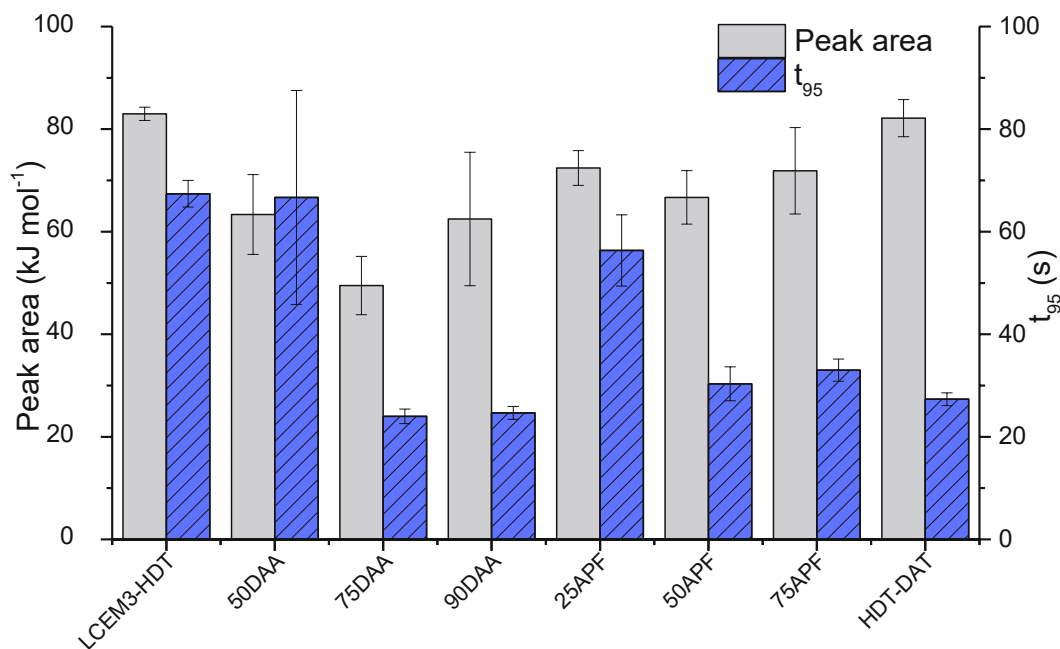
Figure 34: Peak area (grey) and time at 95% conversion (textured blue) results for photo-DSC measurements.

All diallyl adipate-containing samples exhibited comparatively low reactivity with peak areas ranging from 50 to 63 kJ mol^{-1}. Allyl-functionalized pTHF-containing formulations outperformed them with peak areas ranging from 67 to 72 kJ mol^{-1}. The highest peak areas were observed for LCEM3-HDT and the reference formulation HDT-DAT.

As seen in the samples LCEM3-HDT, 50DAA and 25APF, a higher concentration of LCEM3 loosely correlated with a higher t_{95}. The lowest t_{95} was observed for the samples 75DAA and 90DAA, comparable to the HDT-DAT reference sample. However, these two samples were also the least reactive of all samples, pointing to a rapid onset of polymerization also demonstrated by their low t_{max}, but possibly an incomplete conversion of reactive groups. An explanation for this difference in behavior could be the low molecular weight of the DAA monomer, which, due to its low viscosity, has a high mobility in the molten formulation, which causes a large number of reactive groups to be exposed to each other quickly. Compared to this, the APF-containing formulations contain long pTHF chains, which take more time to arrange before polymerization. A possible explanation for the higher final conversions reached by the APF formulations is the gel point, which is reached

later for the flexible APF-containing systems, allowing for more reactive groups to polymerize. Another explanation could be the higher concentration of photoinitiator relative to the number of reactive groups in the APF-containing samples, as a 1 w% concentration was used for all samples.

A generally low t_{max} around or below 10 s and the highest t_{95} of 67 s across all samples confirmed that the photopolymerization could fully take place within the irradiation time of 360 s.

3.2.2   RT-NIR-photorheology

Real time near infrared photorheology is a powerful method capable of observing chemical and mechanical characteristics of monomer mixtures during the polymerization process. A translucent sample plate enables the irradiation of the sample from below and the recording of IR spectra during a rheology measurement (Figure 35).
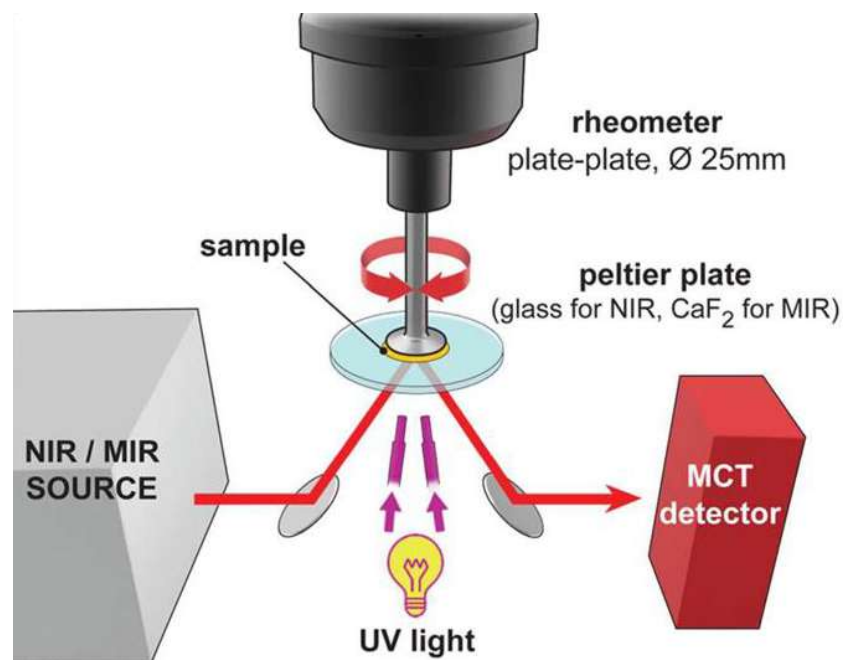
Figure 35: RT-NIR-photorheology measurement setup.[68]

Temperature control of the sample during measurements is enabled through a peltier sample plate and an external heating hood. The rheology instrument measures the dynamic modulus and shrinkage force of the formulation.

Reproducibility and error of measurements was determined empirically by Gorsche et al., who reported errors for time of gelation at typically lower than 5%, and errors of final modulus and shrinkage force below 20%.[68] Due to a lower signal-to-noise ratio than typically observed, an error in the calculated conversions of up to 10% was reported for thiol-ene systems. [68]

The dynamic modulus G* describes the stress-strain behavior of viscoelastic fluids under oscillatory shear. It consists of the storage modulus G′, which describes the amount of deformational energy that is stored in the sample upon shear strain, and the loss modulus G′′, which describes the amount of deformational energy that is converted into heat through internal friction (3).

$$G^* = G' + i \cdot G''$$ (3)

The gel point is reached when the storage modulus is higher than the loss modulus. Using near-infrared spectroscopy, it is possible to determine the double bond conversion (DBC) by integration of the double bond absorption band (6064-6186 cm^{-1}) over time.[68]

Measurements were performed at 120 °C with a light intensity of 35 mW cm^{-2} at an irradiation time of 300 s. The results are listed in Table 6. Due to the high measurement temperature, not all measurements exhibited a gel point. Additionally, for some samples, a double bond conversion higher than 100% was calculated.

Table 6: Results of RT-NIR-photorheology measurements of LCEM3-HDT formulations with varying degrees of substituted ene-monomers measured at 120°C. G'$_{max}$ and G''$_{max}$ are the highest storage modulus and the highest loss modulus reached during each measurement, respectively. DBC is the double bond conversion calculated by integration of the IR spectra. t$_{95}$ is the time after which 95% conversion was reached, calculated by integration of the IR spectra.

Formulation	Gelation time (s)	DBC$_{gel}$ (%)	t$_{95}$ (s)	DBC (%)	G'$_{max}$ (MPa)	G''$_{max}$ (MPa)	Shrinkage force (N)
LCEM3-HDT	16	96	0.9	96	1652800	207230	-4.97
50DAA	25	100 [2]	2.3	100 [2]	796490	127467	-0.85
75DAA	- [1]	- [1]	1.6	99	171	879	-0.03
90DAA	- [1]	- [1]	2.0	99	940	1633	-0.01
25APF	75	100 [2]	2.7	100 [2]	1289	1174	-0.05
50APF	- [1]	- [1]	6.7	100	772	1050	-0.01
75APF	- [1]	- [1]	10.9	99	1.4	25	0.00
HDT-DAT ref.	- [1]	- [1]	3.4	100 [2]	507	2156	0.00

[1] gel point not reached
[2] conversion calculated as > 100%

Crystallinity of the samples exhibited a drastic influence on the rheological properties of the samples. Samples with a high content of the highly crystalline LCEM3 monomer demonstrated much larger maximum moduli and shrinkage forces. With a lower content of LCEM3, a late gel point or no gel point was observed. For the images (Figure 36-Figure 38) a logarithmic scale was used whenever an increase in storage and loss modulus of more than four orders of magnitudes was observed. Graphs of all photorheology measurements are listed in the appendix (A 1, A 2).

The LCEM3-HDT sample, which contained the largest amount of the highly crystalline LCEM3 monomer, exhibited the highest maximum storage and loss modulus (Figure 36). The gelation time was also shorter than that of any other sample. Additionally, a significant shrinkage force was observed. This is likely caused by a rapid crystallization of

the sample, which takes place soon after the start of the irradiation. It is likely that the crystallite melting point of the polymer is significantly higher than the measurement temperature. This is also substantiated by the short t_{95} and lower double bond conversion of the formulation compared to other samples, which can be explained by the decreased mobility of polymer chains after the gel point is reached.
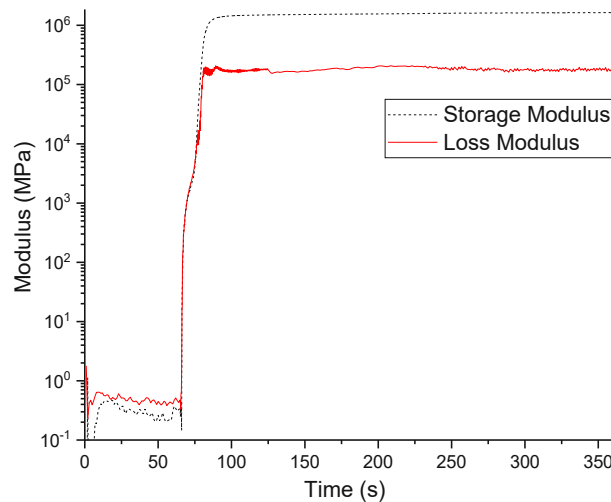
Figure 36: Photorheology measurement of LCEM3-HDT. Irradiation started after 60 s.

For the HDT-DAT reference formulation a higher maximum loss modulus was observed compared to the storage modulus. Therefore, a gel point was not reached. No shrinkage force was detected by the measurement instrument. This is explained by the absence of a gel point, which causes the polymer chains to relax quickly after shrinkage by polymerization, so the shrinkage force is counteracted by relaxation. The maxima of both the storage and the loss modulus were multiple orders of magnitude lower than the ones measured for the LCEM3-HDT formulation. These differences in rheological properties during the polymerization are explained by the rigid mesogenic group present in LCEM3, which is not part of the HDT-DAT reference formulation.

The DAA-containing samples showed large variations among each other based on the DAA content. The 50DAA formulation had high storage and loss moduli, a large shrinkage force compared to most other samples, and a gel point that was reached relatively quickly

(Figure 37 a). For both other DAA-containing formulations, no gel point was observed, as the loss modulus remained higher than the storage modulus throughout the measurement (Figure 37 b). The defining factor of the difference between the 50DAA sample and the other DAA-containing formulations is the content of the highly crystalline LCEM3 monomer. An unexpected result were the low maximum storage and loss moduli for the 75DAA sample, which were lower than for both the higher and lower DAA-content samples. Double bond conversions were high for all DAA-containing samples (99-100%), and no clear trend was observed for the t_{95}, which was measured at around two seconds for all samples. This was higher than the than the LCEM3-HDT sample. This can be explained due to LCEM3-HDT's quick crystallization, which may have resulted in an earlier termination of the reaction compared to the DAA-containing samples. It is possible that the integration method yields slightly different results due to the allyl group present in DAA compared to the aliphatic terminal double bond in LCEM3, or that the monomer itself has a lower rate of reactivity.
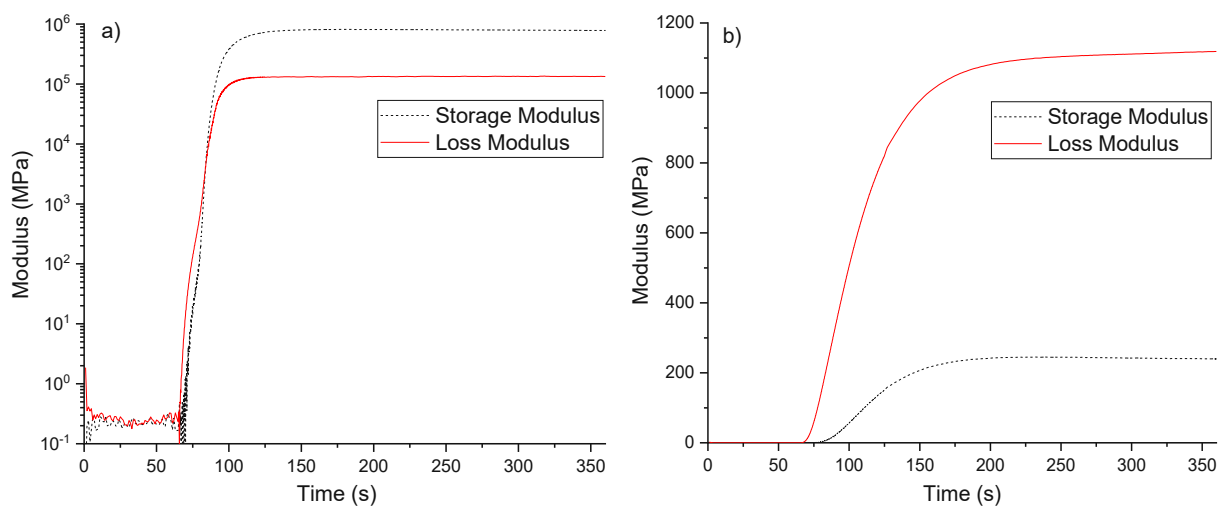
Figure 37: Photorheology measurement of a) 50DAA and b) 75DAA. Irradiation started after 60 s.

For the 25APF sample a gel point was observed after 75 s (Figure 38 a), which was the slowest of all samples where a gel point was reached. A relatively low maximum storage and loss modulus occurred for the 25APF sample, which could be explained by the high molecular weight of allyl-functionalized pTHF, which causes a large volume of the 25APF

sample to have soft elastomeric properties at the measurement temperature. At 169 seconds after the start of the irradiation, another crossover point of the storage and loss modulus curves was observed, after which the storage modulus remained below the loss modulus. The gelation of the sample was therefore undone with the relaxation of the sample's polymer chains. No gel point was reached for the 50APF and 75APF formulations. While the 50APF formulation still exhibited a maximum storage and loss modulus comparable with most of the other samples that did not show a gel point, the 75APF sample had extremely small maximum moduli with a maximum storage modulus at slightly higher than 1 MPa (Figure 38 b). Conversions throughout the APF-containing samples were high, while t_{95} values increased significantly with a higher APF content. This can be explained by the higher viscosity of the formulations (Chapter 3.1).
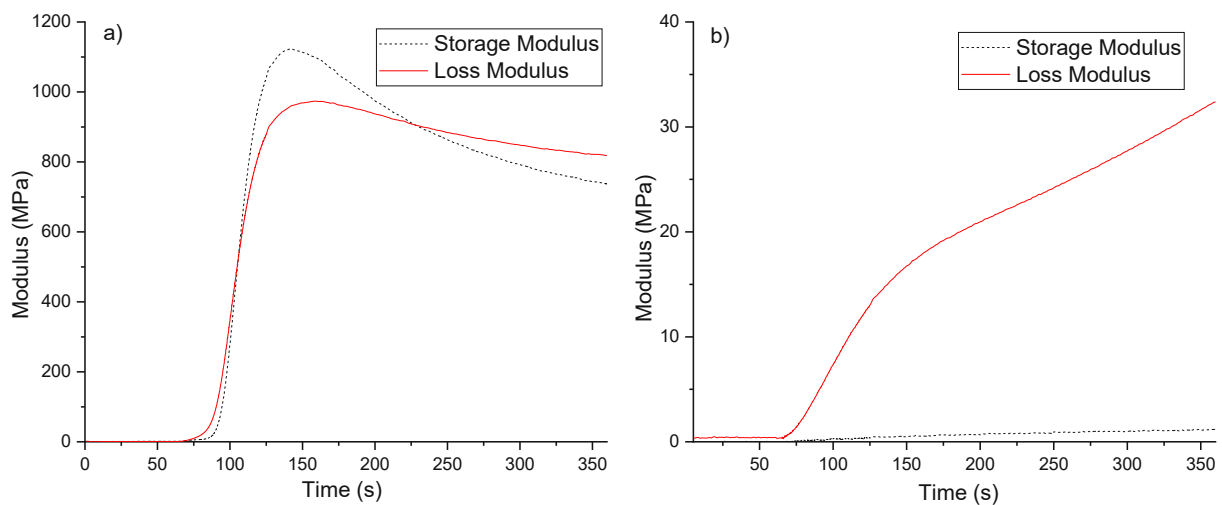
Figure 38: Photorheology measurement of a) 25APF and b) 75APF. Irradiation started at 60 seconds.

The double bond conversion above 100% calculated for some samples may have been caused by a large shift in the baseline of the samples during polymerization. This could have caused the baseline correction to yield inaccurate results.

3.3　Molecular weight *via* gel permeation chromatography

For GPC, analysis, tensile test samples were used. These bulk samples were cured in an Uvitron UV floodlight after melting and homogenizing the formulations. Three formulations could be analyzed by GPC using THF as a solvent, the rest of the samples could not be dissolved in THF at room temperature. In addition to the conventional calibration with a polystyrene standard (conv.), triple detection (triple det.) analysis was attempted for all samples but could only be successfully performed for the APF–containing polymers. The remaining samples were not soluble in THF at room temperature and could therefore not be measured. The results are listed in Table 7.

Table 7: GPC analysis of all polymers soluble in THF. M_n is the number average molecular weight; M_w is the mass average molecular weight. $Đ_m$ is the dispersity of the polymer chain. The calculated number of repeating units was determined by dividing the number average molecular weight by the average molecular weight of the monomers.

Formulation	M_n (kDa)	M_w (kDa)	$Đ_M$	Average molecular weight of monomer (g/mol)	Calculated no. of repeating units
90DAA (conv.)	5.5	29.9	5.4	209.7	26,2
50APF (conv.)	11.5	24.9	2.1	738.8	15,6
50APF (triple det.)	4.9	10.9	2.2	738.8	6,6
75APF (conv.)	12.9	29.0	2.2	907.0	14,2
75APF (triple det.)	6.4	25.1	3.9	907.0	7,1

Due to the limited solubility of the polymer samples in THF, the samples were dissolved in chloroform and measured through a GPC column in an HPLC instrument (Figure 39). All samples except 75DAA and HDT-DAT could be dissolved in chloroform. However, with no calibration curve such as the polystyrene standard, and only refractive index and UV-absorption detectors available, the results could only be compared to each other. Thus,

the time for the refractive index peak to reach the maximum after the injection time was compared for the samples (Figure 40).
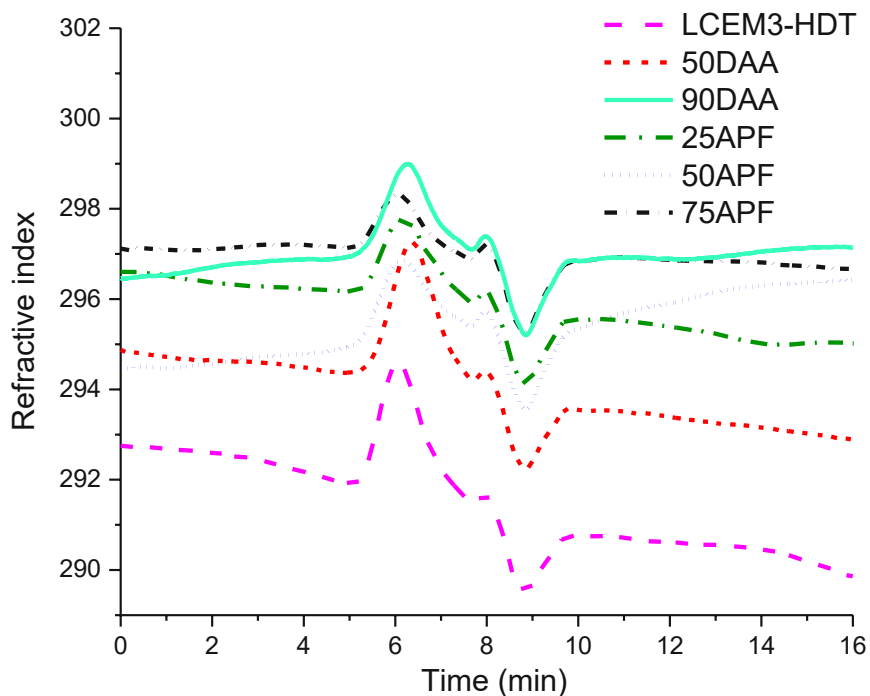
Figure 39: GPC elugrams of polymer samples measured in chloroform.
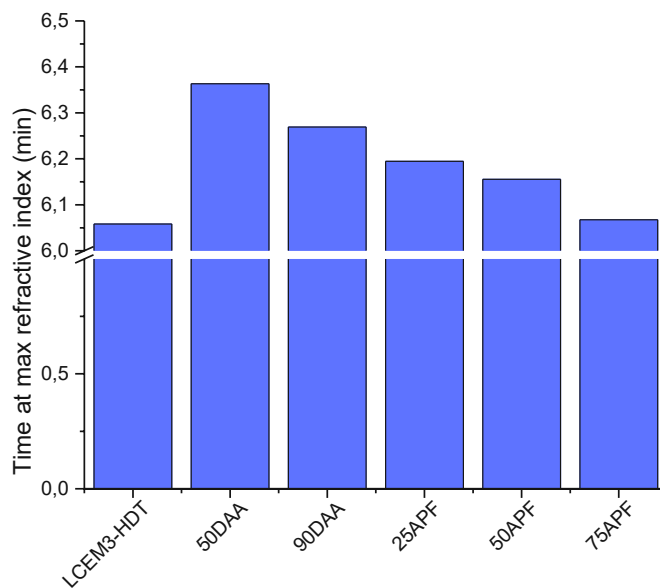
Figure 40: Time to reach the maximum refractive index after injection for GPC samples measured in chloroform.

57

For the samples measured in THF, broad peaks were observed with some smaller oligomer peaks following afterwards (Figure 41, appendix A 3-A 5). The highest molecular weights were observed for the LCEM3-HDT sample and for the samples containing APF, while lower molecular weights were observed for the DAA-containing samples. Generally, low molecular weights were observed when a smaller amount of non-LCEM3 ene-monomer was used in the sample, with an increasing molecular weight when using a larger amount of the co-monomer. A satisfactory correlation of results was found when comparing the samples that could be dissolved in both THF and chloroform.
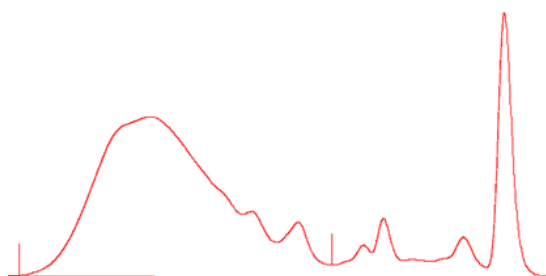
Figure 41: GPC chromatogram of 50APF polymer sample with a broad main peak and trailing oligomer/monomer peaks.

The LCEM3-HDT formulation could not be measured in THF, as it readily dissolved at higher temperatures, but precipitated again when cooling to room temperature. When measured in chloroform it exhibited the lowest retention time, which corresponds to the highest molecular weight of all samples. The simplicity of the monomer system could be a factor in its good performance, as minor inhomogeneities in a more complex three-monomer system could have potentially caused the termination of the polymerization in some areas, reducing overall chain length. The reference material HDT-DAT could not be dissolved fully in any solvent available for GPC measurements.

GPC analysis of the 50DAA sample could be performed when dissolving the sample in chloroform. Of the polymers made from DAA-containing formulations, only 90DAA could be dissolved in THF at room temperature. However, triple detection analysis of the 90DAA sample could not be performed, as the signal intensity required by the light scattering

detector could not be reached with the highest achievable sample concentration in THF. The 75DAA sample could not be fully dissolved in THF or chloroform. High retention times were observed during GPC analysis of 50DAA and 90DAA polymers, which suggests low molecular weights. In comparison with the polystyrene standard calibration, a number average molecular weight of 5.5 kDa was determined for 90DAA along with a very high dispersity (> 5). However, in samples where triple detection could be performed, conventional calibration with a polystyrene standard showed around double the number average molecular weights compared to the triple detection analysis. Following this trend, the true molecular weight of the 90DAA sample may also be much lower than determined using conventional calibration. Photo-DSC experiments (Chapter 2.1) suggest a diminished reactivity of the DAA-containing formulations, which is likely the reason for the reduced molecular weight of the resulting polymers.

For two APF-containing polymer samples (50APF and 75APF), triple detection could be performed to determine the true molecular weight of the polymers. The results (4.9 kDa for 50APF and 6.4 kDa for 75APF) were close to values reported in literature for linear thiol-ene polymers (3-6 kDa).[1] However, in these cases, the monomers had much lower molecular weights, implying that a much larger number of monomer units reacted to form an average chain. $Đ_M$ values around 2, which were measured for all APF-containing samples except for 75APF using triple detection, also matched the values reported in literature. The 25APF sample, which could only be dissolved in chloroform, had a higher retention time than the other APF-containing samples, corresponding to a lower molecular weight. A similar efficiency of polymerization was therefore encountered for the different APF-containing samples. However, a larger amount of APF in the sample resulted in a longer average chain length due to the initial molecular weight of the polymer. When comparing the results to the reactivities of APF-containing formulations measured *via* photo-DSC, no clear correlation could be found.

When comparing samples for which different co-monomers were used, it is possible for different functional groups in the polymer to influence the retention time in addition to

the molecular weight. Therefore, some samples may exhibit higher retention times than others, even though their molecular weights are similar. In the case of comparing the LCEM3-HDT polymer to 50DAA, however, it is likely that there was indeed a large difference in molecular weight, as the percentage of DAA in the formulation by weight was less than 20%. Thus, a large effect on the retention time by the functional groups of the monomer is unlikely. Polymers with a high LCEM3 content were generally not soluble in THF. This correlates with the solubility of the LCEM3 monomer, which by itself is also not soluble in THF and many other solvents, but readily dissolves in chlorinated solvents like chloroform or dichloromethane.

3.4   Thermomechanical properties

3.4.1   Tensile testing

The tensile strength and elongation at break of the polymers, which were chosen for the experiment due to the superior reactivity of the LCEM3-HDT formulation compared to other screened monomer combinations (Chapter 2) were evaluated. Additionally, six formulations that partially substituted LCEM3 with DAA or APF in attempt to increase the toughness of the polymers (Chapter 3, Table 4) were evaluated for their mechanical properties using tensile tests (Table 8, Figure 42-Figure 44).

Table 8: Tensile test results of LCEM3-HDT formulations with varying degrees of substituted ene-monomers.

Formulation	Ultimate tensile strength (MPa)	Elongation at break (%)	Toughness (kJ m^{-3})
LCEM3-HDT	3.65±1.41	0.90±0.23	19.6±12.1
50DAA	1.02±0.29	0.73±0.14	4.70±1.47
75DAA	1.85±0.76	4.15±0.96	58.2±26.1
90DAA	0.68±0.30	2.94±0.30	12.6±3.3
25APF	2.27±0.37	9.22±1.69	136.3±26.7
50APF	1.19±0.15	11.20±3.72	79.2±32.3
75APF	0.17±0.08	10.06±5.74	16.6±16.1
HDT-DAT ref.	10.2±0.7	343±145	27300±12300
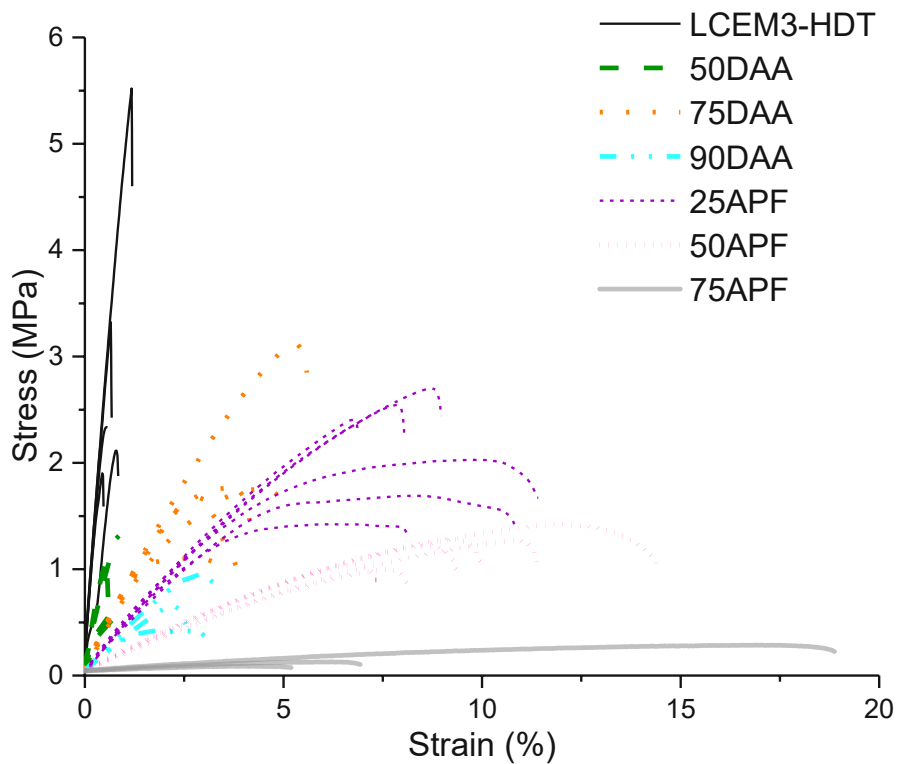
Figure 42: All stress-strain plots of LCEM3-HDT formulations with substituted ene-monomers.
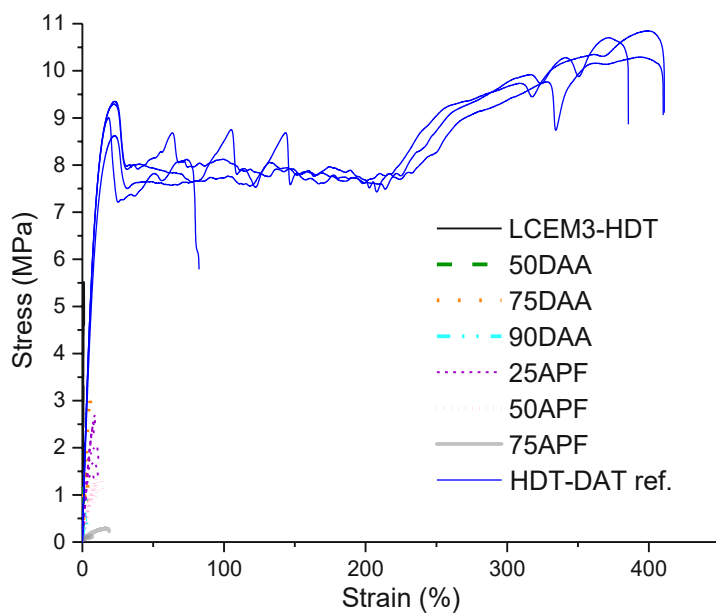
Figure 43: Stress-strain plots of LCEM3-HDT formulations with substituted ene-monomers including the

HDT-DAT reference material.
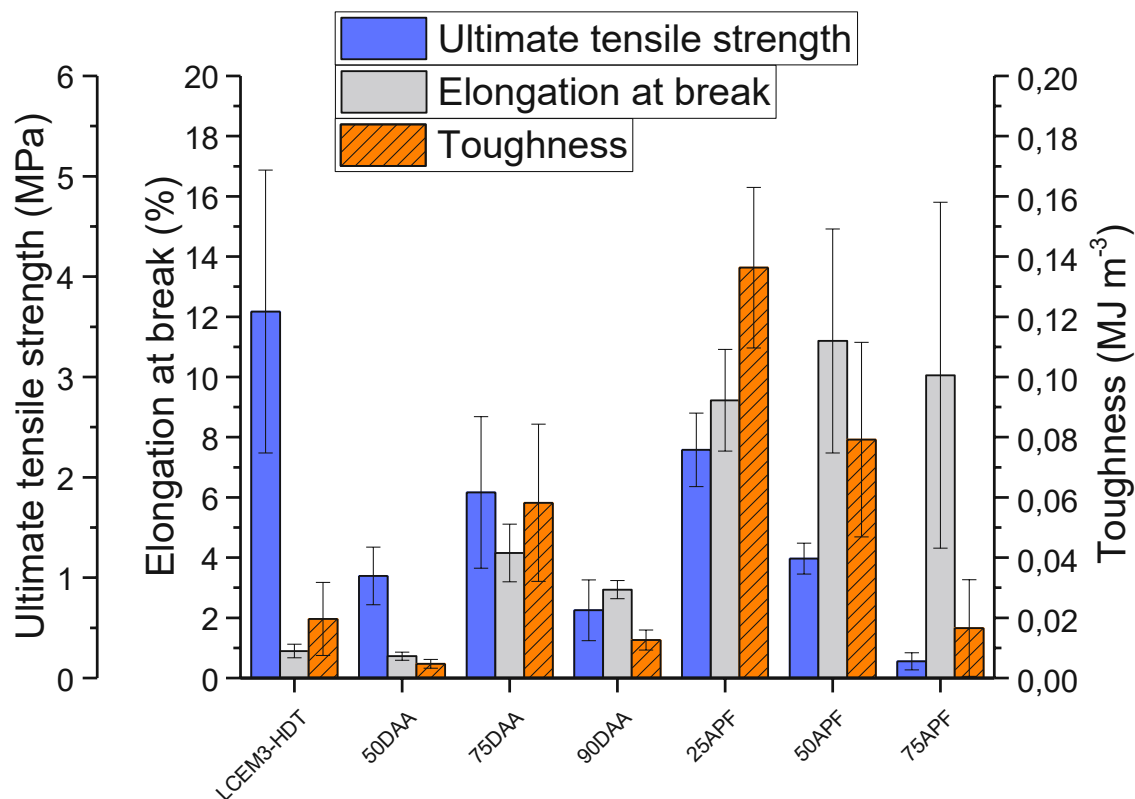
Figure 44: Average results of tensile tests of LCEM3-HDT formulations with varying degrees of substituted ene-monomers.

A large variation in the ultimate tensile strength was observed for some samples, partially due to the brittleness of the samples. This caused several of the samples to break when fixing them into the tensile testing instrument, reducing the number of samples that could be measured. DAA-containing samples generally performed worse than APF-containing samples, for some of which a balance of tensile strength and elasticity could be reached, which resulted in a noticeable increase in tensile toughness.

The LCEM3-HDT formulation proved to be hard and brittle with a strain at break of under 1% in most samples. This can be explained by the high content of the rigid crystalline mesogenic group present in LCEM3. Though the variation was high, the LCEM3-HDT polymer clearly demonstrated the highest ultimate tensile strength of all polymers, except for the HDT-DAT reference sample. The reference sample showed a tensile strength of around 10 MPa with a remarkable plastic deformation starting at around 22% elongation,

which resulted in significant necking of the samples. The elongation then extended up to around 400% for most samples, at which point the material failed.

When partially substituting LCEM3 with diallyl adipate, the strain at break was not improved at a concentration of 50 mol%, which yielded a very brittle and weak material. When substituting 75 mol%, a significant improvement in both tensile strength and strain at break was achieved compared to the previous specimen. With 90 mol% of LCEM3 substituted by DAA, both tensile properties worsened, indicating an ideal range of substitution around 75%. It is possible that at the ratio of monomers used in 75DAA the rigid properties of LCEM3 were partially retained while incorporating the elastic properties of DAA. In the 50DAA sample, the complexity of a three-monomer system could have caused issues in the polymerization, while not enough DAA was present to cause a noticeable toughening effect. For 90DAA, a decrease in the tensile strength was expected due to a higher content of the more elastic DAA monomer. However, it is unclear why no improvement in the elongation at break was observed for this sample.

When partially substituting LCEM3 with allyl-terminated pTHF, the elongation at break was improved to around 10% in all samples. The 25APF sample demonstrated the highest tensile strength of all samples where LCEM3 was partially substituted, in combination with a much higher elongation at break compared to LCEM3-HDT. This resulted in the highest tensile toughness of all LCEM3-HDT derived polymers. The tensile strength decreased significantly with increasing APF concentration, while the strain at break did not significantly increase. The poor performance of the 75APF sample could be explained by a relatively short polymer chain length. This could result in an inhomogeneous material, where the soft and hard segments in the polymer chain experience little entanglement. Normally, a larger elongation at break could be expected from a material with a high elastomer content. Additionally, a large variation in the elongation at break was observed, in part due to some of the samples breaking upon fixing them into the tensile testing instrument. This resulted in a low number of samples and therefore, a high variation of the results.

To analyze the thermomechanical properties of the samples further, a tempering experiment was performed. In semicrystalline polymers, a thermal treatment after the polymerization can lead to improved mechanical properties through stress relaxation mechanisms.[69] Therefore, an additional series of 50APF tensile test samples was subjected to a five-hour thermal treatment at 80 °C after polymerization, after which they were slowly cooled to room temperature. These samples were compared to a series of untreated samples (Figure 45, Table 9).
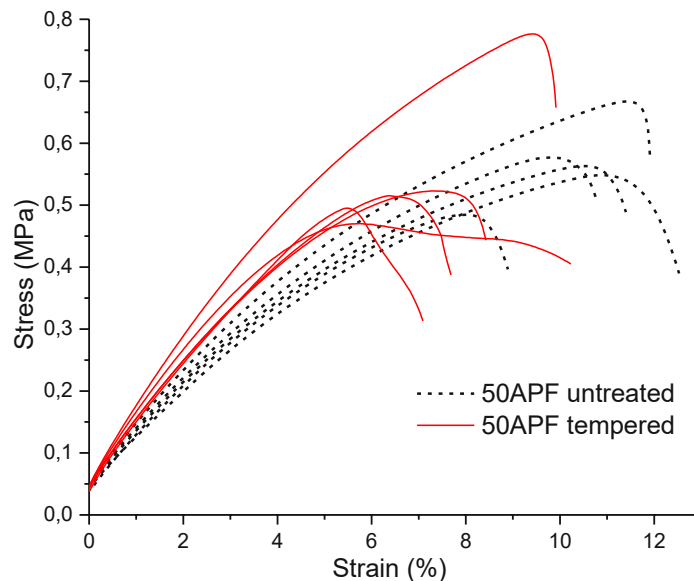
Figure 45: All stress-strain curves of untreated (dotted blue) and tempered (solid orange) 50APF samples in heat treatment experiment.

Table 9: Results of tensile tests of untreated and tempered 50APF samples.

Formulation	Ultimate tensile strength (MPa)	Elongation at break (%)	Toughness (kJ m^{-3})
50APF untreated	0.56±0.07	11.1±1.2	43.3±7.9
50APF tempered	0.56±0.11	8.7±1.2	33.9±9.5

The ultimate tensile strength of the tempered samples did not differ significantly from the untreated samples. The elongation at break of the tempered samples was ~20% lower on

average, which resulted in a lower tensile toughness. It can thus be concluded that the thermal treatment did not have the desired effect, as it only resulted in a decreased elasticity of the samples. Two parameters were changed compared to the original series of tensile tests: the tempering period, and the slower cooling rate. It is possible that the thermal treatment had an aging effect on the polymer, which caused an embrittlement of the material instead of the desired strengthening of the material. Slow cooling is usually responsible for relaxation of stresses in most materials, which results in more elastic properties. However, the combination of the thermal treatment with the slow cooling may have also caused an increase in crystallinity in the sample, leading to an embrittlement.

If the thermal treatment was indeed responsible for a worsening of the tensile properties, an experiment that explores the opposite conditions could be considered for the future: The samples could be heated for as short as possible when polymerizing them, and then rapidly cooled.

Additionally, a lower ultimate tensile strength was observed in all samples compared to the original series of tensile tests, where an average ultimate tensile strength of 1.19 MPa was measured for 50APF samples. A different batch of APF was used to prepare the samples used in the tempering experiment, which seemingly affected the tensile properties of the resulting material negatively.

3.4.2   Thermal analysis *via* differential scanning calorimetry

To detect phase changes in the polymer samples, thermal analysis of polymers was performed *via* differential scanning calorimetry (DSC). DSC measurements are relevant for thermoplastic materials, because the melting point determines the temperature range at which the material can be used and where it can be processed. It is possible that phase transitions like the glass transition temperature are visible in DSC measurement graphs.

For this measurement method, the sample is subjected to a temperature program along a reference chamber, typically filled with an empty DSC crucible of the same kind in which

the sample is located. The heat flow needed to keep the sample chamber at the same temperature as the reference chamber is measured and normalized by the sample mass. Thus, phase transitions can be detected. It is a similar method to photo-DSC (Chapters 2.1 and 3.2.1), with the difference that the sample is not investigated about its reaction to UV light, but instead for its reaction to temperature changes.

The samples were heated to 200 °C, cooled to -90 °C and then heated to 200 °C again. The phase transition temperatures observed in the DSC graphs during the second heating cycle are listed in Table 10. The second cycle is used to evaluate the phase transition temperatures after the first cycle erases the thermal history of the sample.

Table 10: Phase transitions observed via DSC during the second heating cycle. All noted phase transitions are endothermic, except when noted as "exo".

Formulation	Phase transition temperatures (°C)
LCEM3-HDT	88, 127, 131 (exo), 142, 150, 168
50DAA	92, 126, 137
75DAA	72, 90, 102, 113
90DAA	23, 32, 65, 96
25APF	20, 70, 90, 119, 145, 160, 172
50APF	22, 70, 90, 117
75APF	23, 60, 104
HDT-DAT ref.	-26, 58, 75

Many of the measured samples demonstrate a remarkable number of phase transitions. This large number could be explained by a broad distribution of the molecular weight, where different chain lengths could cause different melting points. Five different endothermic phase transition temperatures ranging from 88 to 168 °C were observed for the LCEM3-HDT formulation (Figure 46). Most were sharp spikes, except for the one at 150 °C, which was a weaker, broader signal. An exothermic peak was observed at 131 °C, which only appeared in the second heating cycle. Exothermic peaks usually point to decomposition reactions. However, the sample had been heated to 200 °C in the first

heating cycle. Therefore, it is unlikely that a decomposition would take place at a much lower temperature during the second cycle.

The HDT-DAT reference compound (Figure 46) showed three broad phase transition peaks. The signal at -26 °C could be the glass transition temperature. Afterward, two similarly shaped broad peaks were observed around 58 and 75 °C. They likely represent the crystallite melting point of the semicrystalline polymer. It is possible that a bimodal molecular weight distribution caused the signal to split into two distinct peaks. However, this could not be confirmed *via* GPC, due to the polymer not being fully soluble in THF or CHCl$_3$.
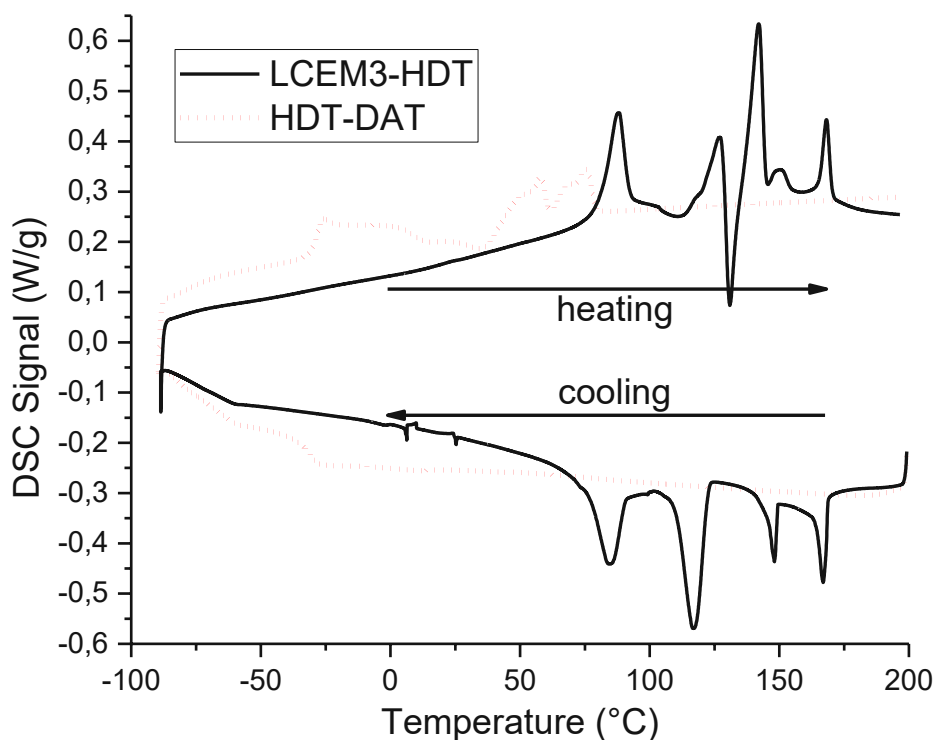
Figure 46: DSC measurement of the LCEM3-HDT and HDT-DAT polymers. Only the second heating cycle is displayed.

A decrease in the initial and final phase transition temperatures was observed for all DAA samples depending on the amount of diallyl adipate substituting LCEM3 (Figure 47). The initial phase transitions were lowered from 92 to 23 °C with increasing amounts of DAA,

while the final phase transitions decreased from 137 to 96 °C. The final phase transitions observed in all three samples were weak signals. Therefore, a strong effect of the LCEM3 content on the melting point of the resulting polymers was confirmed.
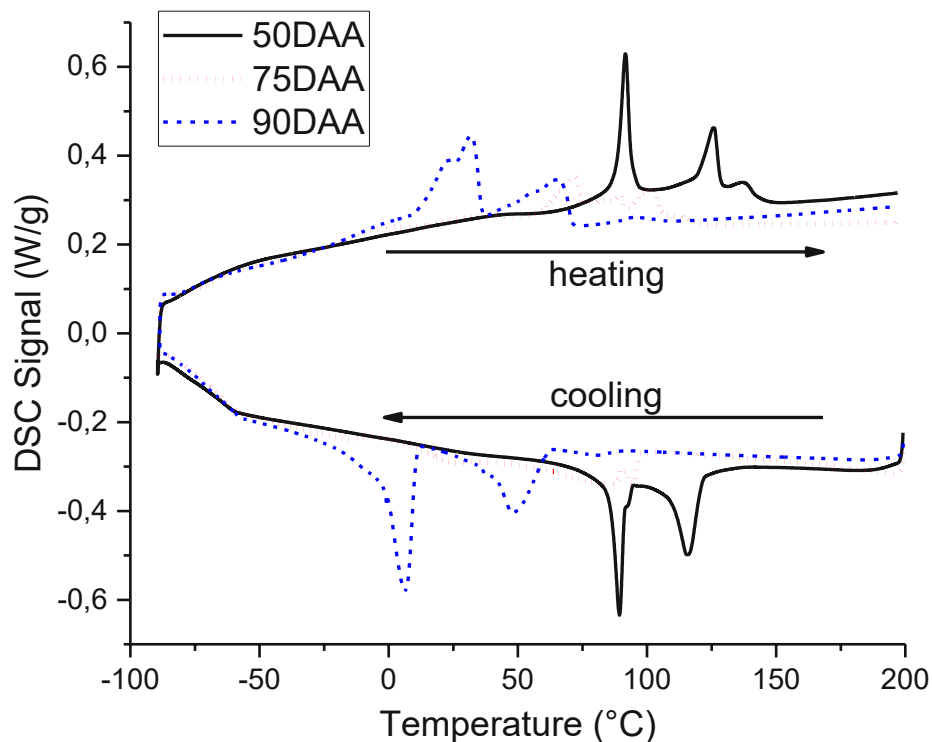
Figure 47: DSC measurement of the DAA-containing polymers. Only the second heating cycle is displayed.

For APF-containing samples, a strong influence of the LCEM3 substitution on the phase transitions was again confirmed (Figure 48). However, the lowest phase transition temperature (~ 20 °C) was shared by all three formulations. Therefore, it can be concluded that it is caused by the APF monomer, as the intensity of the peak also increases with increasing APF content. The 25APF sample exhibited a large number of phase transitions over a large temperature range. The first five transitions were distinct spikes, while the final two transitions were weak signals. It is possible that a large polydispersity is responsible for this large number of phase transitions. However, this could not be confirmed *via* GPC analysis due to the sample being insoluble in THF. The GPC measurements performed in chloroform did not have a sufficiently stable signal baseline

to enable a reliable evaluation of the dispersity. Four different phase transitions were observed for the 50APF polymer, of which the first one was the most intense signal at 22 °C. The following peak was a sharp spike at 70 °C, followed by two weak signals. The 75APF sample had a distinct spike at 23 °C. The transitions at 60 and 100 °C were low, broad signal peaks. This could be explained by the crystalline regions, which define the melting point and which are mostly influenced by the content of LCEM3 in the sample. Due to the low amount of LCEM3 in the sample, weak melting point signals can be expected.
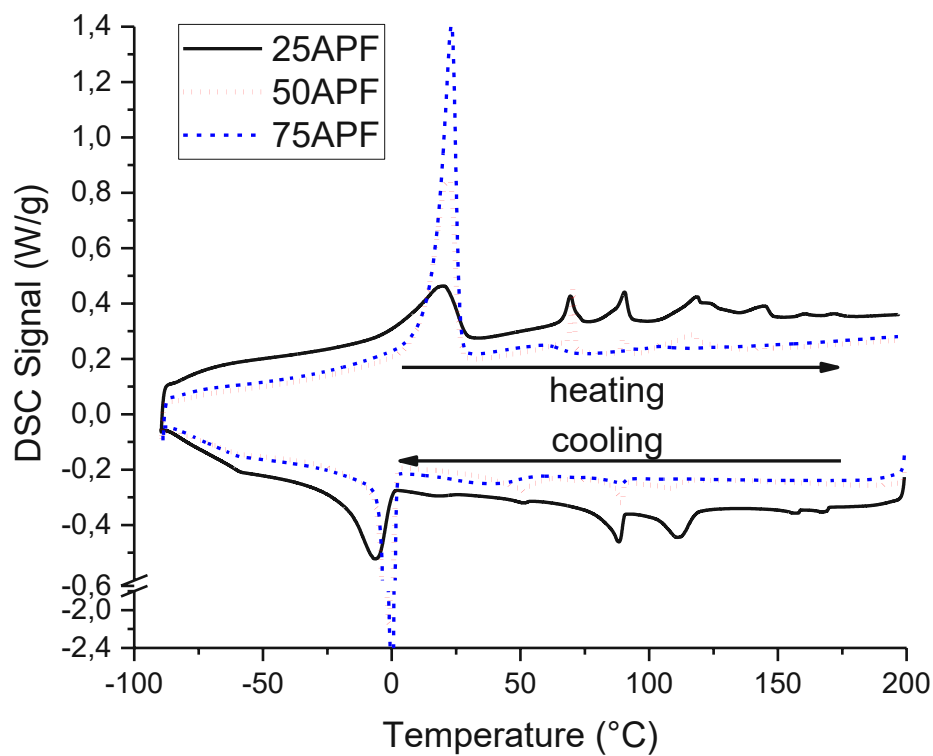
Figure 48: DSC measurement of the APF-containing polymers. Only the second heating cycle is displayed.

3.5   Phase analysis

3.5.1   Polarized optical microscopy

The polymer samples were analyzed on a polarized optical microscope with a heated stage (Figure 49-Figure 56). The observed phase transitions are listed in Table 11, where they are compared to the phase transition temperatures observed *via* DSC (chapter 3.4.2).

Table 11: Phase transitions measured on the polarized optical microscope in comparison with phase transitions measured by DSC. Wherever a phase transition measured on the microscope could be linked to a phase transition measured via DSC, it was recorded in the DSC column.

Formulation	Crystallite melting point (°C)		Fully isotropic melting point (°C)	
	Microscope	DSC	Microscope	DSC
LCEM3-HDT[1]	150-164	150	182	-
50DAA[2]	120-130	126	136	137
75DAA[2]	102-112	102	123	113
90DAA[2]	55-75	65	100	96
25APF[1,2]	130-135	119	171	172
50APF[2]	90-102	90	125	117
75APF[2]	55-60	60	112	104
HDT-DAT ref.	68-80	75	-	-

[1]Liquid crystalline phase between crystallite melting point and fully isotropic melting point
[2]Partially crystalline phase between crystallite melting point and fully isotropic melting point
[1,2]Liquid crystalline and partially crystalline phase present, phase transition at 148 °C

A crystallite melting point was observed on the microscope for all samples. In most cases, it could be linked reliably to a phase transition temperature measured by DSC (Chapter 3.4.2). The phase transitions from a liquid crystalline or partially crystalline phase to an

isotropic melt observed on the microscope also matched well with phase transitions measured *via* DSC.

The LCEM3-HDT polymer (Figure 49) started melting around 150 °C and was fully molten at 164 °C. During the phase transition, an opaque, viscous phase formed. At 164 °C, a transition into a colorful liquid crystalline phase was observed, which persisted up to 182 °C, where a transition into an isotropic molten phase took place. Thermal analysis by DSC identified a phase transition at 150 °C, which could be linked to the start of the crystallite melting range. However, the visible phase transition from liquid crystalline to isotropic could not be confirmed *via* DSC, where the final phase transition was measured at 168 °C. It is possible that the transition from a liquid crystalline phase to an isotropic molten phase only exhibited a minor amount of endothermicity. The high content of the highly crystalline LCEM3-HDT monomer is responsible for the high melting point of this polymer. Additionally, the large amount of mesogenic groups cause the material to clearly exhibit a liquid crystalline phase when molten. This long-range order in the molten phase persists up to a higher temperature than that of the pure monomer, which could be caused by the larger molecular weight of the polymer compared to the monomer, which limits the mobility that is responsible for an isotropic molten phase.

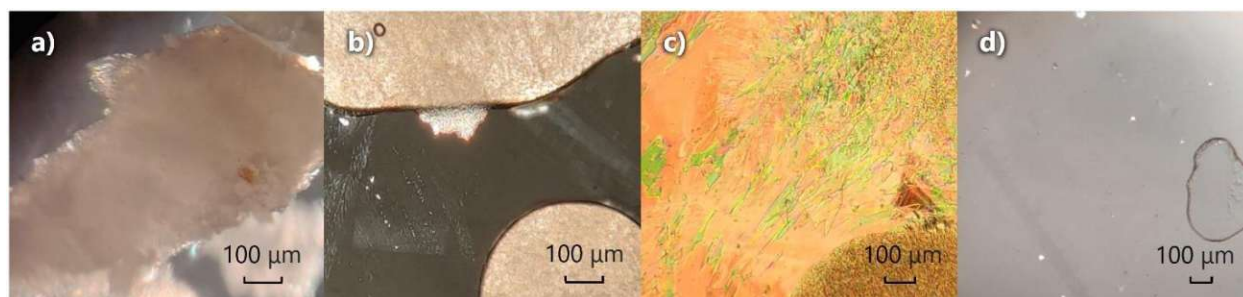*Figure 49: Phases of the LCEM3-HDT polymer observed on the polarized optical microscope: a) room temperature, b) 160 °C, c) 165 °C, d) 184 °C.*

The polymers in which LCEM3 was partially substituted with diallyl adipate (DAA) exhibited similar behavior to each other. As the melting point was reached, the material turned into an opaque phase (Figure 50 b, Figure 51 b, Figure 52 b). In this phase, densely

arranged birefringent areas were observed. These phases did not unambiguously represent liquid crystalline phases, as no distinct colors or maltese cross patterns were observed. It is possible that these phases consist of a partially crystalline phase in a molten matrix, or that the observed phases were indeed liquid crystalline. The birefringent areas vanished upon heating the sample further. The melting points and the phase transitions into an isotropic melt were observed at different temperatures depending on the content of DAA in the formulation. With higher DAA contents, the melting points decreased from 125 to 65 °C and the isotropic phase transition decreased from 136 to 100 °C.

Crystallite melting points overlapped well with phase transition temperatures measured *via* DSC for all samples, in which LCEM3 was partially substituted by DAA. The second to last DSC phase transition fit inside the melting range observed on the microscope for all three samples. The final phase transition measured *via* DSC matched well for the 50DAA and 90DAA samples, where there was a 1 °C and 4 °C difference, respectively. For the 75DAA sample, the transition to isotropic on the microscope was 10 °C higher than the transition measured by DSC. The crystallinity of the LCEM3 monomer had a strong influence on the DAA-containing polymers, as the melting points and the temperature of the transition into a fully isotropic phase increased with increasing LCEM3 content. Clearly discernible liquid crystalline phases were not found in the polymers, which could be explained by the higher stoichiometric contents of DAA. It is possible that the long-range order in the liquid phase is broken up by DAA monomers that are polymerized into the polymer backbone.

Figure 50: Phases of the 50DAA polymer observed on the polarized optical microscope at a) room temperature, b) 125 °C, and c) 135 °C.

Figure 51: Phases of the 75DAA polymer observed on the polarized optical microscope at a) room temperature, b) 108 °C, and c) 123 °C.
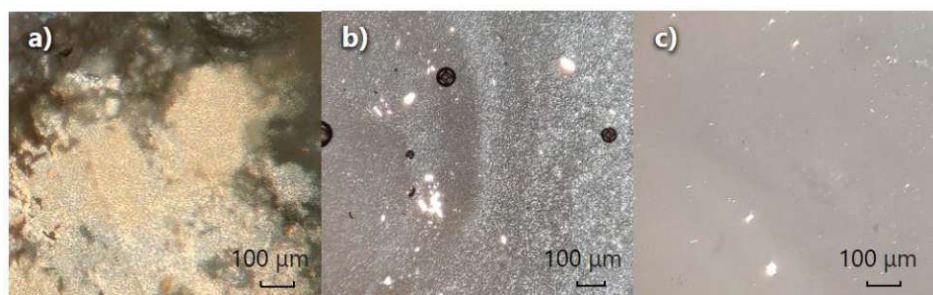
Figure 52: Phases of the 90DAA polymer observed on the polarized optical microscope at a) room temperature, b) 85 °C, and c) 103 °C.

For the polymer, in which 25% of LCEM3 was substituted by allyl-functionalized pTHF (Figure 53), a liquid crystalline phase was observed over large areas of the sample after the melting point, which was less distinct than the one observed for the LCEM3-HDT sample. At about 148 °C, a transition into a partially crystalline phase resembling previous samples took place. A transition into an isotropic molten phase took place at 172 °C. A very large number of phase transitions was measured for the 25APF sample *via* DSC, some of which correlated well with the phase transitions observed on the polarized optical microscope (~119-148 °C). The final phase transition into the isotropic melt matched well with the final phase transition measured *via* DSC, which happened at 171 °C.

The 50APF sample (Figure 54) exhibited similar behavior to the samples with DAA substituting LCEM3, with a partially crystalline phase forming at the sample's melting point. The melting range was observed from 90 to 102 °C, which matched a phase

transition observed *via* DSC (90 °C). The transition into a fully isotropic phase at 125 °C could be connected to a DSC signal (117 °C).

Almost no crystallinity was observed for the 75APF sample (Figure 55), which, at room temperature, appeared like the molten phases of most other samples. A melting process with a noticeable decrease in viscosity took place at 55-60 °C, which matched a phase transition observed *via* DSC (60 °C). A fully isotropic phase without any birefringent spots was reached at 112 °C, loosely matching a DSC signal (104 °C).

The influence of the LCEM3 content on the APF-containing polymers was clearly demonstrated. The melting point increased with an increasing amount of the LCEM3 monomer in the formulation, which also happened for DAA-containing samples. The 25APF polymer was the only sample that exhibited liquid crystallinity aside from the LCEM3-HDT polymer that included no co-monomers. The high LCEM3 content combined with the flexible pTHF chains could be responsible for the retention of the liquid crystallinity.
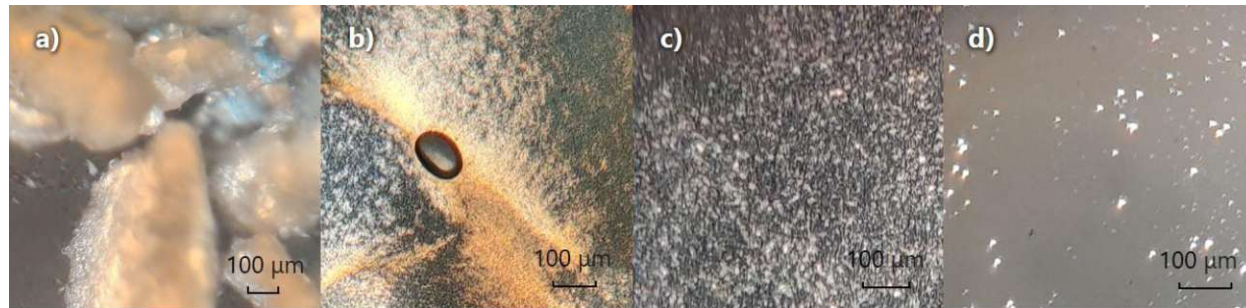
Figure 53: Phases of the 25APF polymer observed on the polarized optical microscope: a) room temperature, b) 135 °C, c) 152 °C, d) 174 °C.
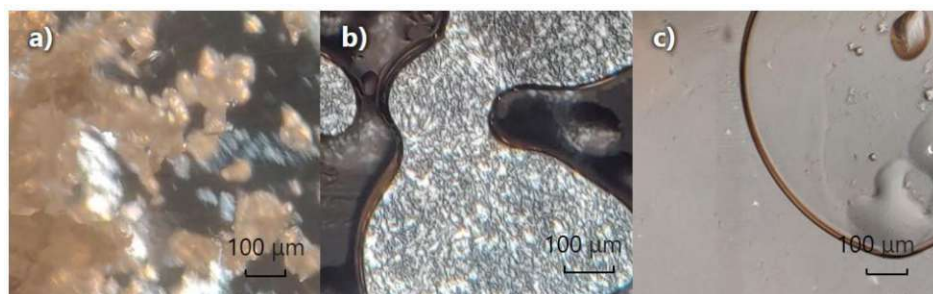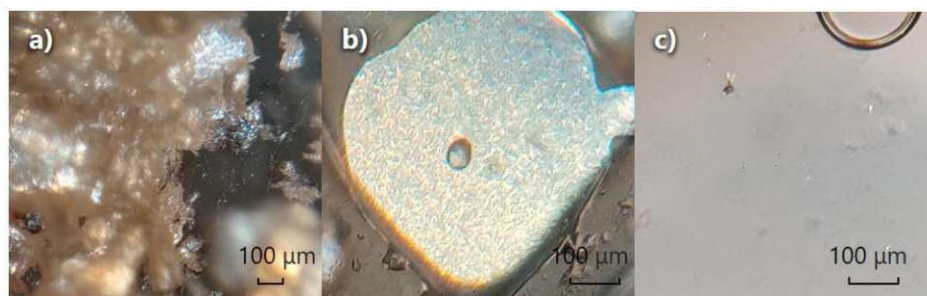
Figure 54: Phases of the 50APF polymer observed on the polarized optical microscope: a) room temperature, b) 115 °C, c) 133 °C.
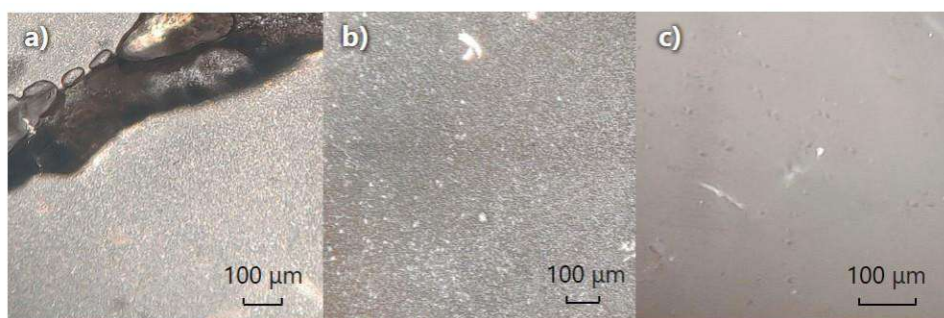
Figure 55: Phases of the 75APF polymer observed on the polarized optical microscope: a) room temperature, b) 80 °C, c) 112 °C.

The semicrystalline HDT-DAT reference polymer (Figure 56) exhibited a crystallite melting point at around 80 °C, after which no further changes were observed when heating the polymer. This crystallite melting point matched with a phase transition temperature observed *via* DSC at 75 °C. According to expectations, only one visible phase transition from opaque to transparent took place. As HDT-DAT is a semicrystalline polymer without mesogenic groups that could cause a long-range order in the molten phase, no optical anisotropy was expected to be observed after the crystallite melting point.
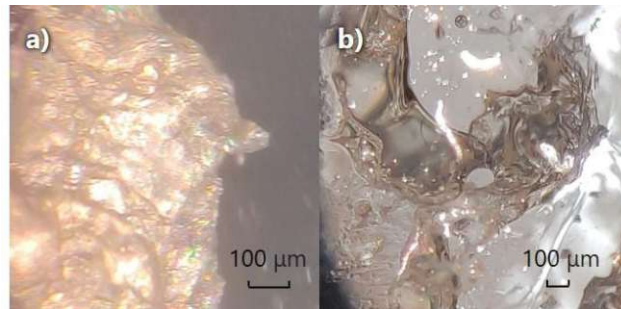
Figure 56: Phases of the HDT-DAT polymer observed on the polarized optical microscope: a) room temperature, b) 80 °C

The phase transition from a liquid crystalline or partially crystalline phase to an isotropic melt were consistently measured higher on the microscope than on the DSC measurement system. This suggests that the visible change in the optical anisotropy happens at the end of the phase transition temperature range.

3.5.2   Atomic force microscopy

Atomic force microscopy (AFM) is a type of scanning probe microscopy capable of recording very high-resolution images. Imaging resolutions on the order of less than a nanometer can be achieved using AFM. A needle mounted on a movable cantilever is moved across a sample surface, which can be performed in a dragging or tapping motion, and the movement is controlled by precise piezo elements. The deflection of the cantilever is recorded by a laser.

Phase Imaging is an AFM technique that can be used to map variations in surface properties such as elasticity, adhesion, and friction. Phase Imaging refers to the monitoring of the phase lag between the signal that drives the cantilever oscillation and its output signal (Figure 57). Changes in the phase lag reflect changes in the mechanical properties of the sample surface.[70]
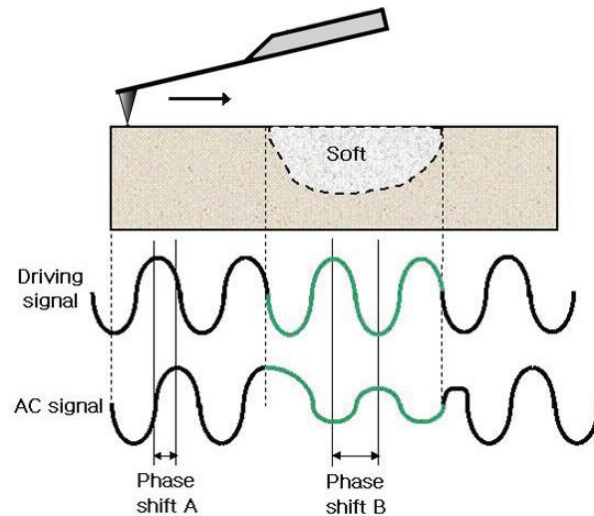
Figure 57: Schematic of AFM phase imaging.[70]

AFM phase images were recorded of all samples that could be adequately prepared for the measurements. The 90DAA, 50APF, and 75APF samples exhibited issues when attempting to record AFM images. A highly heterogeneous surface was observed on the 90DAA sample. Therefore, a representative area for a measurement could not be identified. This could be a result of the softness of the sample due to the high DAA content. The parameters of the sample preparation could be another reason for the surface roughness. The 50APF and 75APF samples exhibited a high adhesion, which affected the cantilever's tracking negatively. Therefore, the phases of 90DAA, 50APF, and 75APF could not be evaluated *via* AFM.

Generally, for the samples measured *via* AFM, some challenges were encountered. Sample preparation proved to be difficult due to the differences in hardness across samples, and even with some optimization, various marks from the grinding and polishing steps were visible on the samples. Further optimization of sample preparation and measurement parameters may be necessary to analyze the phases of the LCEM3-containing polymers to determine the phases and possible phase separation in the samples satisfactorily.

In the AFM images recorded of LCEM3-HDT, no clear evidence of phase separation could be found (Figure 58). Some scratch marks from the sample preparation were visible on all images. While the phase imaging mode did give some clearly separated features, they could not be fully identified as features typical of semicrystalline polymers, such as spherulites or lamellae.
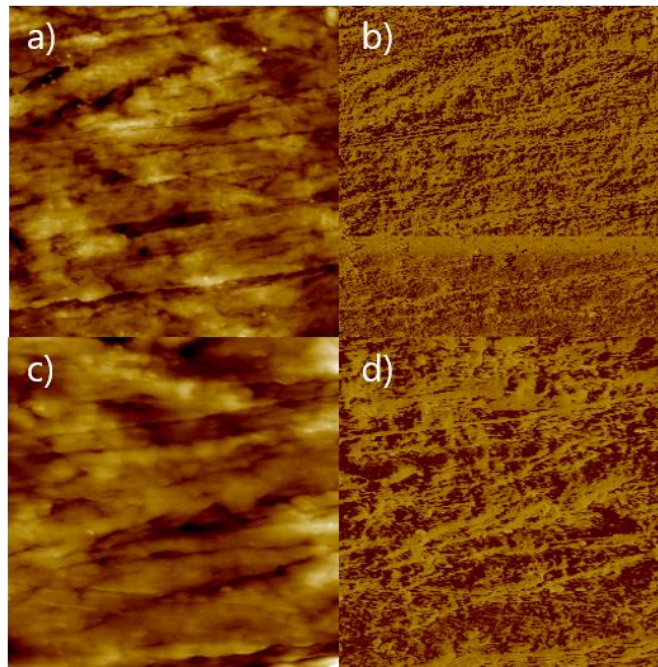
Figure 58: AFM images of LCEM3-HDT polymer: a) 20x20 µm topography, b) 20x20 µm phase imaging,

c) 5x5 µm topography, d) 5x5 µm phase imaging.

The AFM measurements taken of the 50DAA polymer showed some fully white areas in all measured images (Figure 59). The larger white areas were discernible in both the topography and the phase imaging modes. However, the phase imaging mode showed a much larger amount of these bright areas with a high contrast to the remaining image, while almost no other features were visible. Since these features were visible in the phase imaging mode, and not in the topography mode, they could be a sign of phase separation.
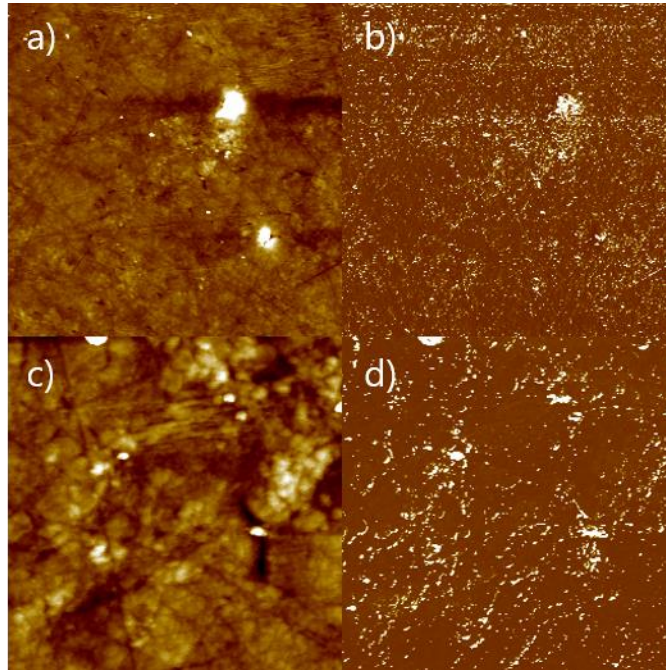
Figure 59: AFM images of 50DAA polymer: a) 20x20 µm topography, b) 20x20 µm phase imaging, c) 5x5 µm topography, d) 5x5 µm phase imaging.

The 75DAA polymer also exhibited white features in the phase images (Figure 60). However, no fully white areas were observed using topography imaging. The white areas also matched the texture that was observed in the topography images. Therefore, it is unlikely that these features are evidence of phase separation. Aside from the fully white features, some branch-like features could be identified in the 20x20 µm phase image (encircled in black) that did not match any features observed in the topography image, and, in some areas, branched out into multiple directions. Therefore, these features can likely be identified as crystal growth patterns typical of a semicrystalline polymer.
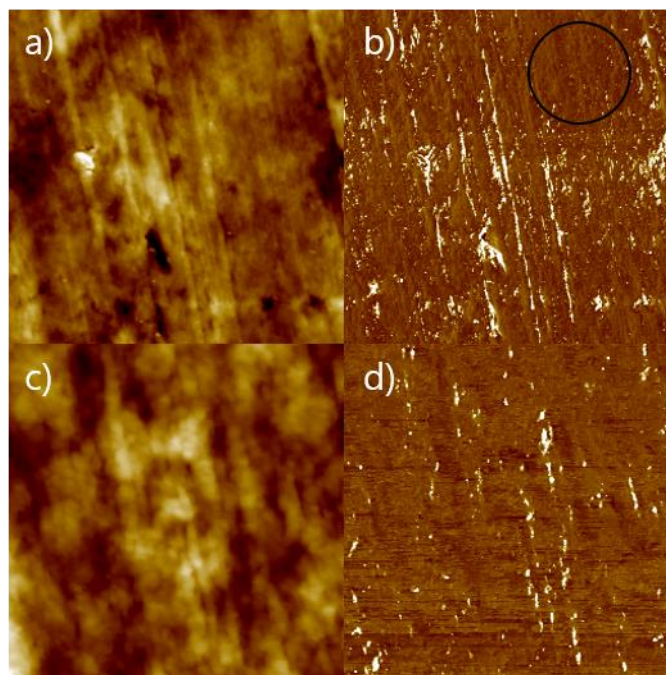
Figure 60: AFM images of 75DAA polymer: a) 20x20 µm topography, b) 20x20 µm phase imaging, c) 5x5 µm topography, d) 5x5 µm phase imaging.

For the 25APF sample (Figure 61), it was not possible to find any features *via* phase imaging that were not already recognizable using topography imaging, except for some horizontal lines in the 20x20 μm image. These can be attributed to the measurement method itself, as they are oriented along the scanning direction throughout the entire image. It is possible that the polymer chains are not long enough to form separated phases in larger areas, or that more optimization of the measurement and sample preparation methods is necessary to detect these phases.
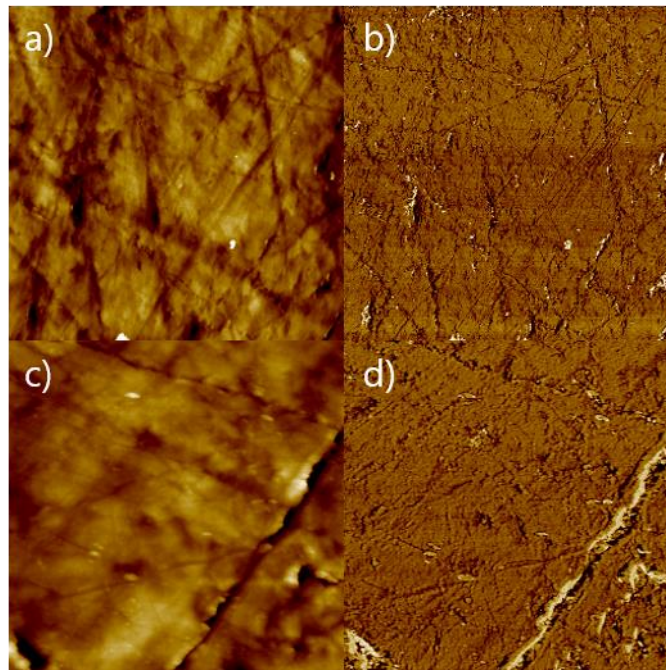
Figure 61: AFM images of 25APF polymer: a) 20x20 μm topography, b) 20x20 μm phase imaging, c) 5x5 μm topography, d) 5x5 μm phase imaging.

Summary

With the goal of creating new recyclable polymers for Hot Lithography 3D printing applications in mind, a library of photopolymerizable difunctional monomers was synthesized. The thiol-ene click reaction was used for polymerization, which is a step-growth mechanism that generates high yields in bulk with 100% atom efficiency. Polymers that are synthesized using this mechanism usually have glass transition temperatures below room temperature, which leads to elastomeric polymers with weak mechanical properties. Therefore, monomers containing liquid crystalline moieties were designed and synthesized.

Monomers that consist of liquid crystalline groups in combination with reactive groups for polymerization typically have melting points that are too high for Hot Lithography applications. Therefore, a molecule with longer spacer chains was synthesized (LCEM3, Figure 62 a), which had a melting point within the applicable range for Hot Lithography printers. A screening experiment was performed, in which a variety of commercially available difunctional thiol monomers were evaluated in combination with LCEM3. The polymerization properties of the thiol monomers were tested in a photoreactivity experiment using photo-DSC and the functional group conversion was determined *via* NMR-spectroscopy. The monomer that showed the best performance in these experiments was 1,6-hexanedithiol (HDT, Figure 62 b).

a)

LCEM3

b)   c)   d)

HDT   DAA   APF   MW ~2000
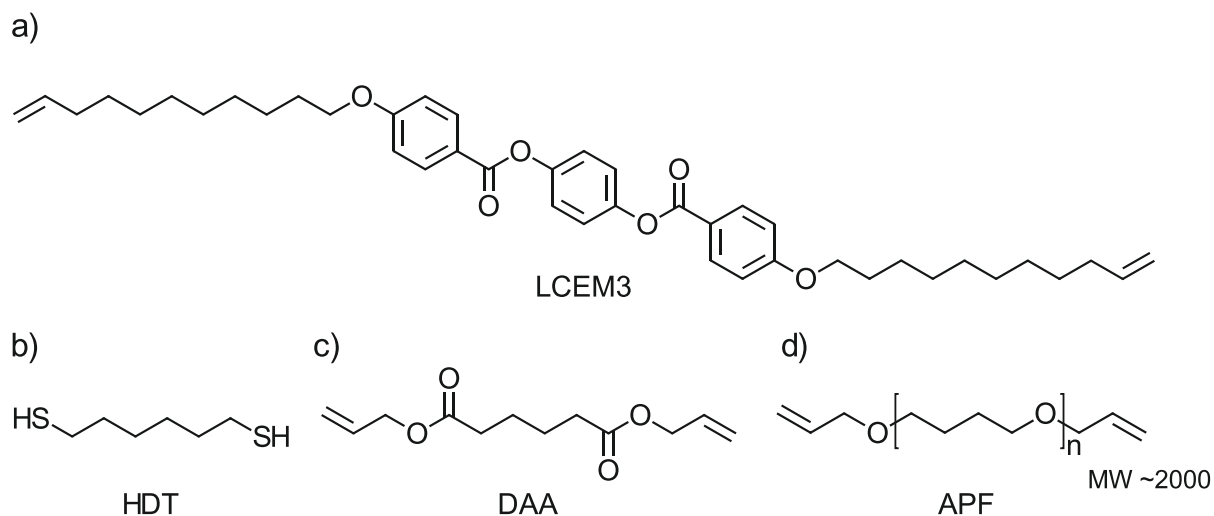
Figure 62: Monomers applied in photopolymerizable formulations: a) LCEM3, b) 1,6-hexanedithiol (HDT), c) diallyl adipate (DAA), d) allyl-functionalized pTHF (APF).

The crystalline polymer, which was formed by combining LCEM3 and HDT in a photopolymerization experiment, exhibited good reactivity and functional group conversion. However, it was also very brittle. To counteract this brittleness, a partial substitution of the highly crystalline LCEM3 monomer with two different softer monomers was performed. For this purpose, diallyl adipate (DAA, Figure 62 c), which was obtained commercially, and allyl-functionalized pTHF (APF, Figure 62 d), which was synthesized, were utilized. Each of these two comonomers was used to substitute LCEM3 in three different concentrations, which amounts to seven formulations that were investigated thoroughly. A literature-known combination of HDT and diallyl terephthalate was used as a reference.

An adequate thermal stability is necessary for Hot Lithography applications so that the formulation does not polymerize spontaneously during a printing project. The viscosity also needs to remain below a certain threshold. Both of these properties were tested in rheology experiments, in which three measurements were performed over the course of five hours. The viscosity was well below the threshold required for a successful 3D printing experiment for all formulations and no significant increase in the viscosity over time was observed, proving a sufficient thermal stability.

Gel permeation chromatography was performed to determine the molecular weight of the polymers. APF-containing polymers generally gave higher molecular weights than DAA-containing polymers. The achieved molecular weights were similar to literature-reported values for thiol-ene polymers (5-6 kDa).

The polymerization properties of the monomer mixtures were investigated using photo-DSC and RT-NIR-photorheology experiments. Using photo-DSC, the speed and intensity of photochemical reactions can be determined. The LCEM3-HDT formulation performed best regarding overall reactivity, along with the reference formulation. The formulations, in which APF was incorporated, followed afterwards, with the DAA-containing formulations exhibiting the lowest reactivities. RT-NIR-photorheology is a measurement method with which the rheological properties of the formulation are observed in real time during photopolymerization. At the same time, NIR-spectroscopy measurements are performed, from which the conversion of reactive groups can be calculated. Photorheology experiments yielded vastly different results for different monomers depending on the melting points of the polymers obtained during the measurements. While polymers with high melting points had a sudden, strong increase in the dynamic modulus with a quick gelation of the formulation, no gel point was obtained for the formulations that resulted in polymers with melting points below the measurement temperature. The amount of crystalline monomer in the formulation had a deciding influence on the melting point of the resulting polymers. Conversions determined by NIR spectroscopy were measured at over 95% for all formulations.

Tensile tests were performed for all polymer materials. A toughening effect was achieved by partially substituting the initially brittle LCEM3-HDT formulation with more elastomeric monomers. The best results, considering a balance of tensile strength and elongation at break, were achieved for the formulations, where 25 mol% of LCEM3 was substituted by APF, and where 75 mol% of LCEM3 was substituted by DAA. Generally, however, the tensile strength of the polymers must be further improved before they can be used in practice as materials for additive manufacturing applications like rapid prototyping.

Phase changes in the polymers were tested *via* DSC, where a multitude of phase transitions was observed in many of the tested polymers, possibly caused by different polymer chain lengths in the materials. They were compared to visible phase changes observed on the polarized optical microscope, which is an instrument often utilized to analyze phase change behavior in (liquid) crystalline materials. Liquid crystalline phases were encountered in some of the molten polymers, which had a high content of the mesogenic LCEM3 monomer. Therefore, it was, to a certain degree, possible to control the liquid crystallinity in the polymer samples. This could be relevant for future research, especially regarding the tuning of optical properties of liquid crystalline materials similar to the systems used in this work. A satisfactory correlation of DSC phase transitions with phase transitions measured *via* polarized optical microscopy was observed in most cases. Phase imaging via atomic force microscopy (AFM) showed some evidence of phase separation. Some features in the images were identified as typical semicrystalline structures. However, further studies and optimization would be necessary before AFM can be used reliably to identify phases and other structures in the polymers.

In conclusion, this work has contributed to gaining fundamental understanding of using liquid crystalline photopolymerizable monomers in bulk applications. The insights obtained from this work will contribute largely to the next generation of liquid crystalline photopolymerizable monomers.

Experimental part

1 Synthesis and characterization of monomers

1.1 Liquid crystalline terminal alkene monomers

1.1.1 LCEM1

1.1.1.1   Synthesis of precursor *p*-allyloxybenzoic acid

The synthesis of *p*-allyloxybenzoic acid was performed in accordance with a procedure outlined by Shen *et al.*[61]
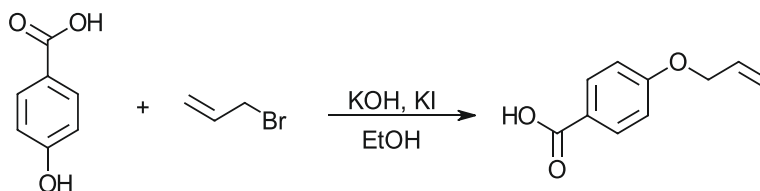
Scheme 14: Synthesis of p-allyloxybenzoic acid.

Potassium hydroxide (2.3 eq, 0.28 mol, 15.71 g) and potassium iodide (0.033 eq, 4 mmol) were added to a solution of *p*-hydroxybenzoic acid (1 eq, 0.12 mol, 16.57 g) in 300 mL ethanol. After the reaction mixture had been stirred at room temperature for 1 h, allyl bromide (1.33 eq, 0.16 mol, 19.36 g) was added dropwise to the mixture. The resulting mixture was heated under reflux overnight. After cooling to room temperature, 1 mol L^{-1} HCl solution was added to neutralize the reaction mixture. The white precipitate was filtered and washed with ethanol. The solvent was removed under reduced pressure, yielding 13.79 g of white powder (65% th.).

^{1}H NMR (400 MHz, DMSO): δ = 12.62 (s, 1H), 7.86 (d, 2H), 7.02 (d, 2H), 6.03 (m, 1H), 5.36 (m, 2H), 4.63 (m, 2H).

^{13}C NMR (101 MHz, DMSO): δ = 166.98, 161.77, 133.21, 131.33, 123.08, 117.85, 114.47, 68.38, 40.15, 39.94, 39.73, 39.52, 39.31, 39.10, 38.89.

R$_f$-value: 0.72 (DCM)

Melting point (°C): 166-168 (Lit. 162-164[71])

1.1.1.2   Synthesis of LCEM1

The synthesis of LCEM1 was performed according to a procedure outlined by Zhang *et al.*[62]
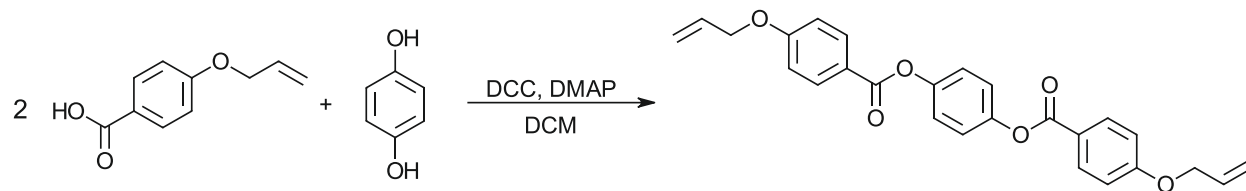
Scheme 15: Synthesis of LCEM1.

For the second step, *p*-allyloxybenzoic acid (2.2 eq, 77.4 mmol, 13.49 g), hydroquinone (1 eq, 35.18 mmol, 3.87 g), and dimethylaminopyridine (0.4 eq, 14.1 mmol, 1.72 g) were stirred in 200 mL anhydrous dichloromethane in an argon-flushed flask. After cooling the mixture below -10 °C using an NaCl/ice bath, *N,N*'-dicyclohexylcarbodiimide, (DCC, 2.2 eq, 77.4 mmol, 14.84 g) suspended in 200 mL of dichloromethane was added dropwise to the reaction mixture while keeping the temperature below -5 °C. The mixture was slowly allowed to warm up to room temperature and continued to be stirred for 48 h. The mixture was filtrated, and the filtrate was extracted five times with water and dried over sodium sulphate. After detecting impurities in the form of dicyclohexylurea, the product was again dissolved in dichloromethane and filtrated, then crystallized from the solution after concentrating the solution further by removing part of the solvent. The product was washed with cold dichloromethane. 10.08 g of the product were obtained as a white powder (67% th.).

^{1}H-NMR (400 MHz, CDCl$_3$): δ = 8.22 − 8.10 (m, 4H), 7.22 (dd, J = 8.7, 1.4 Hz, 4H), 7.07 − 6.94 (m, 4H), 6.08 (ddt, J = 17.3, 10.5, 5.3 Hz, 2H), 5.52 − 5.27 (m, 4H), 4.64 (dt, J = 5.3, 1.5 Hz, 4H).

¹³C NMR (101 MHz, CDCl₃): δ = 164.77, 162.96, 148.42, 132.46, 132.33, 122.66, 121.83, 118.28, 114.59, 68.96, 33.97, 24.97.

R$_f$-value: 0.75 (DCM:MeOH 100:1)

Phase transition temperatures (°C): Cr 167 Sm 190 N 230 I

1.1.2   LCEM2

1.1.2.1   Synthesis of precursor *p*-allyloxybenzoic acid

The synthesis of *p*-allyloxybenzoic acid was performed in accordance with a procedure outlined by Shen *et al.*[61] as described in chapter 1.1.1.
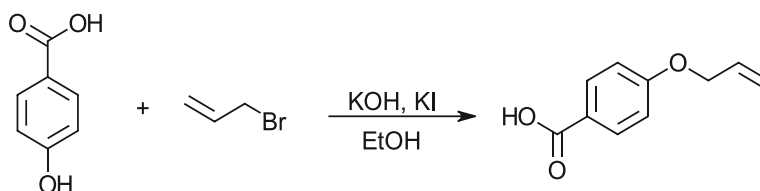
Scheme 16: Synthesis of p-allyloxybenzoic acid.

Potassium hydroxide (2.3 eq, 0.28 mol, 15.71 g) and potassium iodide (0.033 eq, 4 mmol) were added to a solution of *p*-hydroxybenzoic acid (1 eq, 0.12 mol, 16.57 g) in 300 mL ethanol. After the reaction mixture had been stirred at room temperature for 1 h, allyl bromide (1.33 eq, 0.16 mol, 19.36 g) was added dropwise to the mixture. The resulting mixture was heated under reflux overnight. After cooling to room temperature, 1 mol L^{-1} HCl solution was added to neutralize the reaction mixture. The white precipitate was filtered and washed with ethanol. The solvent was removed under reduced pressure, yielding 13.79 g of white powder (65% th.).

**¹H NMR (400 MHz, DMSO):** δ = 12.62 (s, 1H), 7.86 (d, 2H), 7.02 (d, 2H), 6.03 (m, 1H), 5.36 (m, 2H), 4.63 (m, 2H).

¹³C NMR (101 MHz, DMSO): δ = 166.98, 161.77, 133.21, 131.33, 123.08, 117.85, 114.47, 68.38, 40.15, 39.94, 39.73, 39.52, 39.31, 39.10, 38.89.

R$_f$-value: 0.72 (DCM)

Melting point (°C): 166-168 (Lit. 162-164[71])

1.1.2.2   Synthesis of LCEM2

The synthesis of LCEM2 was performed using a Steglich esterification according to a procedure outlined by Zhang *et al.* with the use of methylhydroquinone instead of hydroquinone.[62]
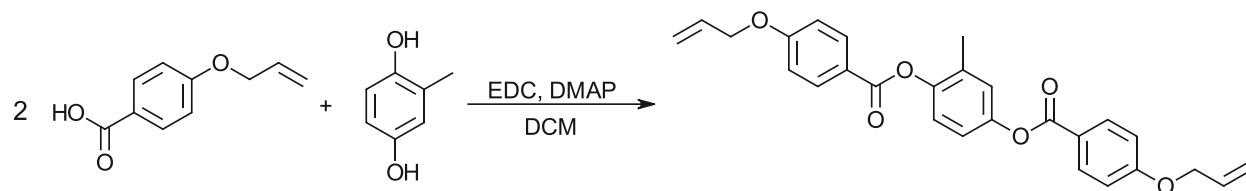
Scheme 17: Synthesis of LCEM2. P-allyloxybenzoic acid was combined with methylhydroquinone in a Steglich esterification. 1-Ethyl-3-(3-dimethylaminopropyl) carbodiimide hydrochloride was used as a coupling agent, as the resulting byproduct is easy to separate by extraction or crystallization. Dimethylaminopyridine (DMAP) was employed as a catalyst, and dichloromethane (DCM) was used as a solvent.

P-allyloxybenzoic acid (2.2 eq, 50.3 mmol, 8.97 g), methylhydroquinone (1 eq, 22.88 mmol, 2.84 g), and dimethylaminopyridine (DMAP, 0.4 eq, 9.17 mmol, 1.12 g) were stirred in 200 mL anhydrous dichloromethane in an argon-flushed flask. After cooling the mixture below -10 °C using an NaCl/ice bath, EDC (2.2 eq, 50.3 mmol, 9.65 g) dissolved in 150 mL of dichloromethane was added dropwise to the reaction mixture while keeping the temperature below -5 °C. The mixture was slowly allowed to warm up to room temperature and continued to be stirred for 48 h. The mixture was filtrated, and the filtrate was extracted five times with water and dried over sodium sulphate. The solvent was removed, and the product was recrystallized from ethyl acetate to yield 4.87 g (48% th.) white powder.

¹H NMR (400 MHz, CDCl₃): δ = 8.21 – 8.11 (m, 4H), 7.22 – 7.05 (m, 3H), 7.05 – 6.95 (m, 4H), 6.08 (ddtd, J = 16.7, 10.5, 5.3, 0.8 Hz, 2H), 5.51 – 5.28 (m, 3H), 4.64 (dq, J = 5.3, 1.7 Hz, 4H), 2.25 (s, 3H).

¹³C NMR (101 MHz, CDCl₃): δ = 165.00, 164.61, 163.09, 148.55, 147.17, 132.59, 132.43, 131.92, 124.26, 123.04, 122.06, 121.90, 120.18, 118.40, 114.70, 69.08, 16.22.

Rf-value: 0.25 (PE:EE 4:1)

Phase transition temperatures (°C): Cr 142 LC 217 I

1.1.3   LCEM3

1.1.3.1   Synthesis of precursor *p*-(undecenyloxy)benzoic acid

The precursor *p*-(undecenyloxy)benzoic acid was synthesized according to a procedure by Alvarez and Mehl.[72]
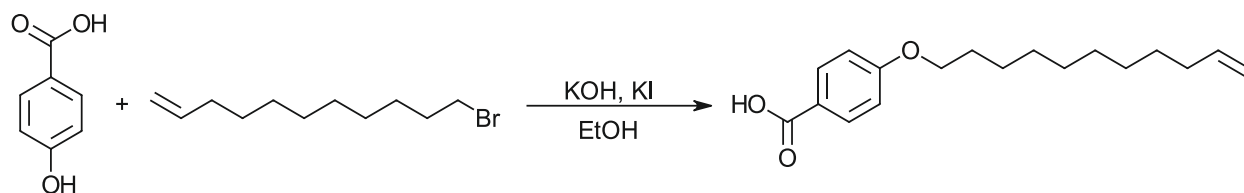
Scheme 18: Synthesis of p-(10-undecenyl-1-oxy)benzoic acid.

Potassium hydroxide (2.3 eq, 0.172 mol, 9.65 g) and potassium iodide (0.033 eq, 0.005 mol, 0.83 g) were added to a solution of *p*-hydroxybenzoic acid (1 eq, 0.074 mol, 10.22 g) in 250 mL of ethanol. After the reaction mixture had been stirred at room temperature for 1 h, 11-bromo-1-undecene (1.12 eq, 0.083 mol, 19.3 g) was added dropwise to the mixture. The resulting mixture was refluxed at 80 °C overnight. After cooling to room temperature, 30 mL water were added to split the ester that had formed as a byproduct. The mixture was briefly heated to reflux and cooled again. 1 mol L⁻¹ HCl solution was then added to acidify the reaction mixture to pH 3-4. The white precipitate was filtered and washed twice with water, twice with ethanol, and three times with diethyl ether. 14.58 g of the product were obtained (67.8% th.).

¹H NMR (400 MHz, DMSO) δ = 12.61 (s, 1H) 8.04 – 7.74 (m, 2H), 7.13 – 6.91 (m, 2H), 5.79 (ddt, J = 16.9, 10.2, 6.7 Hz, 1H), 5.09 – 4.84 (m, 2H), 4.03 (t, J = 6.5 Hz, 2H), 2.01 (tdd, J = 8.0, 6.0, 1.4 Hz, 2H), 1.83 – 1.60 (m, 2H), 1.49 – 1.09 (m, 12H).

¹³C NMR (101 MHz, DMSO) δ = 167.53, 162.71, 139.31, 131.44, 123.44, 115.11, 114.65, 68.22, 40.63, 40.42, 40.21, 40.00, 39.79, 39.58, 39.37, 33.64, 29.40, 29.25, 29.17, 28.98, 28.96, 28.73, 25.89.

R$_f$-value: 0.87 (DCM)

Melting point (°C): 82-85 (Lit. 79.5-80[73])

1.1.3.2   Synthesis of LCEM3

The synthesis of LCEM3 was performed according to a procedure outlined by Zhang et al.[62] Deviations from the original procedure were the use of EDC instead of DCC and the use of *p*-(undecenyloxy)benzoic acid instead of *p*-(allyloxy)benzoic acid.
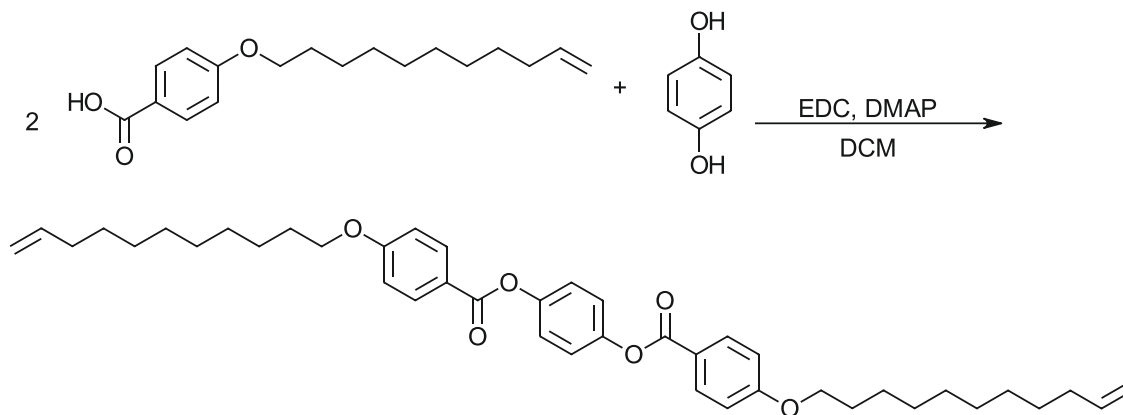
Scheme 19: Synthesis of LCEM3.

For the second step, *p*-(10-undecenyloxy)benzoic acid (2.1 eq, 68.8 mmol, 20 g), hydroquinone (1 eq, 32.2 mmol, 3.61 g), and dimethylaminopyridine (0.4 eq, 1.31 mmol, 1.60 g) were stirred in 350 mL of anhydrous dichloromethane in an argon-flushed flask. After cooling the mixture below -10 °C using an NaCl/ice bath, EDC (2.1 eq, 68.8 mmol, 13.20 g) dissolved in 250 mL of dichloromethane was added dropwise into the reaction mixture while keeping the temperature below -5 °C. The mixture was slowly allowed to

warm up to room temperature and continued to be stirred for 48 h. The mixture was filtrated, and the filtrate was extracted with water and dried over sodium sulphate. The solvent was removed and the product was purified by medium pressure liquid chromatography using dichloromethane.

HPLC (high performance liquid chromatography) analysis was performed to analyze the purity of the product. The samples were separated by non-aqueous reverse phase chromatography in a C18 column. The eluent gradient was set from MeOH/CHCl$_3$ 90:10 to MeOH/CHCl$_3$ 10:90 over the measurement time. Detection was performed by UV absorption at a wavelength of 250 nm.

As some impurities were found by HPLC analysis, the product was purified by recrystallization from 250 mL of PE/EE 2:1. During the cooling process, the product quickly crystallized from the solution, forming a fine white precipitate. After filtration and drying the filter cake at reduced pressure, 15.08 g of the pure product were obtained as a white powder (70% th.).

^{1}H NMR (400 MHz, CDCl$_3$): δ = 8.22 – 8.04 (m, 4H), 7.26 (d, J = 1.2 Hz, 4H), 7.06 – 6.90 (m, 4H), 5.82 (ddt, J = 16.9, 10.2, 6.7 Hz, 2H), 5.06 – 4.88 (m, 4H), 4.05 (t, J = 6.6 Hz, 4H), 2.14 – 1.97 (m, 4H), 1.91 – 1zz.74 (m, 4H), 1.60 – 1.09 (m, 28H).

^{13}C NMR (101 MHz, CDCl$_3$): δ = 165.01, 163.74, 148.56, 139.35, 132.45, 122.80, 121.55, 114.47, 114.29, 68.48, 33.94, 29.63, 29.55, 29.48, 29.25, 29.24, 29.07, 26.12.

R$_f$-value (TLC): 0.77 (DCM)

t(R) (HPLC): 481 s at a gradient of MeOH/CHCl$_3$ 90:10 to MeOH/CHCl$_3$ 10:90 over 20 min

Phase transition temperatures (°C): Cr 111 SmC 140 N 177 I

HR-MS: (DCM/MeOH, ESI+, m/z): calculated: 655.8796 [M+H]$^+$; found: 655.8796 [M+H]$^+$

1.2   Liquid crystalline dithiol monomer

The synthesis of LCDT was performed from the LCEM1 monomer *via* application of the thiol-ene click reaction.
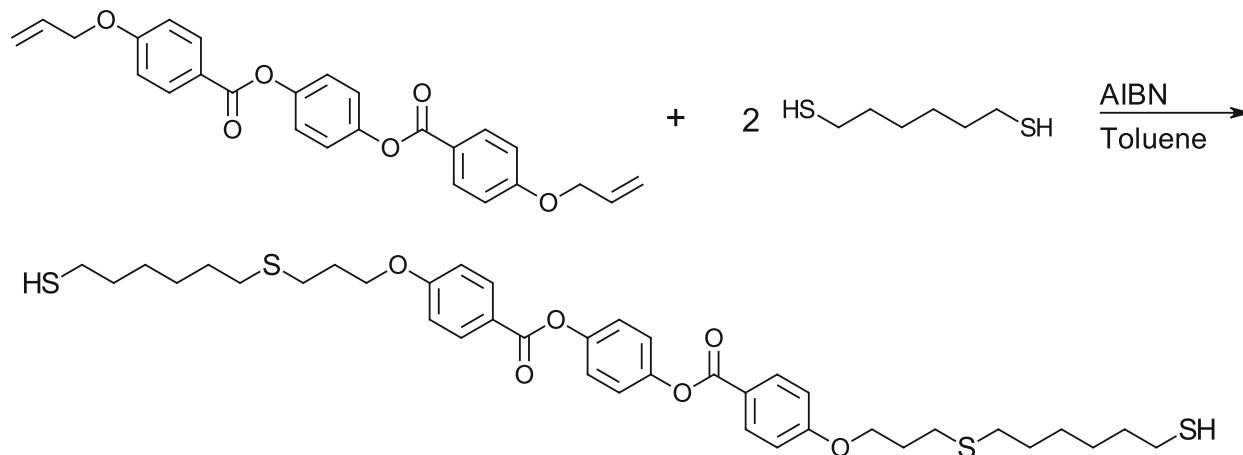
Scheme 20: Synthesis of LCDT.

LCEM1 (1 eq, 9.29 mmol, 4 g) and 1,6-hexanedithiol (8 eq, 74.3 mmol, 11.17 g) were dissolved in 250 mL of dry toluene. The mixture was slowly heated to 65 °C and azobisisobutyronitrile (AIBN, 7 wt% of LCEM1, 1.71 mmol, 0.28 g) was added in three portions over the course of heating up. Afterwards, the mixture was stirred at 65 °C for two hours. The mixture was cooled and filtrated through a glass sinter funnel. The solvent was evaporated from the filtrate and the crude product was purified by column chromatography (DCM/MeOH 100:1).

4.10 g of the product (60% th.) were obtained as a white powder after drying under vacuum.

^{1}H NMR (400 MHz, CDCl$_3$): δ = 8.19 − 8.11 (m, 4H), 7.26 (d, J = 1.0 Hz, 4H), 7.03 − 6.95 (m, 4H), 4.17 (t, J = 6.1 Hz, 4H), 2.73 (t, J = 7.1 Hz, 4H), 2.53 (qd, J = 7.4, 3.1 Hz, 8H), 2.16 − 2.05 (m, 4H), 1.68 − 1.55 (m, 8H), 1.41 (tdd, J = 7.3, 4.4, 2.2 Hz, 8H), 1.33 (t, J = 7.8 Hz, 2H).

^{13}C NMR (101 MHz, CDCl$_3$): δ = 164.93, 163.42, 148.54, 132.47, 122.79, 121.83, 114.47, 66.66, 33.96, 32.31, 29.58, 29.24, 28.62, 28.41, 28.05, 24.68.

R$_f$-value (TLC): 0.6 (DCM/MeOH 100:1),

t(R) (HPLC): 160 s at a gradient of MeOH/CHCl$_3$ 90:10 to MeOH/CHCl$_3$ 10:90 over 19 min

Phase transition temperatures (°C): Cr 80 LC 133 I

HR-MS: (DCM/MeOH, ESI+, m/z): calculated: 731.0699 [M+H]$^+$; found: 731.0699 [M+H]$^+$

1.3   Allyl-functionalized pTHF

Allyl-functionalized pTHF (APF) was synthesized according to a procedure outlined by Jang et al.[64] All parameters were kept the same, except for the use of a larger amount of solvent (120 mL DMF instead of 40 mL in the main flask).
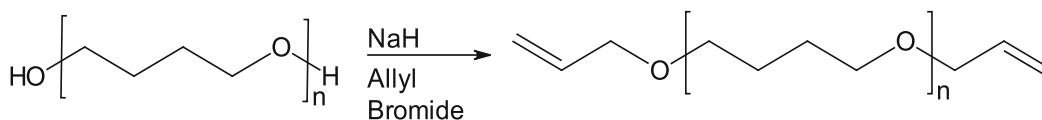
Scheme 21: Synthesis of allyl-functionalized pTHF.[64]

NaH (60% suspension in mineral oil, 333 mmol, 8.00 g) was suspended in anhydrous dimethyl formamide (DMF, 120 mL) and stirred at 0 °C under argon atmosphere. A solution of pTHF, (20.0 g, 10.0 mmol) in DMF (40 mL) was added dropwise to the mixture and the mixture was stirred for 30 min at 0 °C, which caused a rigid foam to form. Allyl bromide (198 mmol, 24.0 g) was added dropwise to the mixture. The mixture was warmed to room temperature and stirred for 12 h. The reaction was stopped by slowly adding 100 mL of water at 0 °C to hydrolyze the remaining NaH. The solution was diluted with 200 mL CHCl$_3$ and washed twice with 200 mL water and brine. The organic layer was dried over MgSO$_4$, filtrated, and concentrated *in vacuo*. The resulting yellow oil was purified by column chromatography (dichloromethane/methanol 10:1), which yielded 19.51 g (96% th.) of a slightly yellow oil that solidified into a waxy solid over a period of around three days.

^{1}H-NMR: (400 MHz, CDCl$_3$): δ = 5.91 (ddt, J = 17.3, 10.5, 5.6 Hz, 2H), 5.29 (q, J = 1.7 Hz, 4H), 3.96 (dt, J = 5.6, 1.4 Hz, 4H), 3.41 (tq, J = 4.1, 3.0 Hz, 116H), 1.73 – 1.49 (m, 143H).

R$_f$-value: 0.7 (DCM/MeOH 10:1)

Melting point (°C): 29 (Lit. 34[64])

Conversion of the hydroxyl groups into allyl groups was determined *via* ^{31}P-NMR-spectroscopy using the reagent 2 chloro-4,4,5,5-tetramethyl-1,3,2-dioxaphospholane (TMDP).[65] 30 mg pTHF and allyl-terminated pTHF were each dissolved in 300 µL chloroform and 100 µL pyridine. 100 µL of a solution of 40.58 mg mL^{-1} of the internal standard cyclohexane and 5.001 mg mL^{-1} of the relaxation reagent chromium(III) acetylacetonate in pyridine was added. The mixture was shaken and a second mixture of 100 µL TMDP and 200 µL chloroform was added to each of the samples. After preparation, a ^{31}P-NMR-spectrum (inverse gated mode, 128 scans, 25 s relaxation time) was recorded on a Bruker 600 MHz NMR-spectrometer.

The OH-number was calculated using (4). c$_{standard}$ is the concentration of the cyclohexanol standard in mg mL^{-1}. V$_{standard}$ is the volume of the cyclohexanol standard added to the sample in µL. I$_{func.gr}$ is the integral of the corresponding functional group in the defined integration area. M$_{standard}$ is the molar mass of the cyclohexanol standard (100.158 g mol^{-1}). I$_{standard}$ is the integral of the cyclohexanol standard peak (set to 1). m$_{sample}$ is the mass of the sample used in the measurement in g.

$$OH\ value\left(\frac{mmol}{g}\right) = \frac{c_{standard}\cdot V_{standard}\cdot I_{func.gr}}{M_{standard}\cdot I_{standard}\cdot m_{sample}} \tag{4}$$

2   Thiol monomer screening

For all formulations, the thermal inhibitor was weighed into a brown glass vial first, followed by the photoinitiator, then the thiol monomer, and finally, the ene-monomer was added. This ensured that the thermal inhibitor could dissolve in the thiol monomer at room temperature or with mild heating before reaching the high temperature necessary for homogenization of the thiol and ene-monomers.

2.1   Reactivity *via* photo-DSC

10-15 mg of the formulation were accurately weighed into an aluminium DSC crucible and covered with a glass cover slide.

A light source with a wavelength range of 300-500 nm was used, with a light intensity of 35 mW cm^{-2} reaching the sample. Irradiation of the sample was started after 60 s and the sample was irradiated for 360 s. A second analogous irradiation period was performed, and the measurements were subtracted from each other to achieve a baseline correction.

The peak area in J mol^{-1} was calculated per double bond. Therefore, the number of double bonds in the sample in mol g^{-1} was calculated first. The peak area in J g^{-1} was then divided by this factor. To calculate the t_{95}, the DSC peak area was integrated and the time when 95% of the area had been covered was measured.

2.2   Molecular weight *via* gel permeation chromatography

Polymer samples from measured photo-DSC crucibles were used to measure GPC. The samples were dissolved in THF spiked with a butylhydroxytoluene flow rate marker. To dissolve the samples, they were stirred at a temperature of around 50 °C. The dissolved polymers were then transferred into GPC vials through a syringe filter. Data evaluation was performed using OmniSEC 5.12, where the baseline was manually set before selecting the peaks.

2.3   Conversion *via* NMR-spectroscopy

All samples from DSC crucibles were dissolved in deuterated chloroform and mildly heated and shaken until the polymer was dissolved. The peak areas of the aromatic region were used as a standard for integration.

Terminal alkene peak 1: ^{1}H-NMR (400 MHz, $CDCl_3$): δ = 4.99 (m, 4 H)

Terminal alkene peak 2: ^{1}H-NMR (400 MHz, $CDCl_3$): δ = 5.85 (ddt, 2 H)

Aromatic reference peak: ^{1}H-NMR (400 MHz, $CDCl_3$): δ = 8.23 – 8.10 (m, 4H)

3 Polymer curing and characterization

For all measurements, formulations were prepared in brown glass vials. The thermal inhibitor was weighed in first, then the photoinitiator, followed by the thiol. The vial was shaken to ensure that the thermal inhibitor could dissolve in the thiol monomer. Finally, the ene-monomers were added.

3.1 Viscosity and thermal stability of formulations

Viscosity of the formulations was tested at a rheometer with a heated sample plate at 120 °C. A conical plate stamp with a diameter of 25 mm and a cone angle of 0.979° was used with a gap size of 0.048 mm. Before the measurements, the rheology stamp was heated on the sample plate until the normal force remained at a constant level. Measurements were performed by transferring the formulation onto the heated rheometer plate, and after a 50 s period, increasing the rotation speed from 0 to 100 rad s^{-1} over another 50 s. Afterwards, viscosity was measured for 100 s at a rotation speed of 100 rad s^{-1} in measurement intervals of 10 s. The average viscosity values in the final 100 s measurement period were used for data evaluation.

3.2 Photoreactivity analysis

3.2.1 Photo-DSC

Photo-DSC measurements were performed with the measurement parameters described in chapter 2.1.

3.2.2 RT-NIR-photorheology

The measurement platform was heated up to 120 °C and a waiting time of three minutes was chosen before transferring the formulation onto the measurement surface to ensure sufficient heating of the full sample surface and the rheology stamp. A parallel plate rheology stamp with a diameter of 25 mm was used with a gap size of 0.2 mm. Around

140 mg of the crystalline formulations were transferred onto the sample surface with a spatula, where they were melted and measured at an irradiation time of 300 s and a light intensity of 35 mW cm^{-2}. No polyethylene tape was used on the sample surface, as the high temperature caused the tape to become too soft to measure the samples. NIR data was evaluated by first performing a baseline correction on the data set (concave rubber band method, 10 iterations), then integrating the curve from 6064 to 6186 cm^{-1}.

3.3 Molecular weight *via* gel permeation chromatography

Bulk polymer samples from tensile tests were used to measure GPC. The samples were dissolved in THF spiked with a butylhydroxytoluene flow rate marker. To dissolve the samples, they were stirred at a temperature of around 50 °C. The dissolved polymers were then transferred into GPC vials through a syringe filter. The samples were not measured if there was a large resistance when filtrating through the syringe filter, as it is an indication that the polymers are not fully dissolved, which can damage the GPC column. Triple detection was performed by injecting the sample five times with five different injection volumes from 80 to 120 µl to allow calculation of the dn/dc value. Data evaluation was performed using OmniSEC 5.12, where the baseline was manually set before selecting the peaks.

As most polymers were not soluble in THF, the polymers were dissolved in chloroform and a GPC measurement was performed on a different column in a HPLC instrument. With no flow rate marker or calibration available for this measurement system, the frame of reference was based on the polymers evaluated *via* GPC thus far. The time for the refractive index to reach the maximum after injection of the sample was used.

Table 12: Results of the GPC samples measured in chloroform.

Formulation	Time at max refractive index (min)
LCEM3-HDT	6.06
25APF	6.20
50APF	6.16
75APF	6.07
50DAA	6.36
90DAA	6.27

3.4   Thermomechanical properties

3.4.1   Tensile testing

Preparation of tensile test samples was performed by casting the molten formulation into dog bone shape silicone molds accordance with ISO 527 test specimen 5b. The molds were heated to ~120 °C. Six samples of each formulation were then cured in a Uvitron UV floodlight at 100% intensity for 300 s. After cooling to room temperature, the samples were removed from the mold and cured on the other side.

The samples were fixed between two clamps on the tensile testing instrument and strained with a traverse speed of 5 mm min^{-1}, during which a stress-strain plot was recorded.

Table 13: Results of tensile test samples of LCEM3-HDT polymers with varying degrees of substituted ene-monomers.

Formulation	Ultimate tensile strength (MPa)	Elongation at break (%)
LCEM3-HDT	3.65±1.41	0.90±0.23
50DAA	1.02±0.29	0.73±0.14
75DAA	1.85±0.76	4.15±0.96
90DAA	0.68±0.30	2.94±0.30
25APF	2.27±0.37	9.22±1.69
50APF	1.19±0.15	11.20±3.72
75APF	0.17±0.08	10.06±5.74
HDT-DAT ref.	10.21±0.73	343.27±145.43

For the tempering experiment, a fresh series of tensile test specimens were prepared, as a new batch of allyl-terminated pTHF had been used. The samples were left in a drying oven at 80 °C for five hours. To ensure a slow cooling process, the samples were subsequently moved to a series of drying ovens at 60 °C, 50 °C, and 37.5 °C, respectively.

3.4.2   Thermal analysis

To perform the differential scanning calorimetry measurements, polymer samples from previously measured tensile tests were transferred into a DSC crucible and cooled to -90 °C. The measurement was started, and the samples were heated to 200 °C at a rate of 10 °C min^{-1}, cooled once more to -90 °C, and heated back to 200 °C. During this time, the heat flow differential between the sample chamber and the reference chamber was recorded. The second heating cycle was used for evaluation of the phase transitions.

3.5   Phase analysis

3.5.1   Polarized optical microscopy

For analysis on the polarized optical microscope, a small amount of the sample was transferred onto a glass slide and flattened with a spatula. A cover slide was put on top

of the sample. Pictures were taken through a camera inlet on top of the objective. An etched glass scale bar was used to measure the scale of the images.

3.5.2   Atomic force microscopy

To prepare the polymer samples for AFM analysis, the polymer samples were embedded in a Struers EpoFix transparent cold curing epoxy resin in the shape of 3 cm diameter cylinders. They were subjected to a grinding and polishing program (Table 14). A force of 10 N per sample was used for polishing with a turning plate speed of 150 rpm. Between steps, the samples were washed with water and sonicated for 5 min each time. The loose grain polishing steps using diamond paste were introduced after the 4000 grit sandpaper-grinding step did not yield a satisfactory sample surface.

Table 14: Grinding and polishing steps used to prepare the resin-embedded polymer samples for AFM measurements.

Time	Grinding/polishing medium	Lubricant
90 s	800 grit sandpaper	Water
5 min	1200 grit sandpaper	Water
20 min	4000 grit sandpaper	Water
10 min	15 μm diamond paste	Struers DP-lubricant blue
10 min	9 μm diamond paste	Struers DP-lubricant blue
10 min	6 μm diamond paste	Struers DP-lubricant blue
15 min	1 μm diamond paste	Struers DP-lubricant blue

AFM phase imaging measurements were performed alongside topography imaging. A representative surface with no scratch marks was located and on this surface, a 20x20 μm and 5x5 μm surface was imaged on each sample. Images were recorded in tapping mode with a scan rate of 0.7 Hz.

Materials and methods

Chemicals and monomers:

Table 15: Chemicals and monomers used in this work, which were obtained commercially.

Chemical	Purity (%)	Manufacturer
Allyl bromide	>98%	TCI chemicals
Hydroquinone	>99%	Merck
Undecenyl bromide	99.74%	BCDPharm
PTHF (MW ~2000)	– [1]	Sigma Aldrich
Diallyl terephthalate (DAT)	>98%	TCI chemicals
Sodium hydride	60% dispersion in paraffin liquid	TCI chemicals
1,4-hydroxybenzoic acid	for synthesis	Merck
1,6-hexanedithiol (HDT)	>97%	TCI chemicals
2,2'-(Ethylenedioxy)diethanethiol (EDDT)	>95%	Sigma Aldrich
4,4'-thiobisbenzenethiol (TBBT)	>98%	Sigma Aldrich
Ethylene bis(thioglycolate (EBTG)	>97%	TCI chemicals
Dithiothreitol (DTT)	>98%	TCI chemicals
Bis(2-mercaptoethyl)ether (BMEE)	>95%	TCI chemicals
Pyrogallol	>98%	Merck
Ivocerin	– [1]	Ivoclar Vivadent
M4470 silicone	– [1]	Farben Wolf
T37 silicone crosslinker	– [1]	Farben Wolf
EpoFix kit	– [1]	Struers

[1] no purity given by manufacturer

Polarized optical microscopy was performed on a Zeiss Axio Scope.A1 equipped with a Linkam T95-HS heated sample stage.

Column Chromatography: A Büchi Sepacore flash system (Büchi pump module C-605, Büchi control unit C-620, Büchi UV-Photometer C-635, Büchi fraction collector C-660) was used. Separation was performed in glass columns packed with silica gel 60 (Merck, 0.040-0.063 mm).

DSC Measurements were performed on a TA Instruments DSC Q2000 V24.11 Build 124. The samples were weighed into aluminium DSC crucibles covered with a pierced aluminium lid.

GPC was performed using a waters GPC using 3 columns (Styragel HR 0.5, Styragel HR 3 and Styragel HR 4) and a Waters 2410 RI detector, a UV Detector Module 2550 for TDA 305 and a VISCOTEK SEC-MALS 9 light scattering detector. A polystyrene standard (375 – 177000 Da) was used for conventional calibration to determine the molecular weight of the polymers. Data evaluation was performed using OmniSEC 5.12.

GPC on HPLC instrument with chloroform as a solvent was performed on an Agilent 1100 Series HPLC instrument using a Waters Styragel HR 3 column.

HPLC was performed on an on an Agilent 1100 Series HPLC instrument using a non-aqueous reverse phase C18 column.

NMR-spectroscopy was performed on a Bruker DPX-200/400 FT-NMR spectrometer for ^{1}H and 50/100MHz for ^{13}C for 200/400 MHz measurements respectively.

The signals were recorded according to their chemical shifts, which were reported in ppm (s = singlet, d = doublet, t = triplet, q = quartet, qn = quintet, sep = septet, m = multiplet, bs = broad singlet) in comparison to tetramethylsilane (δ = 0 ppm). The spectra were referenced to the used NMR-solvent [^{1}H: CDCl3 (7.26 ppm), ^{13}C: CDCl3 (77.16 ppm)]

^{31}P-NMR-spectroscopy was recorded on a Bruker Advance 600MHz spectrometer.

Analysis of NMR-spectroscopy was performed using MestreNova Version 14.1.0-24037.

Photo-DSC measurements were performed using a Netzsch Photo-DSC 204 F1. The samples were weighed into aluminium DSC crucibles covered with a glass lid. Data analysis was done using the Netzsch Proteus thermal analysis V8.0.1 program. A Lumen Dynamics Omnicure S2000 spot UV curing system was used as a light source. Calibration of the light source was performed using an Omnicure R2000 radiometer.

Viscosity of samples was measured on an Anton Paar MCR 301 rheometer. Evaluation of data was performed using Anton Paar RheoCompass v1.24.

RT-NIR-photorheology was measured on an Anton Paar MCR 302 Rheometer combined with a Bruker Vertex 80 IR spectrometer. Evaluation of rheological data was performed using Anton Paar RheoCompass v1.24. Evaluation of IR-spectoscopy was performed using OPUS 7.0. A Lumen Dynamics Omnicure S2000 spot UV curing system was used as a light source. Calibration of the light source was performed using an OceanOptics USB 2000+ radiometer using the SpectraSuite 1.6.0_11 software.

Tensile tests were performed on a Zwick Z050. Samples were cured in dog bone shape silicone molds in accordance with ISO 527 test specimen 5b. Samples were cured for 300 s on both sides in a Uvitron UV floodlight.

Grinding of AFM samples with sandpaper was performed on a Struers Tegrapol 31, while loose grain **polishing** was done on a Struers Tegramin 30.

AFM measurements were done on a Park Systems XE7 AFM system with an AC160TS cantilever. Data evaluation was performed using Park Systems XEI 5.1.6 software.

Abbreviations

AIBN	Azobisisobutyronitrile
APF	allyl-functionalized pTHF
$CDCl_3$	deuterated chloroform
$CHCl_3$	chloroform
DAA	diallyl adipate
DBC	double bond conversion
DCM	dichloromethane
DSC	differential scanning calorimetry
EE	ethyl acetate
Et_2O	diethyl ether
EtOH	ethanol
HPLC	high performance liquid chromatography
LCEM3,2	liquid crystalline ene-monomer 1,2
MeOH	methanol
MPLC	medium pressure liquid chromatography
NIR-spectroscopy	near infrared spectroscopy
NMR-spectroscopy	nuclear magnetic resonance spectroscopy
PE	petrol ether
Photo-DSC	photo-differential scanning calorimetry
pTHF	poly(tetrahydrofuran)
POM	polarized optical microscopy
THF	tetrahydrofuran
Cr	crystalline
I	isotropic melt
LC	liquid crystalline
N	nematic liquid crystalline phase
Sm	smectic liquid crystalline phase

References

1.   Childress, K. K.; Alim, M. D.; Mavila, S.; Martinez, V.; Ding, Y.; Bowman, C. N.; Stansbury, J. W., Systematic Modulation and Structure–Property Relationships in Photopolymerizable Thermoplastics. *ACS Applied Polymer Materials* **2021**.

2.   Gebhardt, A.; Hötter, J.-S., Additive Manufacturing. In *Additive Manufacturing*, Gebhardt, A.; Hötter, J.-S., Eds. Hanser2016; pp I-XX.

3.   Park, S. H.; Yang, D. Y.; Lee, K. S., Two-photon stereolithography for realizing ultraprecise three-dimensional nano/microdevices. *Laser & Photonics Reviews* **2009,** *3*, 1-11.

4.   Nikitin, A. N.; Cherebylo, S. A.; Ipolitov, E. V.; Kamaev, S. V.; Markov, M. A.; Novikov, M. M.; Vnuk, V. V., Features of crosslinking polymerization in laser stereolithography. *Journal of Physics: Conference Series* **2019,** *1347*, 012097.

5.   Gmeiner, R.; Mitteramskogler, G.; Stampfl, J.; Boccaccini, A. R., Stereolithographic Ceramic Manufacturing of High Strength Bioactive Glass. *International Journal of Applied Ceramic Technology* **2015,** *12*, 38-45.

6.   Steyrer, B.; Busetti, B.; Harakály, G.; Liska, R.; Stampfl, J., Hot Lithography vs. room temperature DLP 3D-printing of a dimethacrylate. *Additive Manufacturing* **2018,** *21*, 209-214.

7.   Yagci, Y.; Jockusch, S.; Turro, N. J., Photoinitiated Polymerization: Advances, Challenges, and Opportunities. *Macromolecules* **2010,** *43*, 6245-6260.

8.   Ahmad, N. M.; Charleux, B.; Farcet, C.; Ferguson, C. J.; Gaynor, S. G.; Hawkett, B. S.; Heatley, F.; Klumperman, B.; Konkolewicz, D.; Lovell, P. A.; Matyjaszewski, K.; Venkatesh, R., Chain Transfer to Polymer and Branching in Controlled Radical Polymerizations of n-Butyl Acrylate. *Macromol Rapid Commun* **2009,** *30*, 2002-21.

9.   Gorsche, C.; Koch, T.; Moszner, N.; Liska, R., Exploring the benefits of β-allyl sulfones for more homogeneous dimethacrylate photopolymer networks. *Polymer Chemistry* **2015,** *6*, 2038-2047.

10.   Bagheri, A.; Jin, J., Photopolymerization in 3D Printing. *ACS Applied Polymer Materials* **2019,** *1*, 593-611.

11.   Pierrel, J.; Ibrahim, A.; Croutxé-Barghorn, C.; Allonas, X., Effect of the oxygen affected layer in multilayered photopolymers. *Polymer Chemistry* **2017,** *8*, 4596-4602.

12.   Chatani, S.; Kloxin, C. J.; Bowman, C. N., The power of light in polymer science: photochemical processes to manipulate polymer formation, structure, and properties. *Polym. Chem.* **2014,** *5*, 2187-2201.

13.   What is a Jablonski Diagram? In *Edinburgh Instruments Blog*2021.

14.   Moszner, N. H., T.; Burtscher, P.; Vogel, K.; Todd, J. C.; Siegward, H.; Peschke,; A., Ivocerin - A milestone in composite

technology. In *Ivoclar Vivadent Report*2013; Vol. 19.

15.   Y. Kadoma, S. F., Kinetic evaluation of reactivity of bisphenol A derivatives as radical scavengers for methacrylate polymerization. *Biomaterials* **2000**, 2125-2130.

16.   Esfandiari, P.; Ligon, S. C.; Lagref, J. J.; Frantz, R.; Cherkaoui, Z.; Liska, R., Efficient stabilization of thiol-ene formulations in radical photopolymerization. *Journal of Polymer Science Part A: Polymer Chemistry* **2013,** *51*, 4261-4266.

17.   Fairbanks, B. D.; Macdougall, L. J.; Mavila, S.; Sinha, J.; Kirkpatrick, B. E.; Anseth, K. S.; Bowman, C. N., Photoclick Chemistry: A Bright Idea. *Chem Rev* **2021,** *121*, 6915-6990.

18.   Hoyle, C. E.; Bowman, C. N., Thiol-ene click chemistry. *Angew Chem Int Ed Engl* **2010,** *49*, 1540-73.

19.   Hoyle, C. E.; Lee, T. Y.; Roper, T., Thiol-enes: Chemistry of the past with promise for the future. *Journal of Polymer Science Part A: Polymer Chemistry* **2004,** *42*, 5301-5338.

20.   Hiorns, R., Polymer Handbook, 4th edn, Edited by J Brandup, EH Immergut and EA Grulke, Associate Editors A Abe and DR Bloch, John Wiley and Sons, New York, 1999, pp 2250, price £210 ISBN 0-471-16628-6. *Polymer International* **2000,** *49*, 807-807.

21.   Cheng, S. Z. D.; Jin, S., Crystallization and melting of metastable crystalline polymers. In *Applications to Polymers and Plastics*,2002; pp 167-195.

22.   Vaughan, A. S.; Bassett, D. C., 12 - Crystallization and Morphology. In *Comprehensive Polymer Science and Supplements*, Allen, G.; Bevington, J. C., Eds. Pergamon: Amsterdam, 1989; pp 415-457.

23.   Hsiao, B. S., Semicrystalline Polymers: Lamellar Morphology by SAXS. In *Encyclopedia of Materials: Science and Technology*, Buschow, K. H. J.; Cahn, R. W.; Flemings, M. C.; Ilschner, B.; Kramer, E. J.; Mahajan, S.; Veyssière, P., Eds. Elsevier: Oxford, 2002; pp 1-6.

24.   Saville, B. P., Polarized Light: Qualitative Microscopy. In: Hemsley D.A. (eds) Applied Polymer Light Microscopy. Springer, Dordrecht. **1989**.

25.   Avrami, M., Kinetics of Phase Change. I General Theory. *The Journal of Chemical Physics* **1939,** *7*, 1103-1112.

26.   Hobson, R., Glass Formation and Sub-Tg Transitions in Polymers: Influence of Carbon Chemistry. In *Encyclopedia of Materials: Science and Technology*, Buschow, K. H. J.; Cahn, R. W.; Flemings, M. C.; Ilschner, B.; Kramer, E. J.; Mahajan, S.; Veyssière, P., Eds. Elsevier: Oxford, 2001; pp 3545-3550.

27.   Bera, M. K.; Bu, W.; Uysal, A., Liquid Surface X-Ray Scattering. In *Physical Chemistry of Gas-Liquid Interfaces*,2018; pp 167-194.

28.   Ciofani, G., Menciassi, Arianna, Piezoelectric Nanomaterials for Biomedical Applications. **2012**.

29. Turcott, E.; Nguyen, K.; Garcia-Rejon, A., Microstrcture development during the injection molding of PET/LCP blends. *Polymer Engineering and Science - POLYM ENG SCI* **2001,** *41*, 603-617.

30. Yang, Q.; Hirata, M.; Hsu, Y.-I.; Lu, D.; Kimura, Y., Improved thermal and mechanical properties of poly(butylene succinate) by polymer blending with a thermotropic liquid crystalline polyester. *Journal of Applied Polymer Science* **2014,** *131*.

31. Mingos, D. M., Structure and Bonding. 2014; Vol. 162, pp 1-65.

32. Percec, V.; Tomazos, D., 14 - Molecular Engineering of Liquid Crystalline Polymers. In *Comprehensive Polymer Science and Supplements*, Allen, G.; Bevington, J. C., Eds. Pergamon: Amsterdam, 1989; pp 299-383.

33. Ujiie, S.; Miyazaki, W.; Iimura, K., Influence of spacer length on liquid crystal microstructures of branched polyethyleneimines with mesogenic pendent groups. *Polymer Journal* **2012,** *44*, 561-566.

34. Aouada, F. A.; de Moura, M. R.; Fernandes, P. R. G.; Rubira, A. F.; Muniz, E. C., Optical and morphological characterization of polyacrylamide hydrogel and liquid crystal systems. *European Polymer Journal* **2005,** *41*, 2134-2141.

35. Pichler H., S.-R. C., The polarizing microscope. In: Rock-forming Minerals in Thin Section. Springer, Dordrecht. **1997**.

36. Lowe, A. B., Thiol–ene "click" reactions and recent applications in polymer and materials synthesis: a first update. *Polym. Chem.* **2014,** *5*, 4820-4870.

37. Alim, M. D.; Childress, K. K.; Baugh, N. J.; Martinez, A. M.; Davenport, A.; Fairbanks, B. D.; McBride, M. K.; Worrell, B. T.; Stansbury, J. W.; McLeod, R. R.; Bowman, C. N., A photopolymerizable thermoplastic with tunable mechanical performance. *Materials Horizons* **2020**.

38. Sycks, D. G.; Safranski, D. L.; Reddy, N. B.; Sun, E.; Gall, K., Tough Semicrystalline Thiol–Ene Photopolymers Incorporating Spiroacetal Alkenes. *Macromolecules* **2017,** *50*, 4281-4291.

39. Sycks, D. G.; Wu, T.; Park, H. S.; Gall, K., Tough, stable spiroacetal thiol-ene resin for 3D printing. *Journal of Applied Polymer Science* **2018,** *135*.

40. Rangreez, T. A.; Mobin, R., Polymer composites for dental fillings. In *Applications of Nanocomposite Materials in Dentistry*,2019; pp 205-224.

41. Satsangi, N.; Rawls, H. R.; Norling, B. K., Synthesis of low-shrinkage polymerizable methacrylate liquid-crystal monomers. *J Biomed Mater Res B Appl Biomater* **2005,** *74*, 706-11.

42. REACTIVE MESOGENS FOR IMAGE QUALITY. https://www.merckgroup.com/en/expertise/displays/solutions/reactive-mesogens.html (September 7),

43.   LUB, R. A. M. H. a. J., ANISOTROPIC NETWORKS AND GELS OBTAINED BY PHOTOPOLYMERISATION IN THE LIQUID CRYSTALLINE STATE: SYNTHESIS AND APPLICATIONS. **1996**.

44.   Strohriegl, P.; Hanft, D.; Jandke, M.; Pfeuffer, T., Reactive Mesogenes: Synthesis and Application in Optoelectronic Devices. *MRS Online Proceedings Library* **2011,** *709*, 321.

45.   Liu, D.; Broer, D. J., Liquid crystal polymer networks: preparation, properties, and applications of films with patterned molecular alignment. *Langmuir* **2014,** *30*, 13499-509.

46.   Wilderbeek, H. T. A.; van der Meer, M. G. M.; Jansen, M. A. G.; Nelissen, L.; Fischer, H. R.; van Es, J. J. G. S.; Bastiaansen, C. W. M.; Lub, J.; Broer, D. J., Synthesis and properties of phenyl benzoate-based and biphenyl-based liquid crystalline thiol-ene monomers. *Liquid Crystals* **2003,** *30*, 93-108.

47.   Lub, J.; Broer, D. J.; Allan, J. F., The Synthesis and Polymerisation of a Liquid Crystalline Crosslinkable Thiol-Ene Molecule. *Molecular Crystals and Liquid Crystals Science and Technology. Section A. Molecular Crystals and Liquid Crystals* **2006,** *332*, 259-266.

48.   Lalgudi V. Natarajan, C. K. S., Donna M. Brandelik, Richard L. Sutherland, Suresh Chandra, Vincent P. Tondiglia, David Tomlin, and Timothy J. Bunning, Switchable Holographic Polymer-Dispersed Liquid Crystal Reflection Gratings Based on Thiol-Ene Photopolymerization. *Chem. Mater.* **2003,** *15*, 2477-2484.

49.   Yakacki, C. M.; Saed, M.; Nair, D. P.; Gong, T.; Reed, S. M.; Bowman, C. N., Tailorable and programmable liquid-crystalline elastomers using a two-stage thiol–acrylate reaction. *RSC Advances* **2015,** *5*, 18997-19001.

50.   Lu, H. F.; Wang, M.; Chen, X. M.; Lin, B. P.; Yang, H., Interpenetrating Liquid-Crystal Polyurethane/Polyacrylate Elastomer with Ultrastrong Mechanical Property. *J Am Chem Soc* **2019,** *141*, 14364-14369.

51.   Ube, T., Development of novel network structures in crosslinked liquid-crystalline polymers. *Polymer Journal* **2019,** *51*, 983-988.

52.   Yang, H.; Wang, L.; Shao, R.; Clark, N. A.; Ortega, J.; Etxebarria, J.; Albouy, P.-A.; Walba, D. M.; Keller, P., Novel liquid-crystalline mesogens and main-chain chiral smectic thiol-ene polymers based on trifluoromethylphenyl moieties. *Journal of Materials Chemistry* **2009,** *19*.

53.   Yang, H.; Buguin, A.; Taulemesse, J.-M.; Kaneko, K.; Méry, S.; Bergeret, A.; Keller, P., Micron-Sized Main-Chain Liquid Crystalline Elastomer Actuators with Ultralarge Amplitude Contractions. *Journal of the American Chemical Society* **2009,** *131*, 15000-15004.

54.   Koßmehl, G.; Gerecke, B.; Harmsen, N.; Schröder, F.; Vieth, H. M., Liquid Crystalline Main Chain Polysiloxane Esters and their Monomers Part I: Synthesis of some di(ω-unsaturated esters) and their thermal behaviour. *Molecular Crystals and Liquid Crystals*

Science and Technology. Section A. Molecular Crystals and Liquid Crystals **1995,** *269*, 39-53.

55.   Martinez, A. M.; Cox, L. M.; Killgore, J. P.; Bongiardina, N. J.; Riley, R. D.; Bowman, C. N., Permanent and reversibly programmable shapes in liquid crystal elastomer microparticles capable of shape switching. *Soft Matter* **2021,** *17*, 467-474.

56.   Martinez, A. M.; McBride, M. K.; White, T. J.; Bowman, C. N., Reconfigurable and Spatially Programmable Chameleon Skin-Like Material Utilizing Light Responsive Covalent Adaptable Cholesteric Liquid Crystal Elastomers. *Advanced Functional Materials* **2020**.

57.   Hoekstra, D. C.; van der Lubbe, B.; Bus, T.; Yang, L.; Grossiord, N.; Debije, M. G.; Schenning, A., Wavelength-Selective Photopolymerization of Hybrid Acrylate-Oxetane Liquid Crystals. *Angew Chem Int Ed Engl* **2021**.

58.   Ambulo, C. P.; Burroughs, J. J.; Boothby, J. M.; Kim, H.; Shankar, M. R.; Ware, T. H., Four-dimensional Printing of Liquid Crystal Elastomers. *ACS Appl Mater Interfaces* **2017,** *9*, 37332-37339.

59.   Saed, M. O.; Ambulo, C. P.; Kim, H.; De, R.; Raval, V.; Searles, K.; Siddiqui, D. A.; Cue, J. M. O.; Stefan, M. C.; Shankar, M. R.; Ware, T. H., Molecularly-Engineered, 4D-Printed Liquid Crystal Elastomer Actuators. *Advanced Functional Materials* **2019,** *29*.

60.   Barnes, M.; Sajadi, S. M.; Parekh, S.; Rahman, M. M.; Ajayan, P. M.; Verduzco, R., Reactive 3D Printing of Shape-Programmable Liquid Crystal Elastomer Actuators. *ACS Appl Mater Interfaces* **2020,** *12*, 28692-28699.

61.   Shen, Y.; Cong, Y.-H.; Zhang, B.-Y.; Lang, Q.-Y., Influence on properties of epoxy nanocomposites with nanoparticles modified by surfactants with different molecular structures: liquid crystal, rigid and flexible segment structures. *Materials Research Express* **2019,** *6*.

62.   Zhang, G. Y.; Lu, H. B.; Xu, W. B., Synthesis and Application of a Novel Liquid Crystal Monomer 1,4-di-[4-(3-acryloyloxyhexyloxy)benzoyloxy]-2-methyl Benzene. *Advanced Materials Research* **2014,** *875-877*, 3-8.

63.   n-DODECYL (LAURYL) MERCAPTAN. *Organic Syntheses* **1941,** *21*.

64.   Jang, K.; Miura, K.; Koyama, Y.; Takata, T., Catalyst- and Solvent-Free Click Synthesis of Cyclodextrin-Based Polyrotaxanes Exploiting a Nitrile N-Oxide. *Organic Letters* **2012,** *14*, 3088-3091.

65.   Meng, X.; Crestini, C.; Ben, H.; Hao, N.; Pu, Y.; Ragauskas, A. J.; Argyropoulos, D. S., Determination of hydroxyl groups in biorefinery resources via quantitative (31)P NMR spectroscopy. *Nat Protoc* **2019,** *14*, 2627-2647.

66.   Striegel, A., *Modern Size-Exclusion Liquid Chromatography: Practice of Gel Permeation and Gel Filtration Chromatography*. 2009.

67.   Sutton, J. T.; Rajan, K.; Harper, D. P.; Chmely, S. C., Lignin-Containing Photoactive Resins for 3D Printing by Stereolithography. *ACS Appl Mater Interfaces* **2018,** *10*, 36456-36463.

68.   Gorsche, C.; Harikrishna, R.; Baudis, S.; Knaack, P.; Husar, B.; Laeuger, J.; Hoffmann, H.; Liska, R., Real Time-NIR/MIR-Photorheology: A Versatile Tool for thein SituCharacterization of Photopolymerization Reactions. *Analytical Chemistry* **2017,** *89*, 4958-4968.

69.   Aly, A. A.; Arabia, S. In *Heat Treatment of Polymers: A Review*2015.

70.   Phase Imaging / Phase Detection Microscopy. https://www.parksystems.com/park-spm-modes/91-standard-imaging-mode/221-phase-imaging-phase-detection-microscopy-pdm (Nov 17),

71.   Sarie, J. C.; Thiehoff, C.; Neufeld, J.; Daniliuc, C. G.; Gilmour, R., Enantioselective Synthesis of 3-Fluorochromanes via Iodine(I)/Iodine(III) Catalysis. *Angew Chem Int Ed Engl* **2020,** *59*, 15069-15075.

72.   Alvarez, R.; Mehl, G. H., Cholesteric Silatranes. *Molecular Crystals and Liquid Crystals* **2005,** *439*, 259/[2125]-267/[2133].

73.   Goo Soo Lee, Y.-J. L., So Yeun Choi, Yong Soo Park, and Kyung Byung Yoon, Self-Assembly of a-Glucosidase and D-Glucose-Tethering ZeoliteCrystals into Fibrous Aggregates. *J. Am. Chem. Soc* **2000,** *122*, 12151-12157.

Appendix

## Photorheology measurement graphs
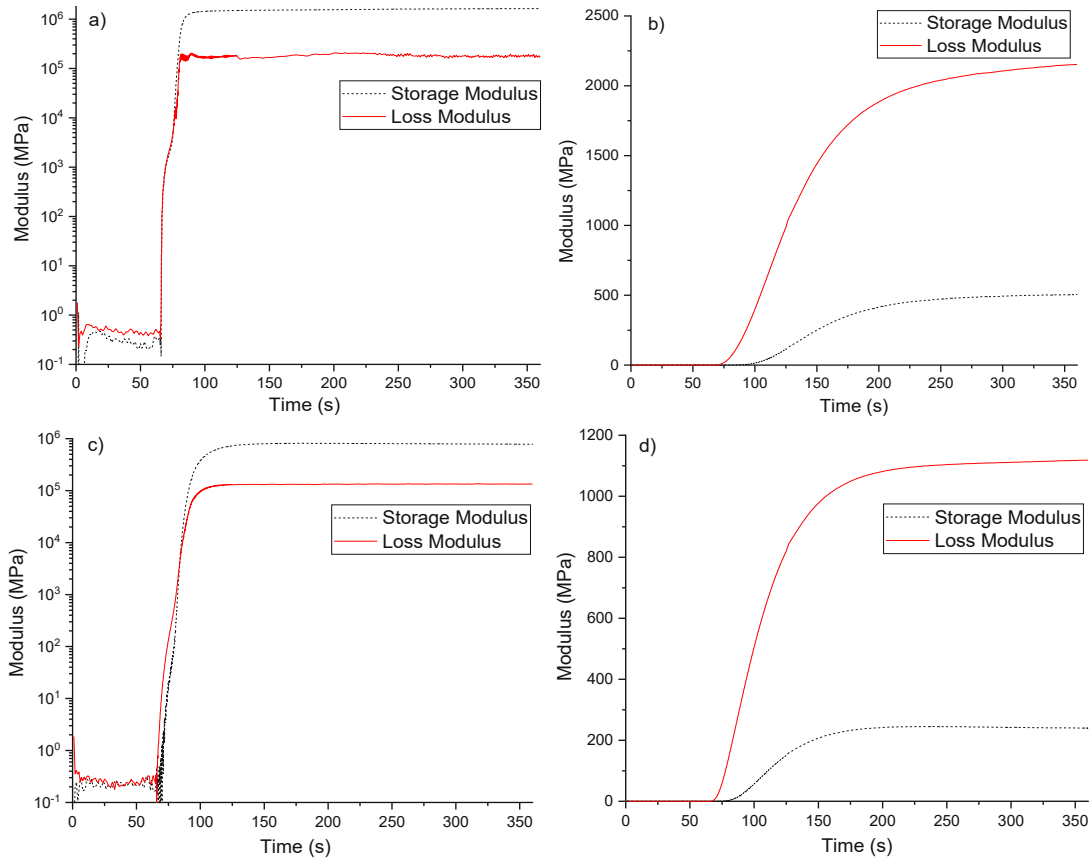
A 1: Photorheology measurement graphs of a) LCEM3-HDT, b) the HDT-DAT reference formulation, c) 50DAA, d) 75DAA. A logarithmic scale was used for the storage and loss modulus for samples LCEM3-HDT and 50APF due to the high moduli observed in the measurements. For all other samples, a linear scale was used.
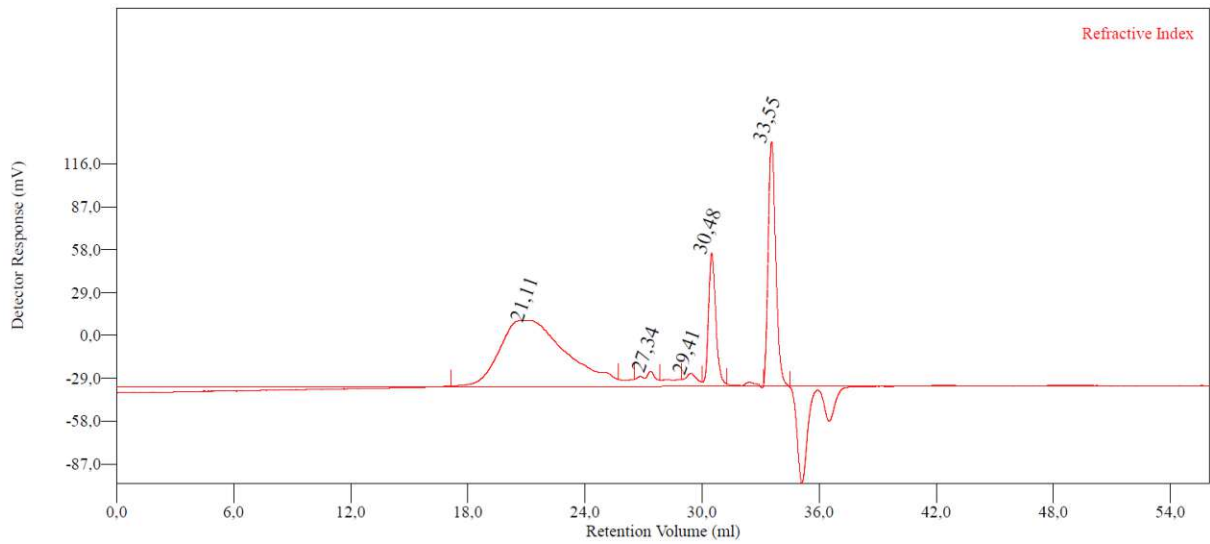
A1
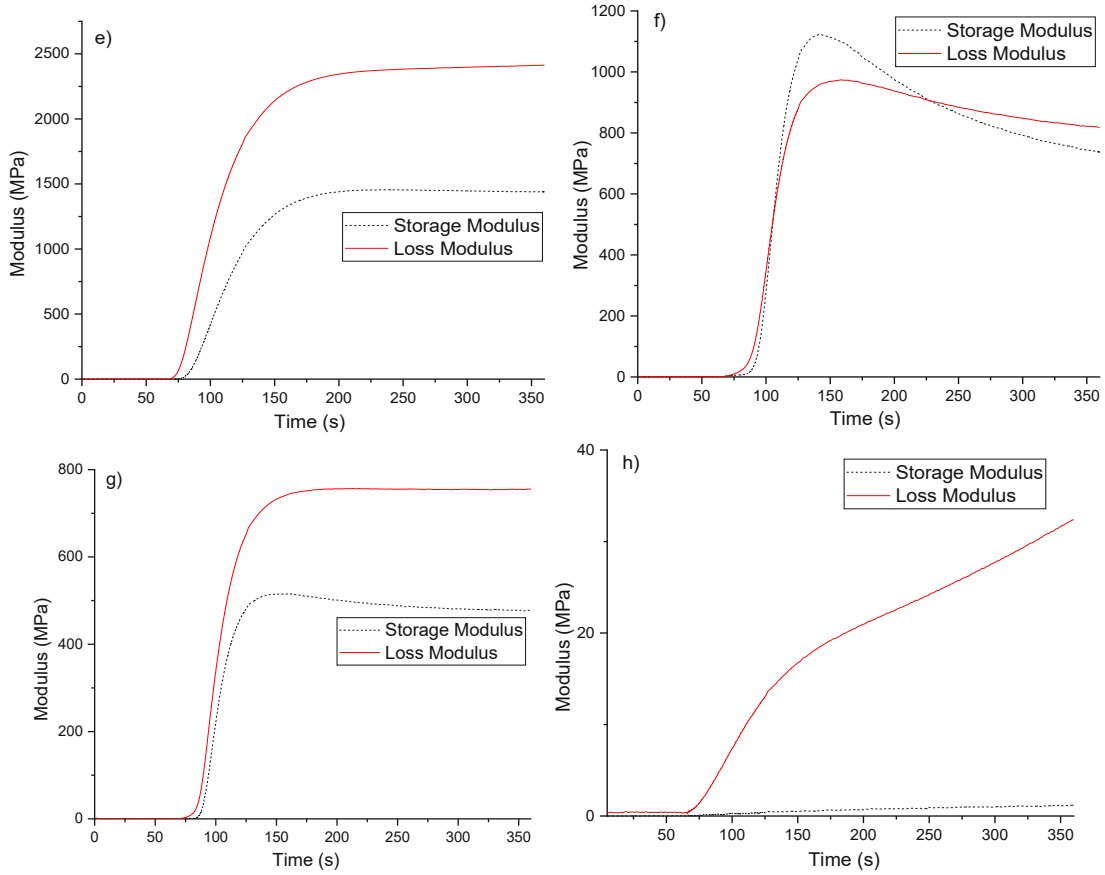
A 2: Photorheology measurement graphs of e) 90DAA, f) 25APF, g) 50APF, h) 75APF. Irradiation starts at 60
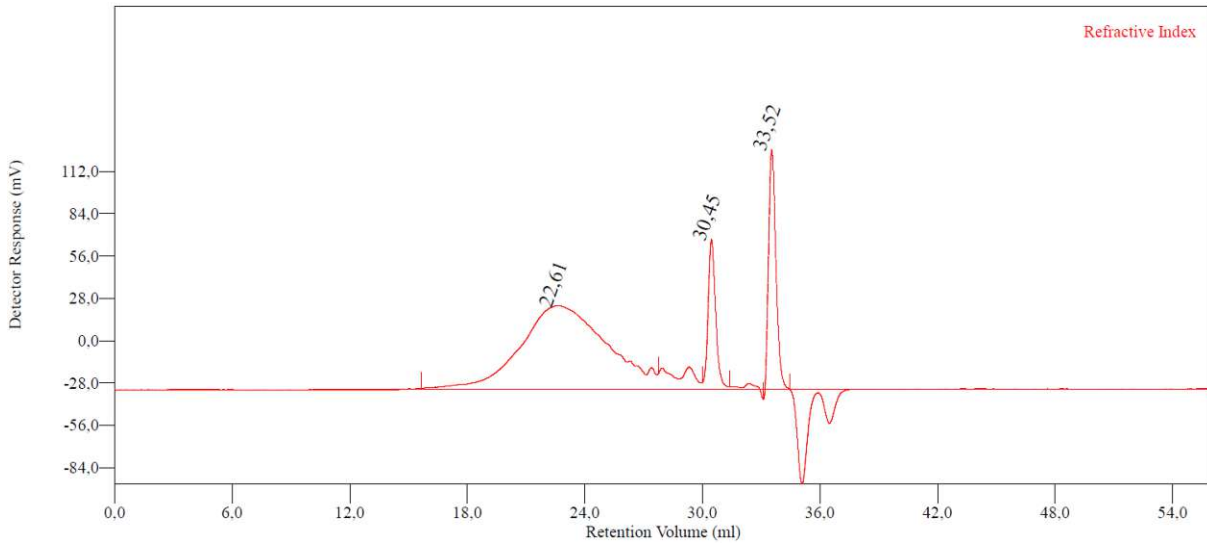
seconds into the measurement.

THF-GPC elugrams
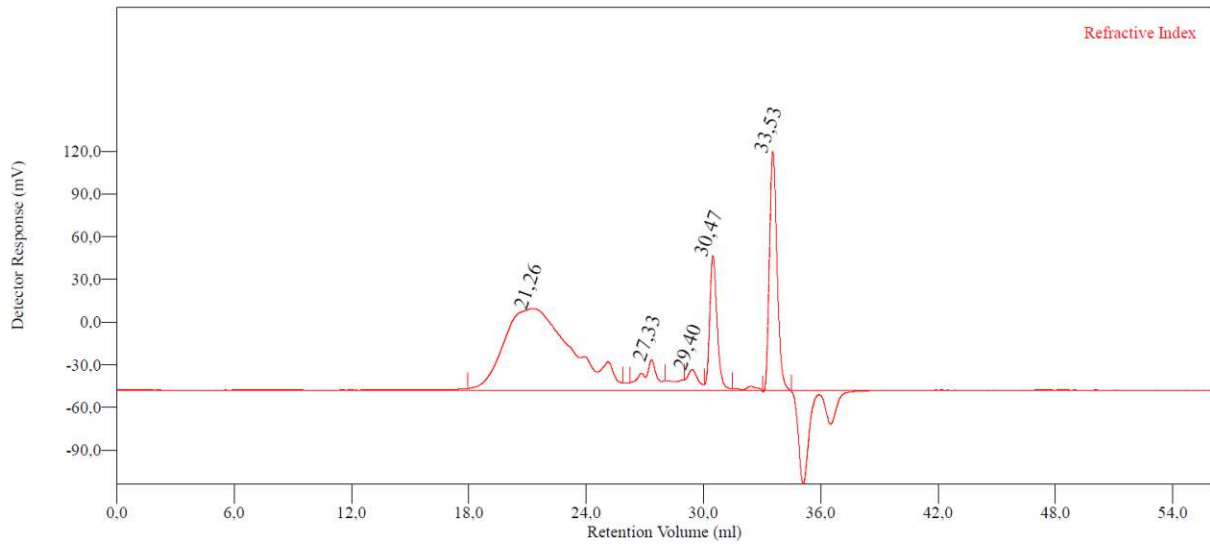
A 3: GPC elugram of 50APF polymer sample.

A 4: GPC elugram of 75APF polymer sample.

A 5: GPC elugram of 90DAA polymer sample.